

FL-TR-91-2192

AD-A246 894



MODELING REGIONAL SEISMIC WAVES

Donald V. Helmberger  
David G. Harkrider

California Institute of Technology  
Seismological Laboratory  
Pasadena, CA 91125

DTIC  
ELECTE  
JAN 15 1992  
S B D

31 July 1991

Final Report  
24 March 1989-31 July 1991

APPROVED FOR PUBLIC RELEASE; DISTRIBUTION UNLIMITED

92-01224



PHILLIPS LABORATORY  
AIR FORCE SYSTEMS COMMAND  
HANSCOM AIR FORCE BASE, MASSACHUSETTS 01731-5000

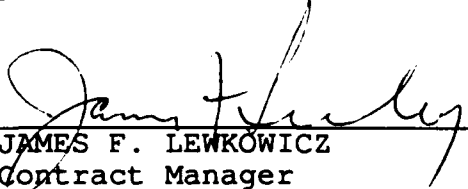
92 1 14 010

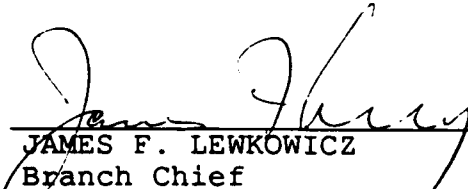
SPONSORED BY  
Defense Advanced Research Projects Agency  
Nuclear Monitoring Research Office  
ARPA ORDER NO. 5307

MONITORED BY  
Phillips Laboratory  
Contract FY19628-89-K-0028

The views and conclusions contained in this document are those of the authors and should not be interpreted as representing the official policies, either expressed or implied, of the Defense Advanced Research Projects Agency or the U.S. Government.

This technical report has been reviewed and is approved for publication.

  
JAMES F. LEWKOWICZ  
Contract Manager  
Solid Earth Geophysics Branch  
Earth Sciences Division

  
JAMES F. LEWKOWICZ  
Branch Chief  
Solid Earth Geophysics Branch  
Earth Sciences Division

  
DONALD H. ECKHARDT, Director  
Earth Sciences Division

This report has been reviewed by the ESD Public Affairs Office (PA) and is releasable to the National Technical Information Service (NTIS).

Qualified requestors may obtain additional copies from the Defense Technical Information Center. All others should apply to the National Technical Information Service.

If your address has changed, or if you wish to be removed from the mailing list, or if the addressee is no longer employed by your organization, please notify PL/IMA, Hanscom AFB, MA 01731-5000. This will assist us in maintaining a current mailing list.

Do not return copies of this report unless contractual obligations or notices on a specific document requires that it be returned.

UNCLASSIFIED

SECURITY CLASSIFICATION OF THIS PAGE

## REPORT DOCUMENTATION PAGE

1a. REPORT SECURITY CLASSIFICATION UNCLASSIFIED			1b. RESTRICTIVE MARKINGS	
2a. SECURITY CLASSIFICATION AUTHORITY			3. DISTRIBUTION/AVAILABILITY OF REPORT Approved for public release: distribution unlimited	
2b. DECLASSIFICATION/DOWNGRADING SCHEDULE				
4. PERFORMING ORGANIZATION REPORT NUMBER(S)			5. MONITORING ORGANIZATION REPORT NUMBER(S) PL-TR-91-2192	
6a. NAME OF PERFORMING ORGANIZATION California Institute of Tech. Seismological Laboratory		6b. OFFICE SYMBOL (If applicable)	7a. NAME OF MONITORING ORGANIZATION Phillips Laboratory	
6c. ADDRESS (City, State and ZIP Code) Pasadena, California 91125			7b. ADDRESS (City, State and ZIP Code) Hanscom Air Force Base, Massachusetts 01731-5000	
8a. NAME OF FUNDING/SPONSORING ORGANIZATION Defense Advanced Research Projects Agency		8b. OFFICE SYMBOL (If applicable) NMRO	9. PROCUREMENT INSTRUMENT IDENTIFICATION NUMBER F19628-89-K-0028	
8c. ADDRESS (City, State and ZIP Code) 1400 Wilson Boulevard Arlington, Virginia 22209-2308			10. SOURCE OF FUNDING NOS.	
11. TITLE (Include Security Classification) Modeling Regional Seismic Waves			PROGRAM ELEMENT NO. 61101E	PROJECT NO. 9A10
			TASK NO. DA	WORK UNIT NO. AD
12. PERSONAL AUTHOR(S) Donald V. Helmlberger and David G. Harkrider				
13a. TYPE OF REPORT Final	13b. TIME COVERED FROM 3/24/89 TO 7/31/91	14. DATE OF REPORT (Yr., Mo., Day) 31 July 1991	15. PAGE COUNT '08	
16. SUPPLEMENTARY NOTATION				
17. COSATI CODES			18. SUBJECT TERMS (Continue on reverse if necessary and identify by block number)	
FIELD	GROUP	SUB GR.		
			M <sub>s</sub> ; regional surface wave magnitudes; broad-band modeling regional seismograms; earthquake relocation Tibet.	
19. ABSTRACT				
<p>The research performed under the contract, during the period 1 August 1989 through 31 July 1991, can be divided into three main topics; modeling regional broad-band seismograms from the Imperial Valley to Pasadena, determining surface wave magnitudes for NTS events using regional data, and waveform modeling to determine the depth of earthquakes in Tibet leading to new origin times and a better estimation of <math>P_n</math> and <math>S_n</math> velocities.</p> <p>In section 1, we address broad-band wave propagation along a corridor from Imperial Valley to Pasadena, California. The path consists of 50 km of slow basin structure with a shallow moho followed by 250 km of relatively normal Southern California structure approaching Pasadena. Events occurring in the valley produce extended body wave codas which carry a dispersive waveform imprint along with longer period Rayleigh waves. Many features of these seismograms at period greater than a few seconds can be modeled by applying a finite-difference technique to a 2D structure. Shorter periods display complex behaviors not easily modeled by present techniques, especially for shallow events. Events occurring in the normal structure produce broad-band SH waveforms that can be modeled, analytically, if we include some extra empirically derived parameters determined by calibration events. These parameters are determined by adjusting travel time differentials between the decomposed wavefield S, sS, etc. For example, delays in sS relative to S correspond to local corrections for sediment cover for a particular source region. Asperities and directivity become increasingly important at shorter periods, as demonstrated by numerical experiments and observation. Numerical experiments conducted on 2D models with embedded scatterers appear to explain coda development and some of the properties of the Lg phase.</p>				
20. DISTRIBUTION/AVAILABILITY OF ABSTRACT UNCLASSIFIED/UNLIMITED <input checked="" type="checkbox"/> SAME AS RPT. <input type="checkbox"/> DTIC USERS <input type="checkbox"/>			21. ABSTRACT SECURITY CLASSIFICATION UNCLASSIFIED	
22a. NAME OF RESPONSIBLE INDIVIDUAL James E. Harkrider			22b. TELEPHONE NUMBER (Include Area Code) (617) 377-3028	22c. OFFICE SYMBOL PL/IMB

In section 2, we calculate surface wave magnitudes for 112 Nevada Test Site (NTS) explosions from a data set of regional long-period seismograms from North American stations. In order to utilize the nearer regional stations ( $\Delta < 25^\circ$ ), a new method for determining  $M_S$  and been developed which employs synthetic seismograms to establish a relationship between the amplitude of the regional Airy phase, or Rayleigh pulse, of the data and an associated surface wave magnitude, based on conventional  $M_S$  determinations, calculated from a synthetic seismogram propagated to  $40^\circ$ . This method easily lends itself to implementing path corrections. The inclusion of path corrections decreases the  $M_S$  variance by a factor of two and also decreases the average value by 0.08 magnitude units. This latter effect is attributed to the particular station network used. The method gives stable  $M_S$  values that correlate well with other magnitude scale values over a range of three orders of magnitude in source yield. Our most refined  $M_S$  values yield the relationship  $m_b = 0.9 \times M_S + 1.82$ . When events are grouped with respect to source region, significantly better fits to these individual site linear regression curves are obtained compared to the fits obtained using a single, all inclusive model. This observation implies that shot site parameters and source structure effect surface wave magnitude measurements, although event yield site distribution also may be in part responsible.

Since our magnitude values are based on a theoretical continental structure, we regressed our values with the more standard values of Marshall et al. (1979). Using 14 common NTS events we found that our values were greater by  $0.53 \pm 0.03$  magnitude units.

In section 3, we present a note on the relocation of Tibetan earthquakes. Present ISC locations for earthquakes beneath Tibet indicate a random distribution of events down to a depth of about 50 km. This distribution might be expected from a relatively cool crust which would allow the seismo-genic zone to extend to such depths. A detailed investigation of the Tibetan earthquakes, with magnitude greater than 5.5 from 1964 to 1986, yields a distinctly different picture. Waveform modeling of depth phases such as  $pP$  indicates that only three or four events from this population is actually deeper than 25 km. These few events occur near the edges of the Plateau where active subduction is occurring as suggested by the thrust-like nature of their mechanisms. The events, averaging the entire population, occurred earlier than indicated by the ISC by about 3 seconds which leads to about a 1.5% and 0.5% over estimation of  $P_n$  and  $S_n$  velocities respectively applying ISC tables and standard flat-layered models. A more serious error occurs if the  $P_n$  and  $S_n$  velocities are determined by correcting for source depth but assuming the ISC origin times.

FINAL TECHNICAL REPORT  
24 may 1989 - 31 July 1991

ARPA Order No.:

Name of Contractor: California Institute of Technology

Effective Date of Contract: 24 March 1989

Contract Expiration Date: 31 July 1991

Contract Number: F19628-89-K-0028

Principal Investigators: Donald V. Helmberger  
(818)356-6998

David G. Harkrider  
(818)356-6910

Program Manager: James F. Lewkowicz  
(617)861-3028

Short Title of Work: Modeling Regional Seismic Waves

The views and conclusions contained in this document are those of the authors and should not be interpreted as necessarily representing the official policies, either expressed or implied, of the Defense Advanced Research Projects Agency or the U.S. Government

Sponsored by  
Defense Advanced Research Projects Agency (DoD)  
Nuclear Monitoring Research Office  
ARPA Order No.  
Issued by the Air Force Geophysics Laboratory under  
Contract#F19628-89-K-0028

Seismological Laboratory  
Division of Geological and Planetary Sciences  
California Institute of Technology  
Pasadena, California 91125

Accession For	
NTIS GRA&I	<input checked="" type="checkbox"/>
DTIC TAB	<input type="checkbox"/>
Unannounced	<input type="checkbox"/>
Justification	
By _____	
Distribution/	
Availability Codes	
Dist	Avail and/or Special
A-1	

## TABLE OF CONTENTS

	Page Numbers
Summary.....	V
1. Broad-band modeling of regional seismograms Imperial Valley to Pasadena.....	1
2. Determining $M_S$ Magnitudes from Regional NTS Data.....	49
3. A Note on the Relocation of Tibetan earthquakes.....	81

## Summary

The research performed under the contract, during the period 1 August 1989 through 31 July 1991, can be divided into three main topics; modeling regional broad-band seismograms from the Imperial Valley to Pasadena, determining surface wave magnitudes for NTS events using regional data, and waveform modeling to determine the depth of earthquakes in Tibet leading to new origin times and a better estimation of  $P_n$  and  $S_n$  velocities.

In section 1, we address broad-band wave propagation along a corridor from Imperial Valley to Pasadena, California. The path consists of 50 km of slow basin structure with a shallow moho followed by 250 km of relatively normal Southern California structure approaching Pasadena. Events occurring in the valley produce extended body wave codas which carry a dispersive waveform imprint along with longer period Rayleigh waves. Many features of these seismograms at period greater than a few seconds can be modeled by applying a finite-difference technique to a 2D structure. Shorter periods display complex behaviors not easily modeled by present techniques, especially for shallow events. Events occurring in the normal structure produce broad-band SH waveforms that can be modeled, analytically, if we include some extra empirically derived parameters determined by calibration events. These parameters are determined by adjusting travel time differentials between the decomposed wavefield S, sS, etc. For example, delays in sS relative to S correspond to local corrections for sediment cover for a particular source region. Asperities and directivity become increasingly important at shorter periods, as demonstrated by numerical experiments and observation. Numerical experiments conducted on 2D models with embedded scatterers appear to explain coda development and some of the properties of the Lg phase.

In section 2, we calculate surface wave magnitudes for 112 Nevada Test Site (NTS) explosions from a data set of regional long-period seismograms from North American stations. In order to utilize the nearer regional stations ( $\Delta < 25^\circ$ ), a new method for determining  $M_s$  has been developed which employs synthetic seismograms to establish a relationship between the amplitude of the regional Airy phase, or Rayleigh pulse, of the data and an associated surface wave magnitude, based on conventional  $M_s$  determinations, calculated from a synthetic seismogram propagated to  $40^\circ$ . This method easily lends itself to implementing path corrections. The inclusion of path corrections decreases the  $M_s$  variance by a factor of two and also decreases the average value by 0.08 magnitude units. This latter effect is attributed to the particular station network used. The method gives stable  $M_s$  values that correlate well with other magnitude scale values over a range of three orders of magnitude in source yield. Our most refined  $M_s$  values yield the relationship  $m_b = 0.9 \times M_s + 1.82$ . When events are grouped with respect to source region, significantly better fits to these individual site linear regression curves are obtained compared to the fits obtained using a single, all inclusive model. This observation implies that shot site parameters and source structure effect surface wave magnitude measurements, although event yield site distribution also may be in part responsible.

Since our magnitude values are based on a theoretical continental structure, we regressed our values with the more standard values of Marshall et al. (1979). Using 14 common NTS events we found that our values were greater by  $0.53 \pm 0.03$  magnitude units.

In section 3, we present a note on the relocation of Tibetan earthquakes. Present ISC locations for earthquakes beneath Tibet indicate a random distribution of events down to a depth of about 50 km. This distribution might be expected

from a relatively cool crust which would allow the seismo-genic zone to extend to such depths. A detailed investigation of the Tibetan earthquakes, with magnitude greater than 5.5 from 1964 to 1986, yields a distinctly different picture. Waveform modeling of depth phases such as  $pP$  indicates that only three or four events from this population is actually deeper than 25 km. These few events occur near the edges of the Plateau where active subduction is occurring as suggested by the thrust-like nature of their mechanisms. The events, averaging the entire population, occurred earlier than indicated by the ISC by about 3 seconds which leads to about a 1.5% and 0.5% over estimation of  $P_n$  and  $S_n$  velocities respectively applying ISC tables and standard flat-layered models. A more serious error occurs if the  $P_n$  and  $S_n$  velocities are determined by correcting for source depth but assuming the ISC origin times.



## **SECTION 1**

Broad-band modeling of regional seismograms;  
Imperial Valley to Pasadena

## **Broad-band modeling of regional seismograms; Imperial Valley to Pasadena**

**D. Helmberger, R. Stead, Phyllis Ho-Liu and D. Dreger**

### **Abstract**

This paper addresses broad-band wave propagation along a corridor from Imperial Valley to Pasadena, California. The path consists of 50 km of slow basin structure with a shallow moho followed by 250 km of relatively normal Southern California structure approaching Pasadena. Events occurring in the valley produce extended body wave codas which carry a dispersive waveform imprint along with longer period Rayleigh waves. Many features of these seismograms at periods greater than a few seconds can be modeled by applying a finite-difference technique to a 2D structure. Shorter periods display complex behaviors not easily modeled by present techniques, especially for shallow events. Events occurring in the normal structure produce broad-band SH waveforms that can be modeled, analytically, if we include some extra empirically derived parameters determined by calibration events. These parameters are determined by adjusting travel time differentials between the decomposed wavefield  $S$ ,  $sS$ , etc. For example, delays in  $sS$  relative to  $S$  correspond to local corrections for sediment cover for a particular source region. Asperities and directivity become increasingly important at shorter periods, as demonstrated by numerical experiments and observation. Numerical experiments conducted on 2D models with embedded scatterers

appear to explain coda development and some of the properties of the Lg phase.

### Introduction

One of the fundamental reasons why quantitative seismology and waveform modeling is contributing to source retrieval and to the monitoring of nuclear weapons is its prediction capability. That is, given a set of seismograms we can correct for propagational effects and predict the nature of the source. This is relatively easy when dealing with teleseismic body waves and well dispersed long period surface waves. But since small events cannot be seen teleseismically, we must address the more difficult problem of source retrieval from regional phases.

An intermediate stage in this development is to examine broad band records, BB, at regional distances for events large enough to be well-recorded teleseismically. This feature allows the source parameters to be determined by modeling teleseismic bodywave phases, direct P and reflected phases (e.g. pP, etc.). Starting with a known source allows detailed studies of regional seismograms in terms of path effects and the development of BB Green's functions. Hopefully, these Green's functions can be used to estimate smaller events in the general vicinity of the larger event or master event. Such a procedure has been used earlier to calibrate surface wave paths, Romanowicz (1982). Unfortunately, there are not many BB recordings of significant events presently available. Some results from detailed studies of these existing records are encouraging while others are not.

An example of the former is given in a paper by Zhao and Helmberger (1991), see figure 1, for a path from Quebec to Harvard. Their strategy for modeling these records was to break the seismograms into segments  $P_{n1}$ , containing  $P_n$ ,  $pP_n$ ,  $sP_n$ ,  $P_mP$ ,  $P$ , coupled PL waves;  $S_{n1}$ , containing  $S_n$ ,  $sS_n$ ,  $S_mS$ , (etc.); and the fundamental Rayleigh waves. Synthetics are generated for the various segments with generalized rays, normal modes and reflectivity methods where the advantages of each technique are exploited. Information about the upper crust is obtained from the fundamental modes and crustal thickness and velocity gradients in the mantle from  $P_{n1}$  and  $S_{n1}$  waves.

It is rather remarkable that a flat layered model (see Table 1) can explain so many features. In fact, a simple layer over a half space does a good job for the first 100 seconds of long period motions.

These results suggest that in stable regions where  $S_n$  propagates to large distances, the possibility of using  $sS_n$  to help fix source depths could prove useful. Note that  $S_{n1}$  and  $sS_n$  are considerably larger than  $P_n$  and  $pP_n$  and can probably be seen for smaller events. The usefulness of the interference produce by  $P_n$  and  $pP_n$  has already been demonstrated by Burdick, Saikia and Smith (1991) for explosions.

Explaining the jitter in the BB observations displayed in figure 1, (assuming a flat-layered model), has proven difficult. Thus, it appears appropriate at this stage to introduce scattering into the synthetics as proposed by Flatte and Wu (1988), Kennett (1989) and others. Note that this method supposes that a first-order model

already exists. We will show that establishing these models is no easy task, especially in tectonic regions, as discussed for a BB dataset for a corridor from Imperial Valley to Pasadena. Complexity abounds along this profile and the short period modeling results are not so encouraging.

### Observations

The observations addressed in this study consist of a collection of low-gain short period records from moderate sized events along the San Jacinto fault system which have known source mechanisms, and BB observations of recent smaller events. Figure 2 gives the locations of these events which range (roughly) from 170 to 270 km. The more distance events are beneath the Imperial Valley. Table 2 list some of the event information, source depth, etc. These events are all strike-slip in nature and have been studied in detail by several authors: for example see Bent and Helmberger (1991).

One of the reasons for working with the Pasadena data is the presence of a recently installed Streckeisen instrument. Example seismograms from this system are displayed in figures 3, 4, and 5. The bottom three rows of simulations correspond to three older types of instruments operated at Pasadena and bracket the range of frequencies of interest. These three events are located along the extended San Jacinto fault system and can be used to compare with the older well-studied large events such as the events located in figure 2.

Since the azimuth towards Pasadena is near the (P-SV) node assuming a strike-slip orientation, we would expect considerable

variation on the vertical component which is apparently observed, (see figures 4 and 5), where the P-waves appear to be of opposite polarity. The tangential motions are similar as expected along this azimuth. Recordings from the aftershock of the Superstition Hills event, see (c) in figure 2, display distinctly different properties from the first two sets. Note that the BB tangential motions are longer period and the ratio of wa.lp-to-wa.sp period torsion responses increase from (3) to (5). Stead (1989) compares these ratios for 20 events in the region and finds this same change on average. Another difference is the enhanced strengths of surface waves for basin events and their relatively slow velocity relative to the bodywaves.

Note that as the Rayleigh waves become stronger, the SV waves become weaker. These same general features can be seen in the older records as displayed in figure 6. The wa.sp records are from the large events and the wa.lp is from a smaller aftershock as indicated in Table 2. Comparing the wa.sp waveforms for a large event with a wa.lp waveforms of a aftershock or smaller event generally shows good agreement as displayed in figure 7. This similarity is produced largely by the differences in faulting area where the distributed nature of the main event tends to produce an integrated effect. This subject becomes interesting because of directivity and the sensitivity of the wa.sp waveforms to fault asperities. We will address these issues in this paper, along with the development of depth phases and the effects of random scatterers in the crustal waveguide.

### Modeling events in the Imperial Valley

We have not had much success in modeling Imperial Valley events with uniform layers, see Ho-Liu and Helmberger (1989). Finite-difference modeling, however, appears to explain some of the observed long period features, see Ho-Liu and Helmberger (1989). Their model is displayed in figure 8 and is based on studying a profile of long-period (30-90) observations along this same corridor. This model allows events occurring in the basin to have prolonged wavetrains at the Pasadena station, PAS while events north of the boundary to have rather sharp pulses, see figure 2.

Synthetics for basin structures can be generated by finite-difference methods following the approach discussed by Helmberger and Vidale (1988). The basic technique is based on the expansion of the complete three-dimensional solution of the wave equation in cylindrical coordinates in an asymptotic form which provides for the separation of the motions into SH and P-SV systems. Closed form expressions appropriate for finite-difference source excitation are obtained from two-dimensional Cagniard-de Hoop theory with rather elaborate near-field terms, see Vidale and Helmberger (1987). Note that the synthetics generated by this mapping preserve the (P-SV) and (SH) systems or two dimension scattering but fail to treat the SV-SH scattering problem which becomes increasingly important at the higher frequencies, see figures 3, 4 and 5.

Profiles of synthetics for the geometry displayed in figure 8 are given in figure 9 for the three pass-bands. The first fifty km of propagation in the slow Imperial Valley structure causes the rapid development of dispersion. After the shallow Lovewave leaves the

basin, it speeds up and disperses more slowly. Three component synthetics generated for a source depth of 12 km appropriate for the 1/28/88 event are given in figure 10. The overall timing looks good but the shorter-periods are not matched well, especially on the tangential component.

Comparing these synthetics with the records of event 1 of the 1987 sequence, trace 4 of figure 6, displays about the same degree of fits as discussed earlier, see Bent et al.(1989) where this event was studied in detail.

Results for the Westmoreland event are given in figure 11. These results are not bad, but the short period complexity becomes very severe for shallower events, as displayed in figure 12. Some progress in explaining the long period motion for very shallow events is given in Ho-Liu and Helmberger (1989) where very slow surface waves in the sediments can be scattered into the coda by valley edge effects. However, generating BB synthetics for these types of models is very expensive relative to analytical techniques and therefore, we will address events occurring to the North of the Imperial Valley in the remaining sections assuming more conventional layered models.

#### Waveform modeling north of the Imperial Valley.

In this section, we will discuss the analytical decomposition of the wavefield in terms of generalized rays, see Helmberger (1983) for a discussion of the method employed. This method allows separation of the wavefield into energy that starts downward relative to upward and isolation of depth phases such as sS. The



latter phase (sS) has potential for source discrimination since explosions are obviously shallow.

First, we examine the behavior of a smooth model followed by that of a coarsely layered model with fewer parameters and discuss their properties when dipping layers are allowed. A particularly effective wavefield decomposition is presented in terms of travel paths: namely,

1. Direct arrival plus surface layer multiples (shallow Love waves)
2. Diving energy paths (lower crustal triplications)
3. Surface reflected paths which turn below the source (sS)

These latter two wave-packets are particularly affected by vertical directivity, as demonstrated by broadband experiments, and behave as if they had different time histories. In short, combining the three contributions with various time shifts which correspond to depth changes or lateral variation allows some extra freedom. Modeling observations with these added parameters becomes much easier as will be demonstrated later.

A velocity model composed of approximately 50 layers and obtained by smoothing a southern California model proposed by Hadley and Kanamori (1979), is given in figure 13. Figure 13 also displays two generalized ray sets used in constructing the wavefield, namely the down-going ray set and up-going ray set (excluding the direct arrival). The upper portion of figure 14 displays the various contributions of these three raysets to the total potential field. These responses were produced by applying the Cagniard-de Hoop

technique to the generalized rays, see Helmberger and Malone (1975). The upper row shows the loss of short-period energy with range as the signal becomes diffracted. The down-going rays or diving rays contribute significantly to the high-frequency content. The moho reflection and head wave complicate the picture, especially due to contributions from sS. The interplay between S and sS changes dramatically when we change mechanism to a dip-slip because of the polarity shift across the horizontal axis.

This feature is easily seen in some preliminary dipping models used in modeling waveform data from the 1969 and 1968 events, see figures 15 and 16. In this situation, we decomposed the rayset into two groups, those containing the direct ray plus multiples in the surface layer (Lovewave) and those diving below the source either directly or following a bounce off the free surface, see figure 15. The direct arrival and diving rays have the same polarity for strike-slip events but opposite in the dip-slip case. For this reason the dip-slip case produces much different looking synthetics as displayed in figure 15.

A comparison of synthetics generated from this dipping model are presented in figure 16 where the depth effects are emphasized by the ray decomposition. Note that in the Coyote Mtn. example, the source depth is 14 km and the shallow Lovewaves become less important. For the shallower Borrego Mtn. event we see a stronger Lovewave contribution. The sSmS phase is especially obvious in the Coyote Mtn. record.

One of the advantages in working with large events in developing a model is the constraints on source parameters obtained

from the teleseismic modeling of body waves. The Coyote Mtn. event appears very simple teleseismically and occurred at the relatively deep depth of 14 km, see Bent and Helmberger (1991a). A disadvantage of large events is seen in the Borrego Mtn. case where the source contains at least two spikes. This complexity is clear in the teleseismic results as well, see Ebel and Helmberger (1982).

The dipping model discussed above was derived in conjunction with a cross-section running from Imperial Valley to Pasadena as displayed in figure 8. The model predicts synthetic that fit these waveforms quite well, although it is poorly constrained. In fact, there are only three principal pulses controlling these waveforms at this range. They are the shallow Lovewave, SmS and sSmS. Since a flat-layered model has a broader applicability, we will address such a model next.

Unfortunately, we do not have a profile of shear wave observations from a calibrated event and, thus, we must constrain the model from other sources and keep the parameters to a minimum. Our preferred model is given in Table 3 and has just five layers, similar to Hadley and Kanamori (1979). Here the gradient at the top of the model given in figure 13 was replaced by a single layer with a thickness of 4 km. This thickness was adopted from a study of local events recorded at PAS where a single-layered model fits the three component data very well, see Dreger and Helmberger (1990). The smooth positive gradient at mid-depths displayed in figure 13 was replaced by a single layer with velocity 3.6. This is consistent with studies from NTS to Tucson; see for example, Langston and Helmberger (1974). The transition zone at the base of

the crust was added to reduce the strength of the moho triplication as suggested by the P-wave data, (Hadley and Kanamori (1979).) The problem discovered in modeling the waveforms is that of preventing the moho triplication from completely overwhelming the relative weak arrival from the nearly constant velocity crust.

Applying the above constraints and varying the thickness to match the timing and waveshapes produced the model given in Table 3. Synthetics appropriate for this model are displayed in figure 17 along with a decomposition which proves useful in modeling near-regional data. The first-column shows the development of the Love wave associated with the surface layer. Note that it also contains the direct arrival. The second column gives the results contributed by the down-going arrivals and the third displays the build up of sS. It is clear that the direct wave plus the surface multiples dominate the motions at epicentral distances less than 100 km. This feature was observed and modeled earlier by Helmberger and Malone (1975) for the Morgan Hill earthquake in central California.

Most of the San Jacinto events occurred near distances at 200 km where all three raysets contribute, sometime destructively and sometime constructively. Adding random velocity anomalies to the various crustal layers produces shifts in timing between these groups, which in turn yields dramatic high frequency effects as discussed in the next section.

Changing the source depth also has a strong effect on the excitation of Lovewaves and on the separation in arrival times between S and sS. Figure 18 displays the depth sensitivity appropriate for a distance of 205 km, where we show BB, long-period

and short period Wood-Anderson synthetics. The phase sS is the most obvious for deep events where the Lovewaves are the weakest and less interference occurs.

Application of the decomposed wavefield with "time shifts" is presented in figure 19. The fits to the data were obtained by shifting the phase sS back in time by .3 seconds for the 7/02/88 event and .5 seconds for the 5/17/88 event. Although these shifts were applied as rather arbitrary corrections, they can be pictured as upper crustal adjustments for these particular locations. For instance, Hamilton (1970), reports about .4 km of sediments in the Borrego Spring Valley near the epicenter of the 5/17/88 event. Thus, sS would be delayed about .5 seconds relative to the diving energy in accordance with the .5 sec. lag applied. These two events were sufficiently small to treat as point sources and apply a simple trapezoid time history, namely  $\delta t_1$ ,  $\delta t_2$  and  $\delta t_3$  yielding .2, .4, and .2 seconds for both events. Their moment estimates are  $4.5 \times 10^{21}$  ergs for the 7/02/88 event and slightly smaller for the 5/17/88 earthquake,  $4.5 \times 10^{21}$  ergs. Since we have, presently, only one broad-band instrument we must treat these moment results as preliminary estimates.

For larger events, we expect considerably more complications involving both directivity and a slip distribution containing asperities. Figure 20 displays predicted synthetics for a number of rupture geometries. A point source synthetic is included for comparison. The case of forward rupturing event is nearly the same as the point source if the rupture velocity is near the body velocity as usually assumed. Rupturing away from the receiver produces a strong reduction in short period signals, as expected. Downward

rupture tends to enhance the moho reflection while rupture upward strengthens sS. Since both the waveshapes and relative short period to long period amplitude ratios are so sensitive to rupture direction it would appear that broad-band data will prove particularly useful for the purpose of studying rupture direction.

If we scale the motions given in figure 20 to those appropriate for the 69 event discussed earlier with a  $M_0=4.8 \times 10^{24}$  from Bent and Helmberger (1991a) we obtain an estimate of 168 cm for the case of upward rupture. The observed peak motions were 53 cm and the waveform fit is quite good, see figure 21. A 30% strength of short period energy release to long period level is about the average behavior of many California earthquakes, (Bent and Helmberger (1991b)). However, to avoid biasing this estimate by directivity, we clearly require multiple samples in different locations, as demonstrated in figure 20. This will be possible in a few years with modern instrumentation, at least in California with the installation of Terrascope.

### Numerical Scattering Experiments

The introduction of laterally varying structure causes considerable interference between the three ray-groups discussed earlier. This is especially true at the larger ranges where the summation has about the same amplitude as each individual group. In this section, we discuss the theoretical results from models containing random scatterers embedded in the various layers. We are particularly concerned with the development of high frequency coda, and with amplitude decay with distance.

The model and geometrical setup is displayed in figure 22. We investigated four situations with variation allowed in particular layers; namely RMOHO (thin layer at the top of the mantle), RSURF (surface layer only), RBOTH (bottom transition layer) and RALL (variations in all the layers). The scattering model follows the scheme discussed by Frankel and Clayton (1984) where a Gaussian correlation function with correlation distances (X) in the vertical and (Y) in the horizontal dimensions is applied. Variations in velocity are up to 20%. Locations of variation are random and their positions are indicated in the above figure. Variations of this size have been suggested by Frankel and Clayton (1984) and others and are probably on the high side.

The complete wave-field was generated for these models ranging in distance from 50 to 275 km at intervals of 5 km with frequencies up to about 2 Hz. We will concentrate primarily on the cross-over ranges as displayed in figure 23 for the SH field. The synthetics displayed on the left are difficult to distinguish from the synthetics discussed earlier from the homogeneous model, see figure 17. The next three columns of the above figure shows the effects of adding random scatterers to the various crustal layers. Scatterers in the top layer show a much stronger effect than do those in the bottom crustal layer (3.75 km/sec) since the second and third columns are nearly the same. Adding in scatterers in the main crustal layer (3.6 km/sec) causes the strongest distortions. The relative amplitude variation across the various rows reflects primarily the velocity at the receiver which is the same for the three columns on the right.

It becomes difficult to interpret these complex waveforms since we can no longer decompose the waveform into subgroups, though we can still identify some of the more important phases such as  $S_mS$  and  $sS_mS$ . A brief review of figure 17 indicates that  $sS_mS$  becomes strong near 200 km and  $S_mS$  and  $sS_mS$  are particularly obvious at the ranges 170 and 185 in the first three columns. Direct  $S_mS$  becomes less strong in the most severe case given on the right. Apparently as the ray paths flatten, they become more sensitive to lateral variation as one would expect and the multiples which travel more nearly vertical become important.

The introduction of random scatterers into the surface layer produced significant amplitude anomalies in the tangential case but did not greatly increase the coda which is so commonly observed in regional data. The effects on the (P-SV) system are more dramatic as displayed in figure 24. Synthetics for the RMOHO case are displayed on the left for comparison. Note the simplicity of the P arrivals, essentially  $P_mP$  and  $pP_mP$ , which are not affected much by the shallow velocity anomalies, nor are the corresponding SV phases.

Significant short period scattering occurs following SV which is apparently caused by the interaction of the Rayleigh wave with the irregular fine structure near the surface. The latter contributes to the mysterious Lg phase which is prevalent on short period regional records. Convolution of the broad-band SH responses of figure 23 with a (wa.sp) instrument yields similar looking records, but showing considerable modulation in amplitudes, as displayed in figure 25.

The amplitude fall-off or attenuation as determined by the strong-motion community reflects the choice of crustal model. The



thick mid-crustal layer of velocity (3.6 km/sec) is probably quite common in western United States and is responsible for the rapid decay between 50 to 90 km. The increase at larger ranges is influenced by the lower crustal transition and the sharpness of the moho. Note that these amplitudes are also influenced by radiation pattern. These plots are appropriate for the strike-slip case which is the most common type observed along the San Jacinto fault system.

The strong arrival at the range of 105 km in the full-scattering model is caused by constructive interference between the moho reflection and first multiple in the top layer (Love wave). In general, the strong scattering introduced in this exercise was sufficient to obscure the moho reflection, but the possibility of large motions near the moho-cross over is hard to avoid.

The increased amplitudes near 100 km, as discussed here, are not apparent in most strong-motion datasets. However, this may reflect the prevalent processing methods normally applied; where one truncates the range of interest at the first strong-motion station that does not trigger. In light of the strong motions observed in San Francisco for the Loma Prieta (1989) earthquake, (Somerville and Yoshimura, 1990) and observations from the Saguenay earthquake (1988), Somerville et.al (1990), this subject should probably be revisited.

### Conclusions

This paper investigates BB wave propagation along a corridor in Southern California from the Imperial Valley to Pasadena. Seismograms from Imperial Valley events are characterized by SH

waves which appear dispersed, and possess well-developed codas. Rayleigh waves are dispersed and relatively strong compared to body phases. These features can be modeled with a finite-difference code at periods greater than a few seconds by assuming the following two-dimensional model; a slow basin with a shallow moho followed by a thick crust. Propagating 50 km in the basin is sufficient to disperse the wave-field. Shallow sources apparently excite the surface waveguide where the field travels slowly to the edge of the valley. There it is re-radiated very strong coda signatures. It appears difficult to propagate the wave-field across boundaries of this type by present analytical techniques.

Modeling events at smaller ranges in the normal crust proved possible with analytical codes. In these codes, a decomposition of the wavefield into the following individual phases was useful: direct S and Love, diving S and sS in the tangential case. Shifts in  $S_mS$  relative to s $S_mS$  of a few tenths of a second allow excellent fits in BB records in many situations. Directivity plays an important role in the sharpness of these phases which adds to the richness in modeling BB regional phases. At these ranges the Moho critical angle reflections contribute the strongest peak amplitudes, at least in flat-layered models. Numerical experiments conducted with the inclusion of scatterers into the various layers did not change this result. Scatterers in the surface layer produce signals which resemble typical Lg phases, at least as observed on the vertical component waveform.

In conclusion, it appears possible to model depth phases such as sS in tectonic regions with analytical methods if major geological

boundaries are not crossed. Secondly, the ratio of S to Love waves can be used to estimate source depths if paths are calibrated. Future efforts will include the application of source inversion techniques to these type of records.

#### Acknowledgments

We would like to thank Laura Jones, Larry Burdick and Hiroo Kanamori for their reviews. This research was supported by the Advanced Research Projects Agency of the Department of Defense and was monitored by the Air Force Geophysical Laboratory under the contract F19628-89-K-0028. Contribution No. 4987, Division of Geological and Planetary Sciences, California Institute of Technology, Pasadena, California.

## References

- Bent, A. L., D. V. Helmberger, R. J. Stead, and P. Ho-Liu, 1989. Waveform modeling of the November 1987 Superstition Hills earthquakes, *Bull. Seism. Soc. Am.*, **79**, 500-514.
- Bent, A. L. and D. V. Helmberger (1991a). A re-examination of historic earthquakes in the San Jacinto fault zone, California, submitted *Bull. Seism. Soc. Am.*
- Bent, A. L. and D. V. Helmberger (1991b). Seismic characteristics of earthquakes along the offshore extension of the western transverse ranges, California, in press, *Bull. Seism. Soc. Am.*
- Burdick, L. J., C. K. Saikia, and N. F. Smith, 1991.  $P_n$  for the Nevada Test Site, *AGU Monograph on Explosion Source Phenomenology*.
- Dreger, D. and D. V. Helmberger, 1990. Broad-band modeling of local earthquakes. *Bull. Seism. Soc. Am.*, **80**, 1162-1179.
- Ebel, J. E. and D. V. Helmberger, 1982. P-wave complexity and fault asperities: The Borrego Mountain, California, earthquake of 1968, *Bull. Seism. Soc. Am.*, **72**, 413-437.
- Flatte, S. M. and R. S. Wu, 1988. Small-scale structure in the lithosphere and asthenosphere deduced from arrival times and amplitude fluctuations at NORSAR, *J. Geophys. Res.*, **93**, 6601-6614.
- Frankel, A. and R. W. Clayton, 1984. A finite difference simulation of wave propagation in two-dimensional random media, *Bull. Seism. Soc. Am.*, **74**, 2167-2186.
- Hadley, D. and H. Kanamori, 1979. Regional S-wave structure for southern California from the analysis of teleseismic Rayleigh waves, *Geophys. J. R. astr. Soc.*, **58**, 655-666.
- Hamilton, R. M., 1970. Time-term analysis of explosion data from the vicinity of the Borrego Mountain, California earthquake of 9 April, 1968, *Bull. Seism. Soc. Am.*, **60**, 367-381.
- Helmberger, D. V. and S. D. Malone, 1975. Modeling local earthquakes as shear dislocations in a layered half space, *J. Geophys. Res.*, **80**, 4881-4888.
- Helmberger, D. V. 1983. Theory and application of synthetic seismograms, In *Earthquakes: Observation, Theory and Interpretation*, *Proc. Int. Sch. Phys. "Enrico Fermi" Course LXXXV*, (eds. Kanamori, H. and Boschi, E.)(North-Holland Publ., Amsterdam) pp. 174-221.
- Ho-Liu, P. and D. Helmberger, 1989. Modeling regional love waves: Imperial Valley to Pasadena, *Bull. Seism. Soc. Am.*, **79**, 1194-1209.

- Kennett B.L.N., 1989. Lg-wave propagation in heterogeneous media, *Bull Seism. Soc. Am.*, **79**, 860-872.
- Kennett B. L. N., 1989. On the nature of regional seismic phases I - phase representations for Pn,Pg,Lg, and Sn, *Geophysical Journal*, **98**, 447-456.
- Langston, Charles A. and Donald V. Helmberger 1974. Interpretation of body and rayleigh waves from NTS to Tucson, *Bull Seism. Soc. Am.*, **64**, No. 6, 1919-1929.
- Romanowicz, B., 1982. Lateral heterogeneity in continents; moment-tensor inversion of long-period surface waves and depth resolution of crustal events; body-wave modeling and phase-velocity calibration, *Phys. of the Earth and Plan. Int.*, **30**, 269-271.
- Somerville, P. G. and J. Yoshimura, 1990. The influence of critical Moho reflections on strong ground motions recorded in San Francisco and Oakland during the 1989 Loma Prieta earthquake, *Geophys. Res. Lett.*, **17**, 1203-1206.
- Somerville, P. G., J. P. McLaren, Saikia, C. K. and D. V. Helmberger, 1990. The November 25, 1988 Saguenay, Quebec earthquake: Source parameters and the attenuation of strong ground motion, *Bull. Seism. Soc. Am.*, **80**, 1118-1143.
- Stead, R. J., (1989). Finite Differences and a Coupled Analytic Technique with applications to Explosions and Earthquakes, *Phd Thesis*, Caltech, Pasadena, California.
- Vidale, J. E., and D. V. Helmberger, 1987. Path effects in strong motion seismology. (chapter in 1986 volume of *Methods of Computational Physics*, Bruce Bolt, ed.).
- Zhao, L. S., D. Helmberger, 1991. Broadband modeling along a regional shield path, Harvard recording of the Saguenay Earthquake, *Geophysical Journal*. (in press).

Table 1. Crustal model MPM

Layer	1	2	3	4	5	6	7	8	9	10
$\alpha$ km/sec	6.04	6.24	6.30	6.52	6.58	7.90	8.10	8.20	8.27	8.13
$\beta$ km/sec	3.49	3.61	3.70	3.77	3.80	4.60	4.70	4.55	4.723	4.74
Th km	8.0	8.0	8.0	8.0	3.0	10.0	10.0	90.0	35.0	45.0

Table 2. Earthquakes along profile

date	origin time GCT	latitude degrees N	longitude degrees E	depth km	magnitude	distance from Pas.
03/23/54	04.14	33.28	-116.18	16.0	5.1	230 km
04/09/68	02.28	33.18	-116.12	11.0	6.4	224
04/28/69	23.20	33.33	-116.33	20.0	6.1	191
04/26/81	12.09	33.13	-115.65	6.0	5.3	260
11/24/87	01.54	33.08	-115.78	5.0	5.7	251
11/24/87	13.15	33.01	-115.84	2.0	6.0	252
01/28/88	02.54	32.91	-115.68	6.0	4.6	270
05/17/88	19.38	33.24	-116.25	8.0	3.8	205
07/02/88	00.26	33.49	-116.44	12.0	4.1	176
03/06/89	22.16	33.17	-115.59	1.0	4.7	262

Table 3. Normal Southern Cal Crust

Layer	1	2	3	4	5
$\alpha$	5.4	6.2	6.6	7.5	7.8 km/sec
$\beta$	3.2	3.6	3.75	4.1	4.25 km/sec
$\rho$	2.7	2.85	3.2	3.42	3.45 gr/cm <sup>3</sup>
Th	4	16	8	3	km

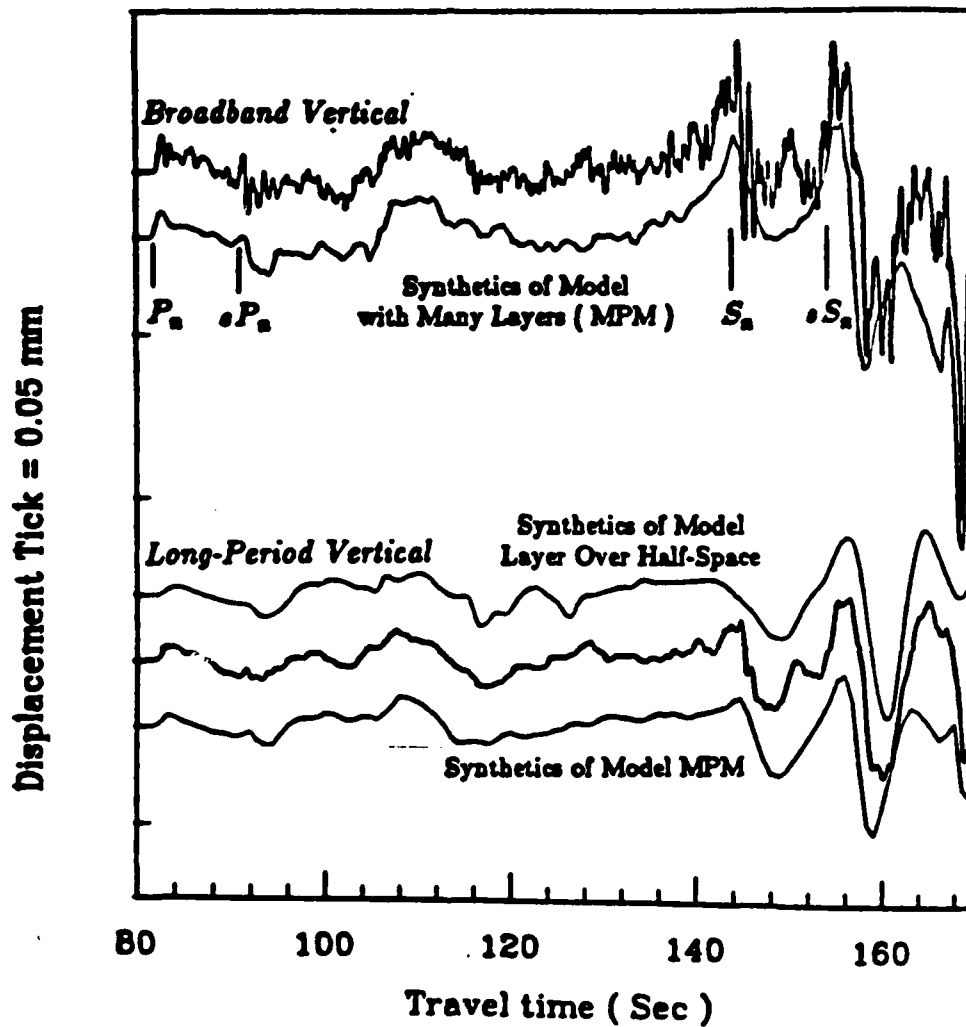


Figure 1. The top pair of traces compares a synthetic with the first 100 sec of the vertical observation of the Quebec earthquake, 11/25/88, as recorded at the Harvard broad-band station,  $\Delta = 625$  km. The lower three traces display the fits after convolving with the WWSSN long period response. The first 30 to 40 secs is composed mostly of P diffracted energy along the top of the mantle,  $P_n$ . The latter 30 secs is composed mostly of SV diffracted energy along the same mantle path,  $S_{n1}$ .

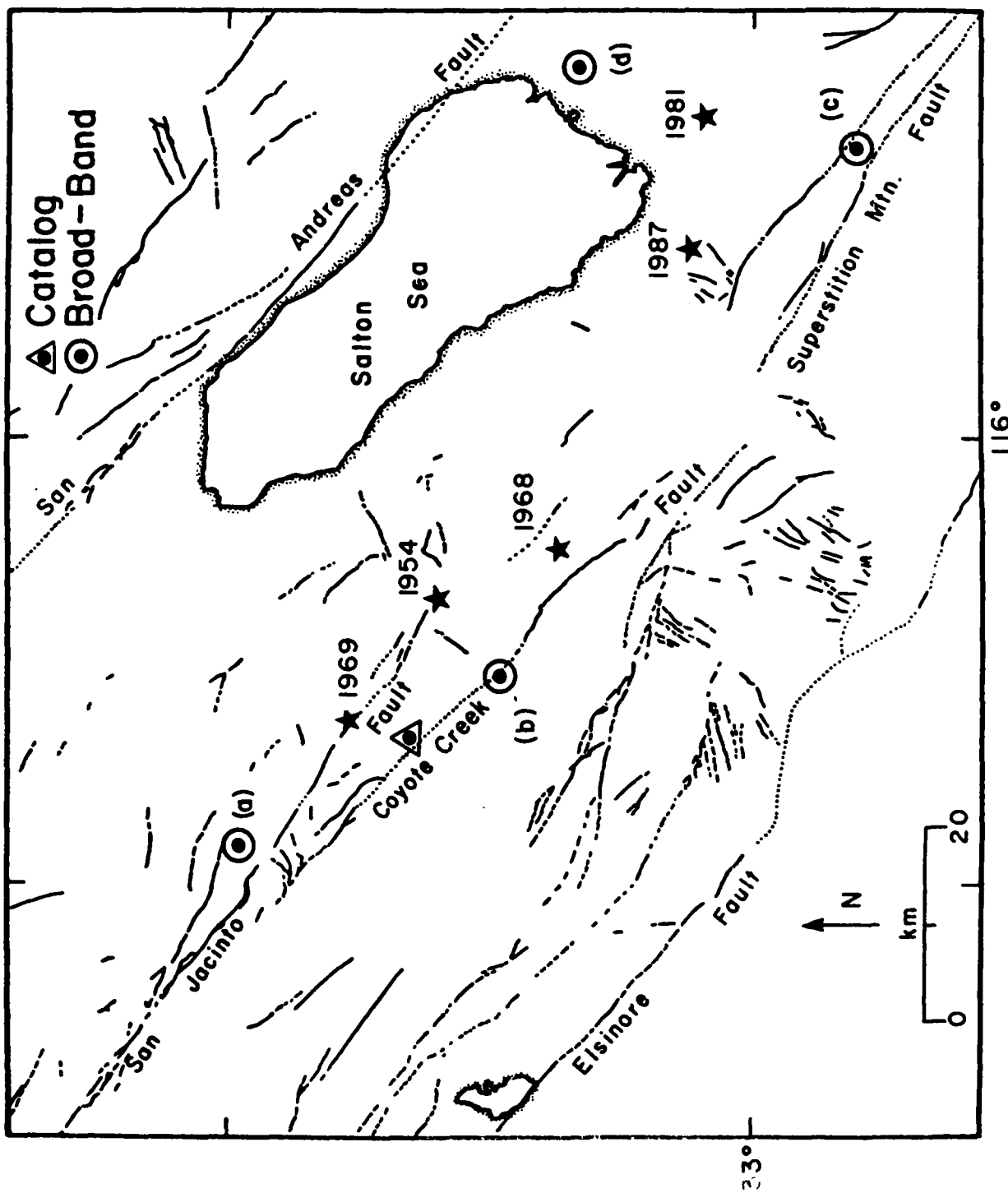


Figure 2. This map displays the locations of a number of events discussed in this paper relative to the extended San Jacinto fault system. The stars indicate relatively large events while the circles indicates smaller recent events recorded by the new IRIS system at Pasadena.



Event: 07/02/88 00:26

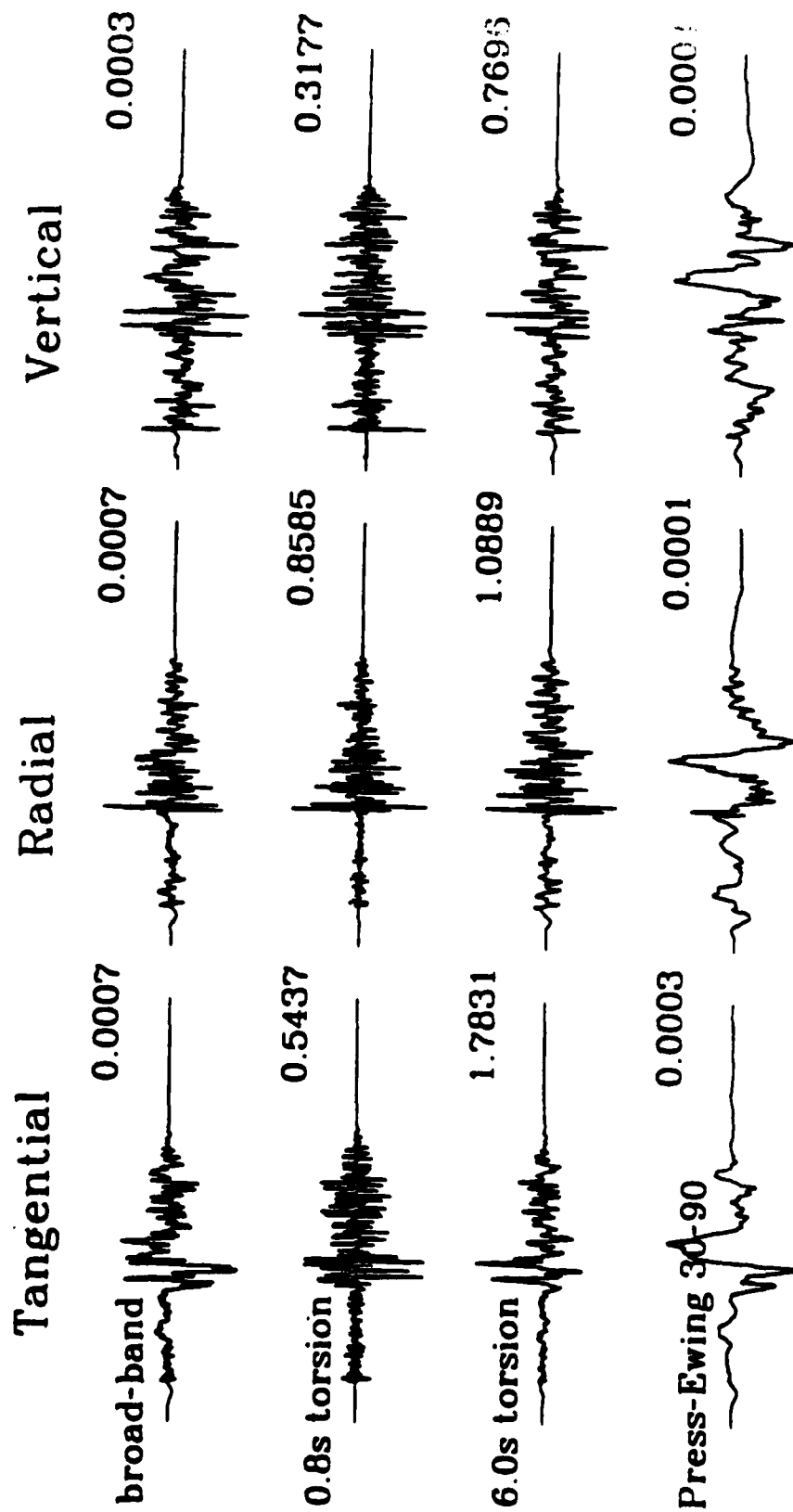


Figure 3. Display of motions recorded from the 7/2/88 magnitude 4 event (a),  $\Delta = 176$  km. Peak amplitudes are given in cm. The gain of the Press-Ewing has been set at one in these simulations.

Event: 05/17/88 19:38

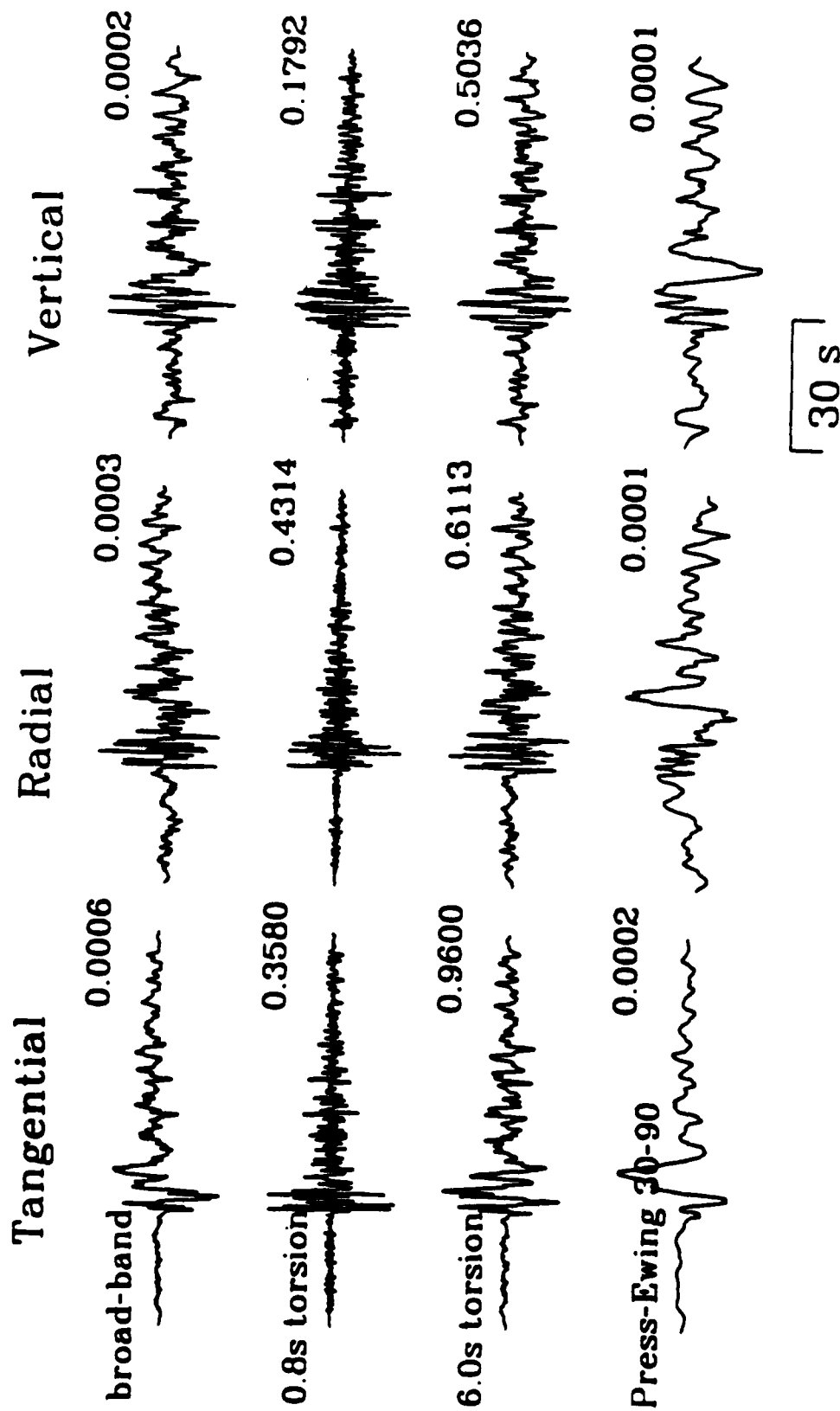


Figure 4. Display similar to that in figure 4 of the 5/17/88 event (b),  $\Delta = 205$  km.

Event: 03/06/89 22:16

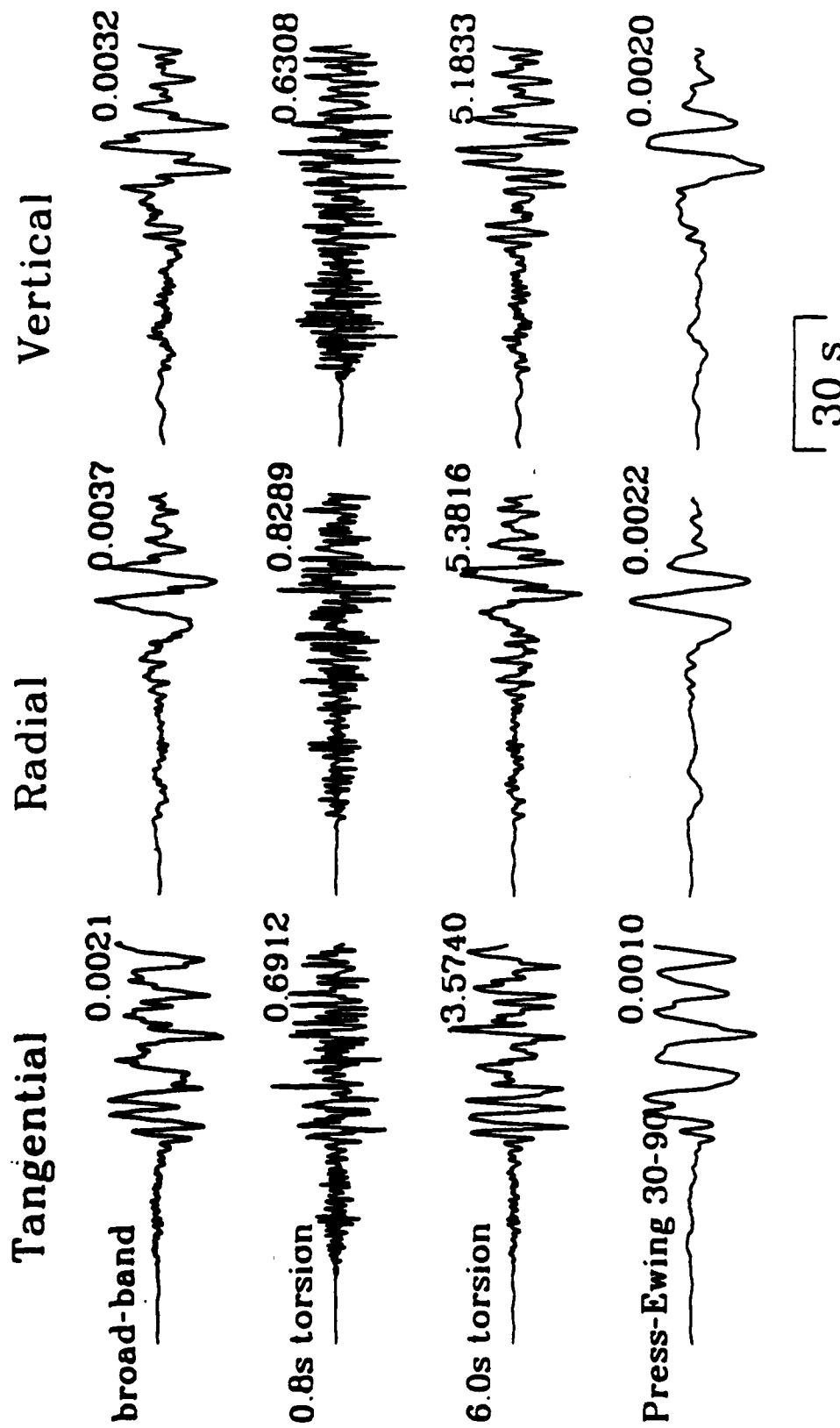


Figure 5. Display similar to that in figure 4 of the Superstition Hills aftershock 1/28/88 event (c).  
 $\Delta = 256$  km.

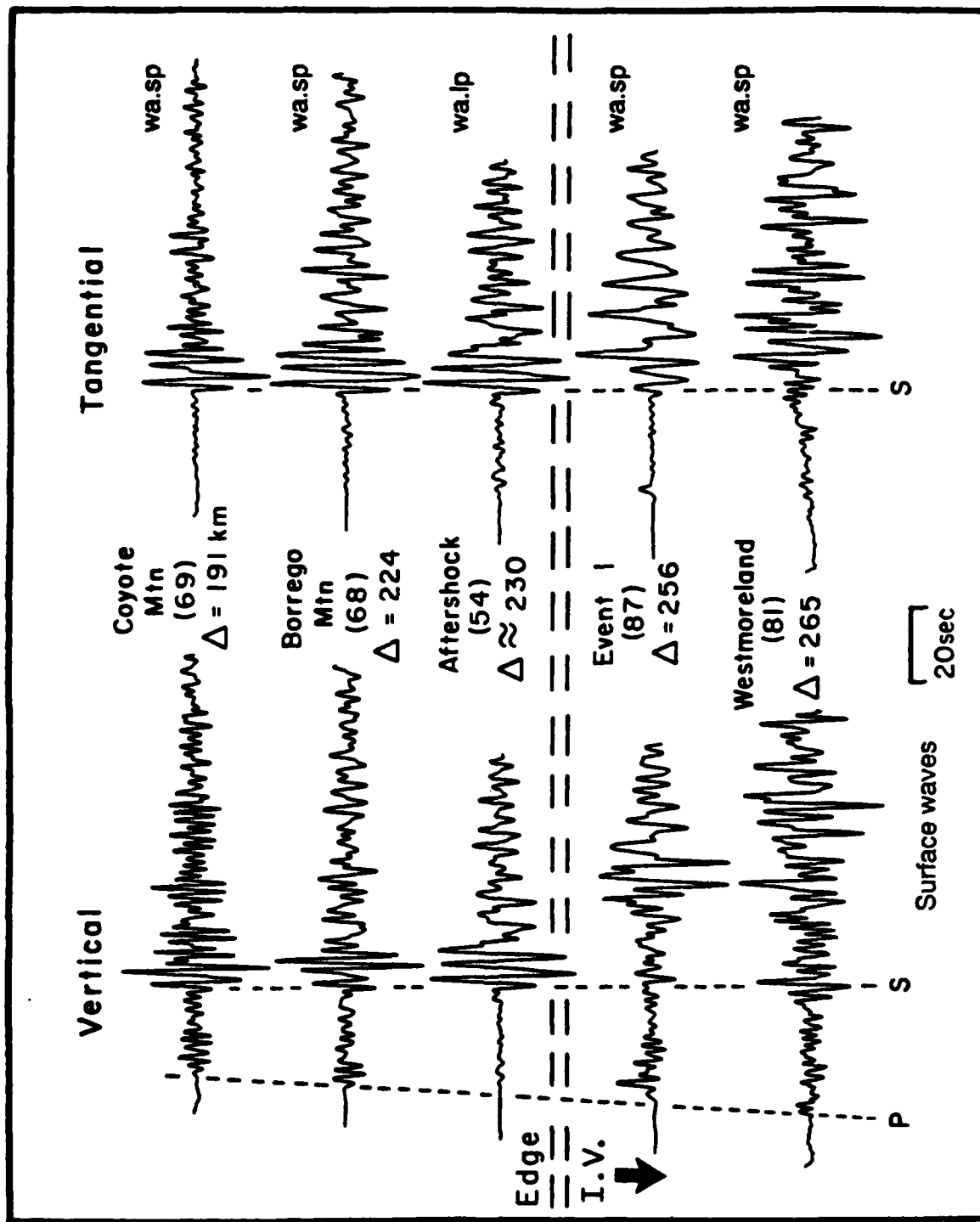


Figure 6. Comparisons of seismograms from the older events as recorded on the low-gain instrument at Pasadena. These records have been hand digitized and rotated. The lower two traces are from the events in the Imperial Valley, see figure 2.

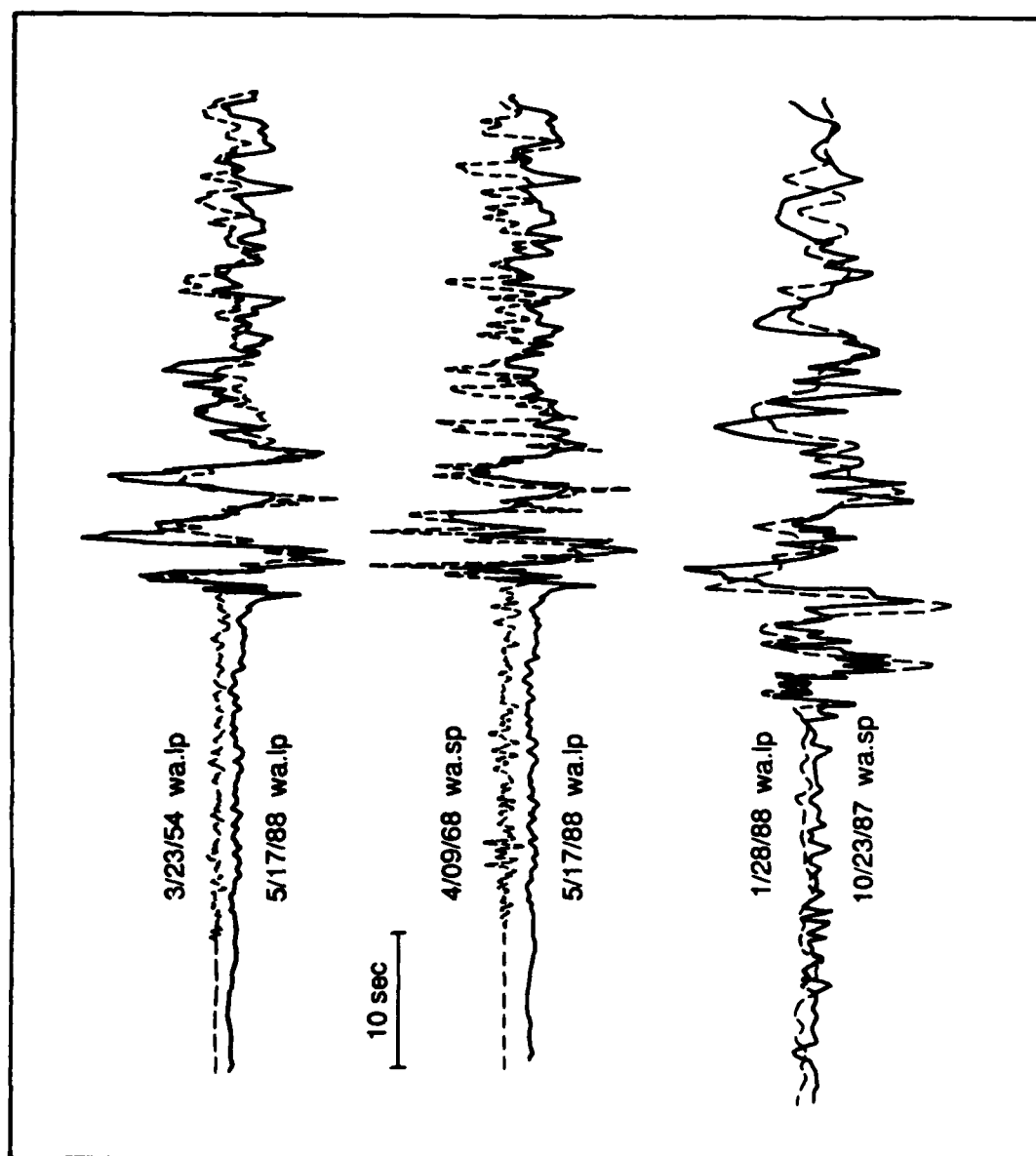


Figure 7. Comparison of tangential motions of large events (wa.sp) with small events (wa.lp).

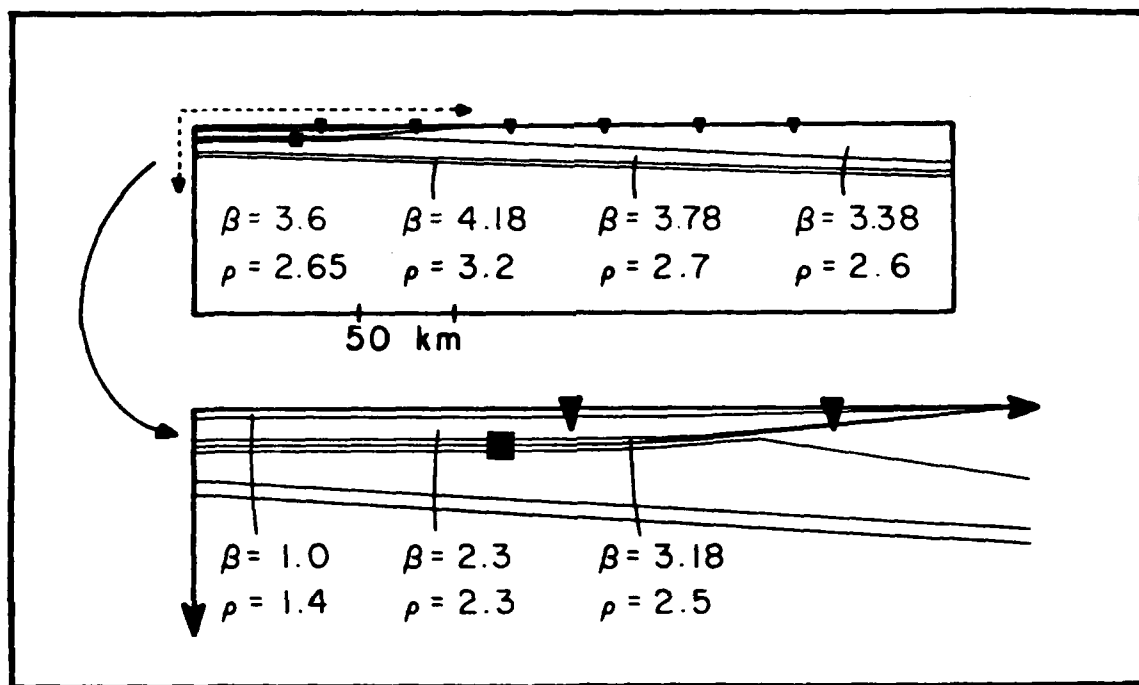


Figure 8. Seismic parameters for a 2D model connecting Imperial Valley to Pasadena, after Ho-Liu and Helmberger (1988).

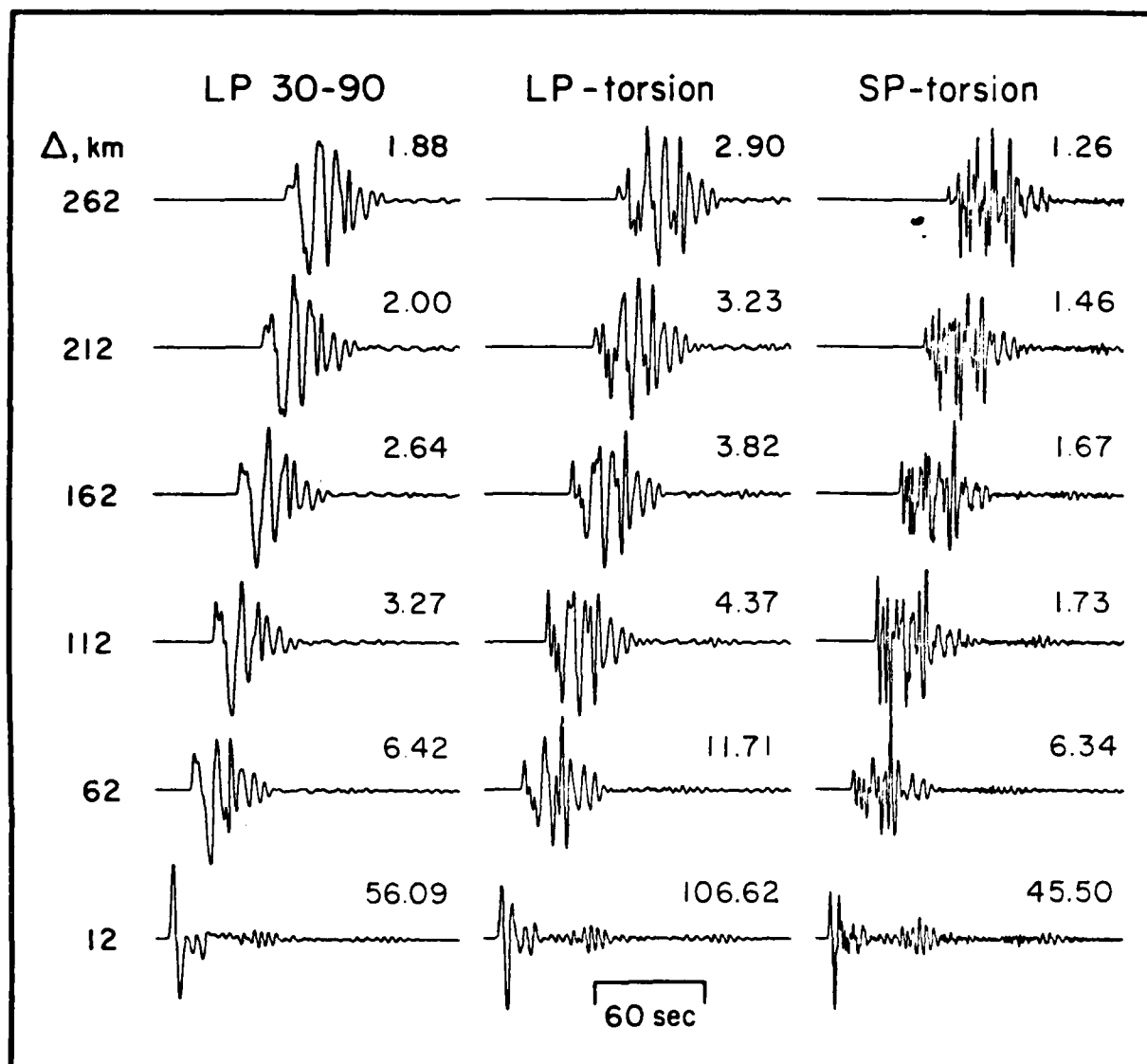
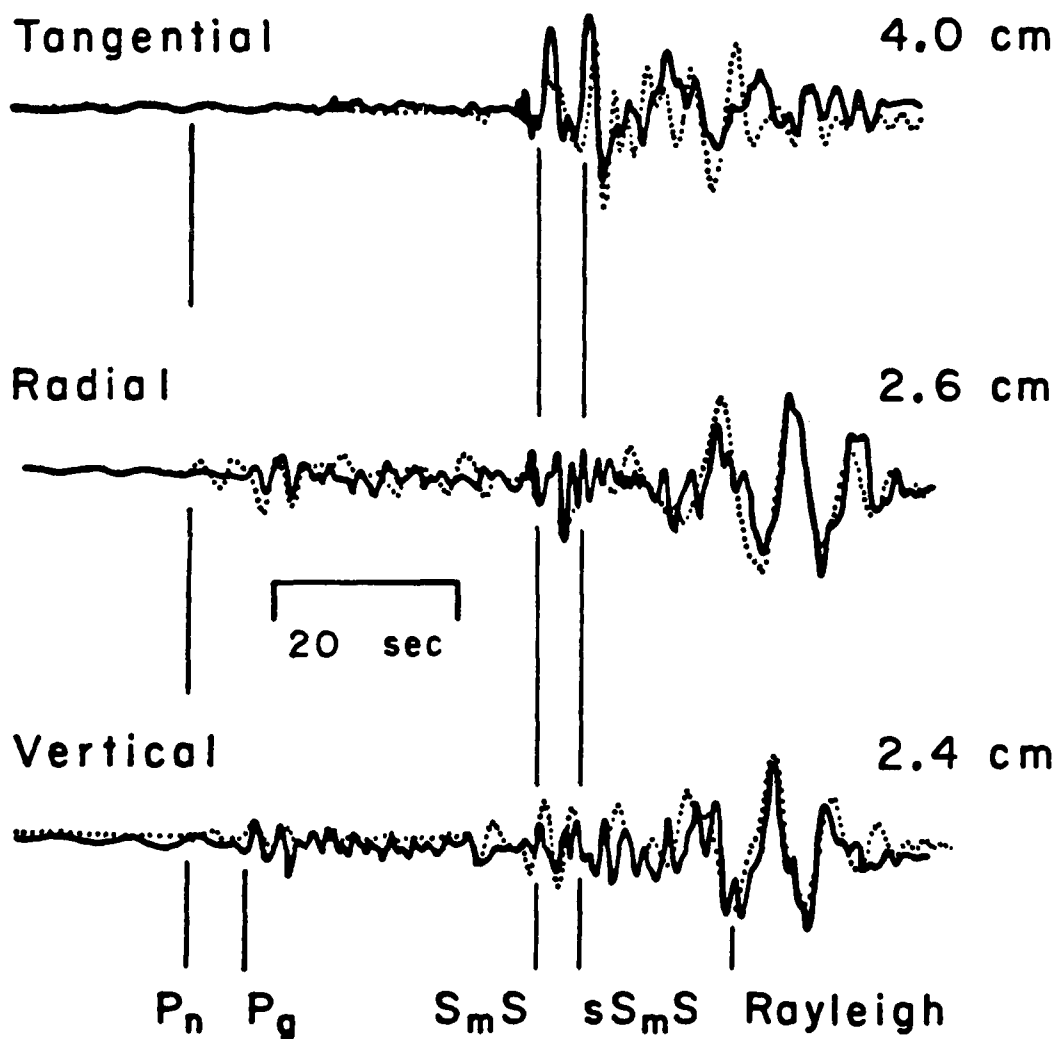


Figure 9. Synthetics appropriate for a strike-slip source beneath Imperial valley ( $d = 7$  km) assuming the model defined in figure 8.

m = 4.9 1/28/88 AFTERSHOCK



$$M_0 \approx 1.1 \times 10^{23} \text{ ergs}$$

Figure 10. Comparison of synthetics and observations for the Superstition Hills aftershock constructed from the model displayed in figure 8 assuming  $\alpha=1.73\beta$ .



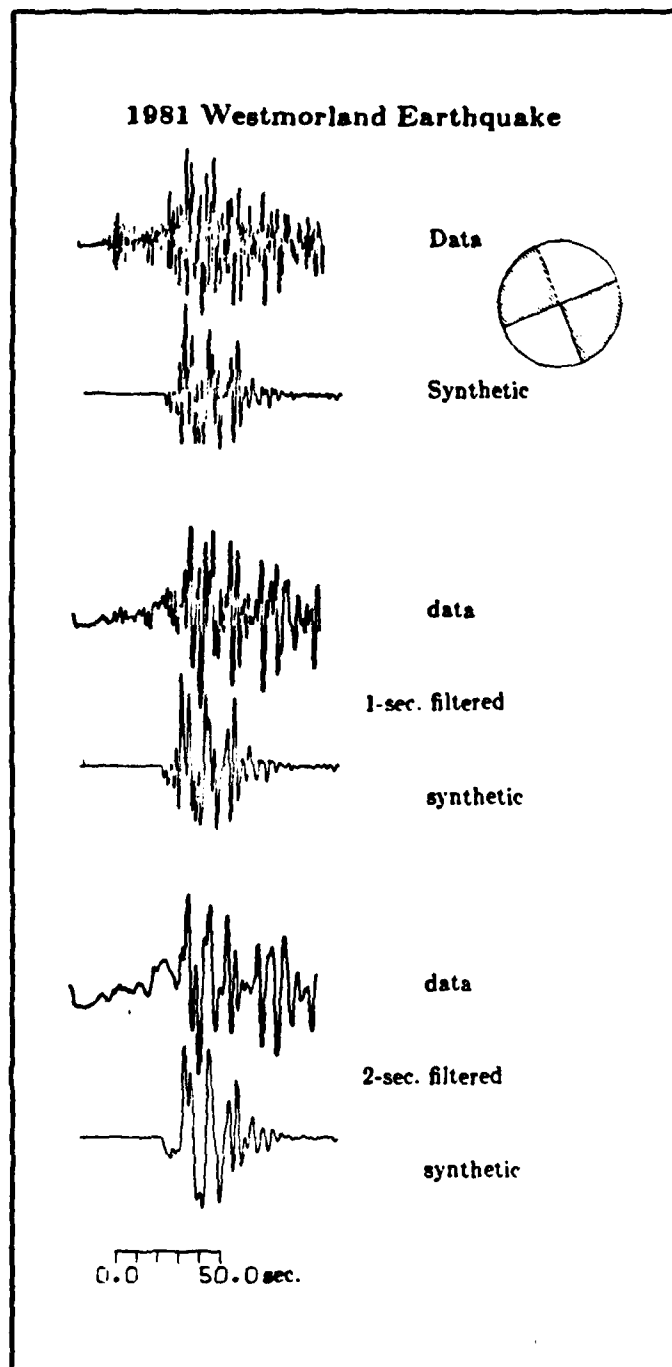


Figure 11. WA (100x) recording from the Westmorland earthquake. Two sources were used in generating the synthetics, one with a  $M_0$  of  $2.5 \times 10^{24}$  dyne-cm at a depth of 7 km and the second one with an  $M_0$  of  $4.5 \times 10^{24}$  dyne-cm at a depth of 10.5 km, delayed by about 2.5 secs. This 2.5 sec. delay is also observed in local strong motion accelerograms. The lower comparisons are made after filtering the synthetics and data by one and two second triangles.

Event: 03/06/89 22:16

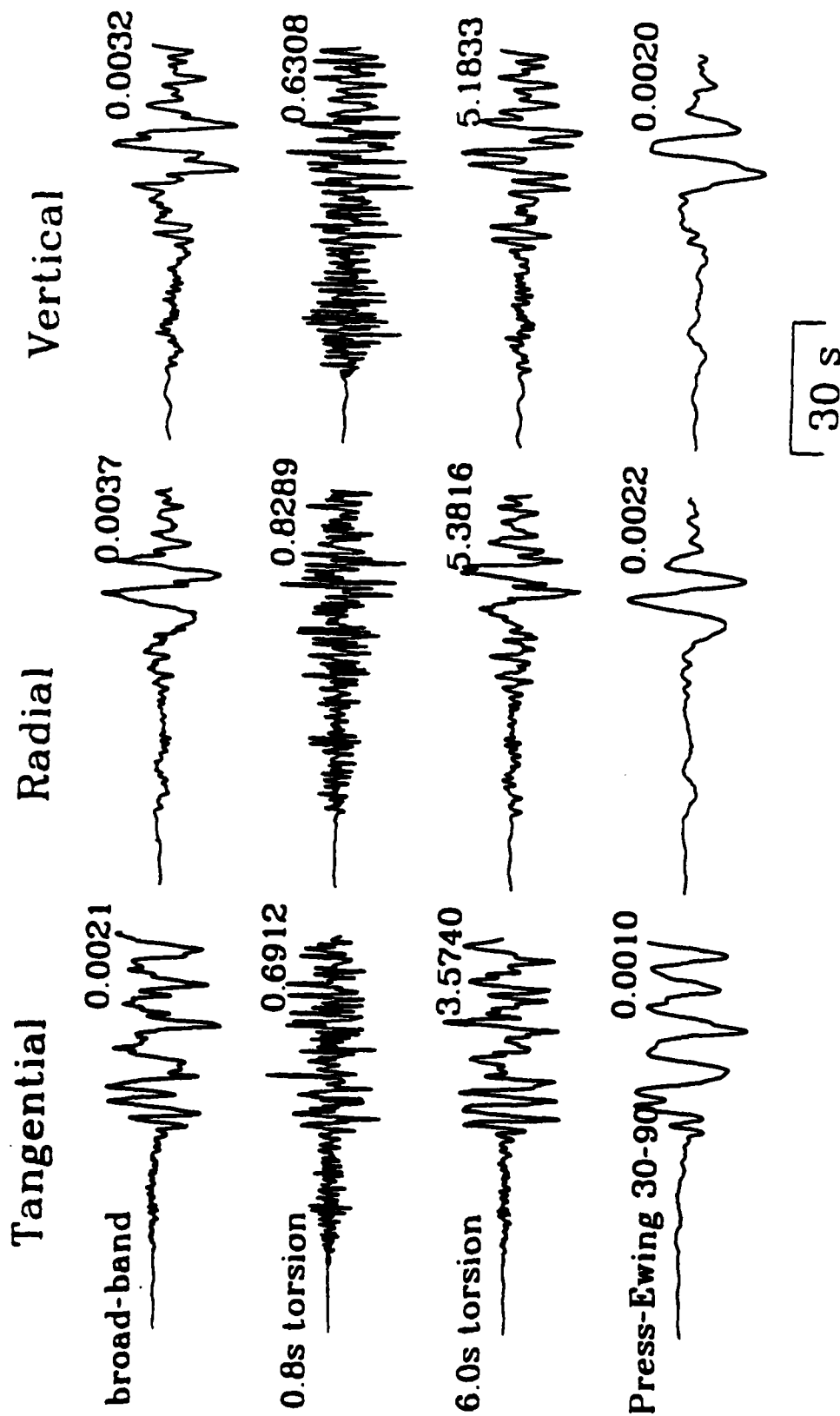


Figure 12. Display of motions recorded from the 3/6/89 event, (d in figure 2) which occurred near the Westmorland event.

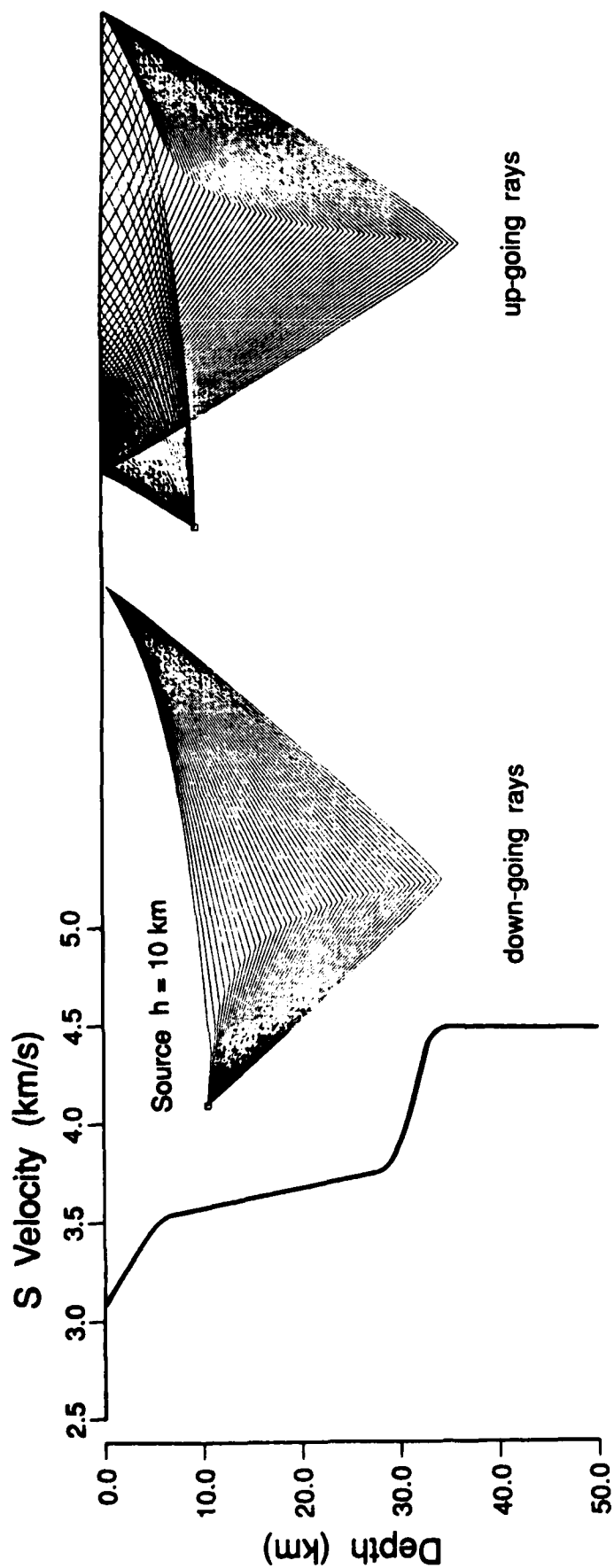


Figure 13. A velocity-depth function is displayed on the left along with generalized ray paths used in the construction of synthetics on the right.

# STRIKE-SLIP

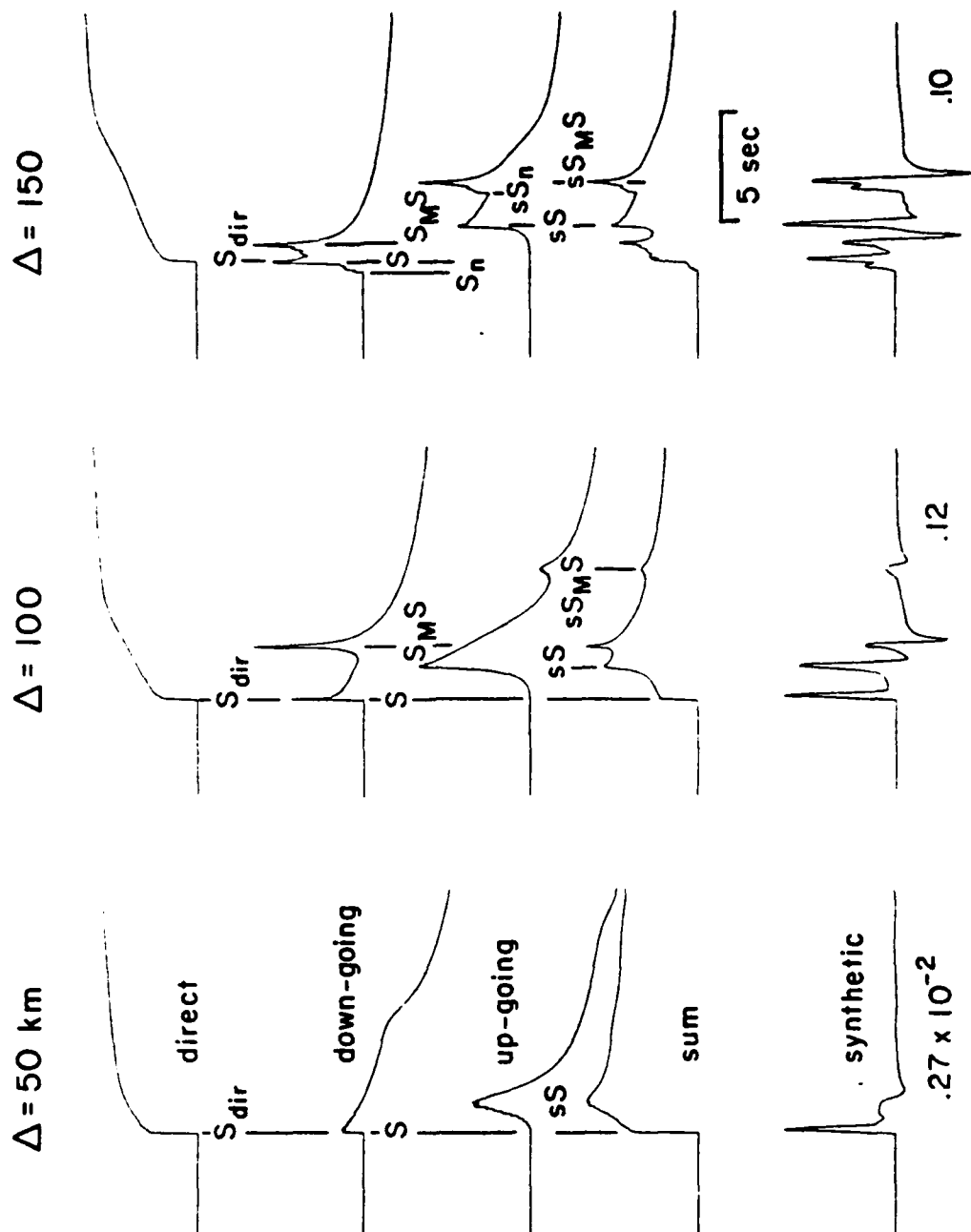


Figure 14. Wave-field decomposition displaying the response of the direct arrival on the top followed by the contribution from down-going paths ( $S$ ) and up-going paths ( $sS$ ). The bottom row displays the synthetic assuming a (.2..2..2) trapezoidal source.

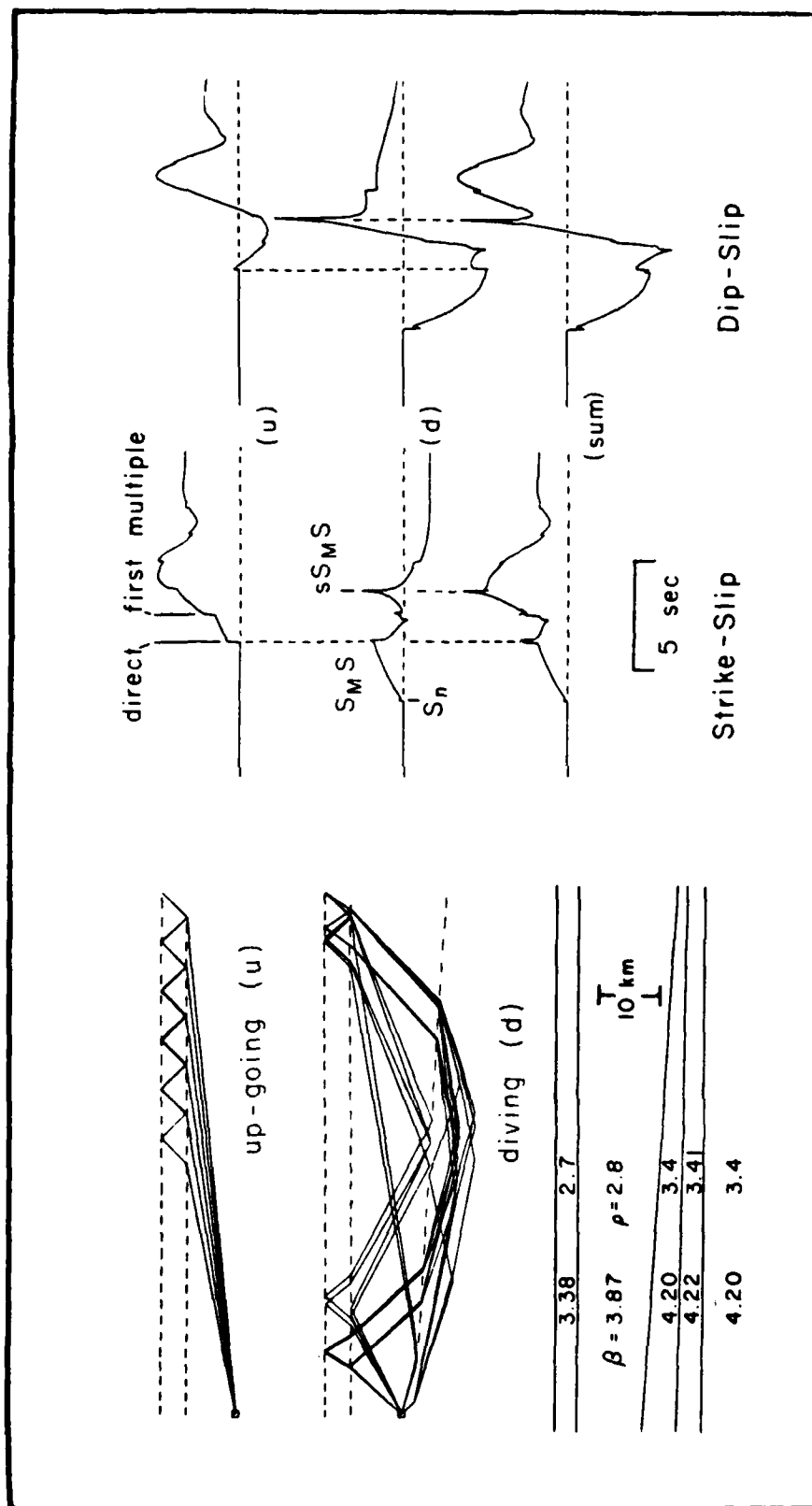


Figure 15. Ray paths and corresponding step-responses for a dipping layered model similar to that displayed in figure 8.

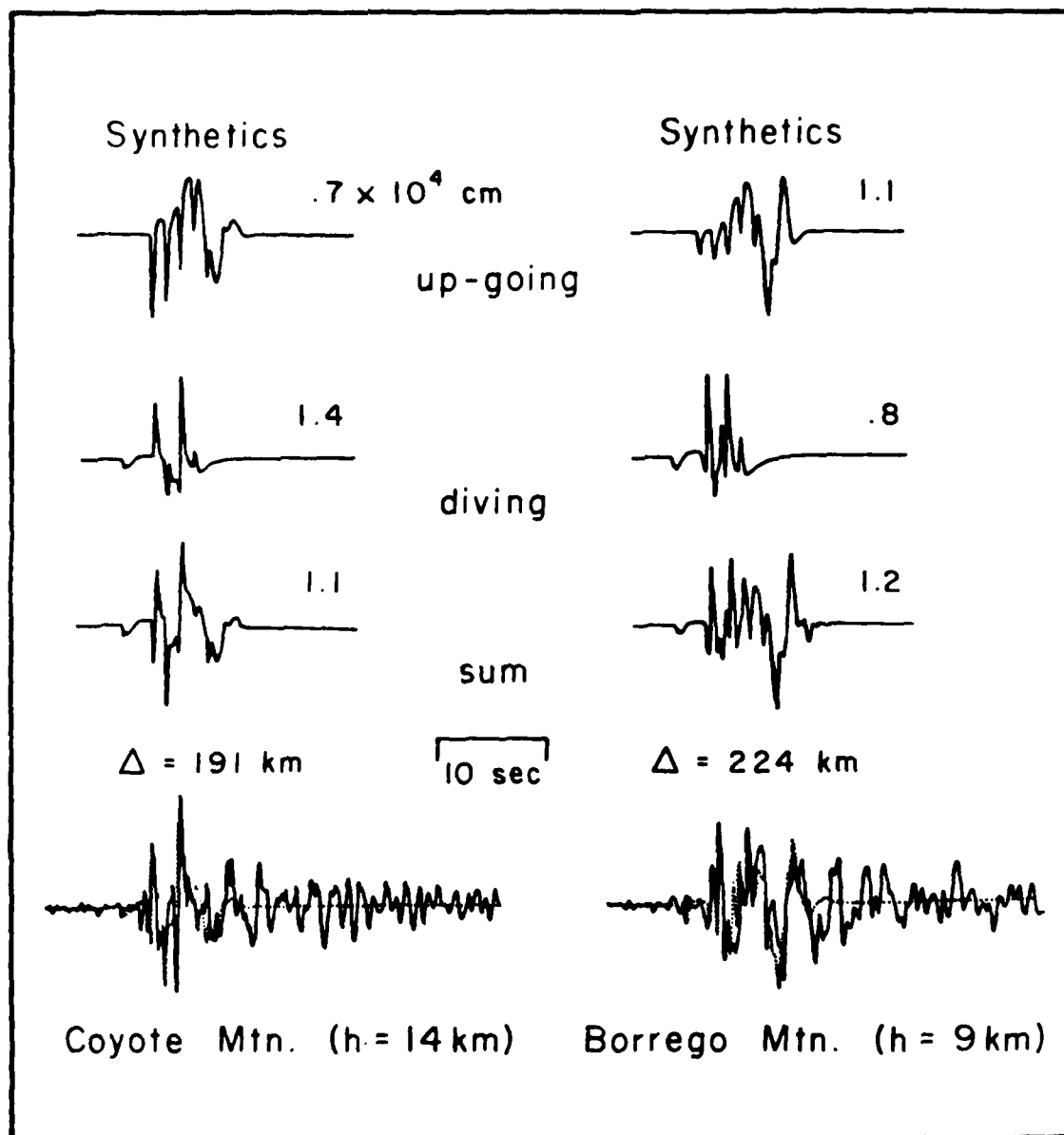


Figure 16. Synthetics constructed from the step-responses (strike-slip) displayed in figure 15 for a range of 191km along with a similar construction for  $\Delta=224$  km. Comparisons with the data is given in the bottom row. The time function for the Coyote Mtn. event consisted of a trapezoid (.2,.2,.2). The time function used in the Borrego Mtn. event consisted of two trapezoids with the same timing where the second is three times the first and lagged .7 secs.

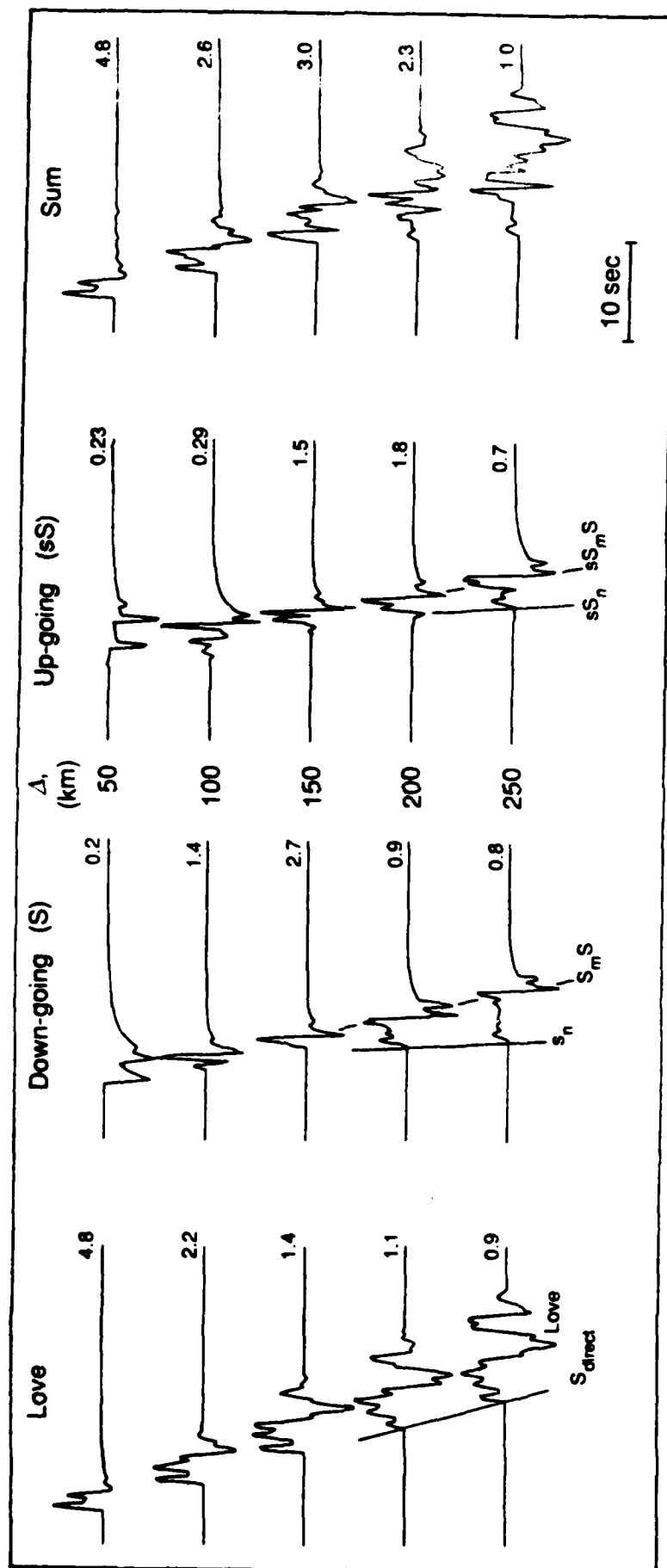


Figure 17. Construction of synthetics from 50 to 250 kms displaying the delicate interference that occurs at the cross-over distances. These synthetics are appropriate for the model presented in Table 3 for a source depth of 10 km, assuming a trapezoidal source (2,2,2).

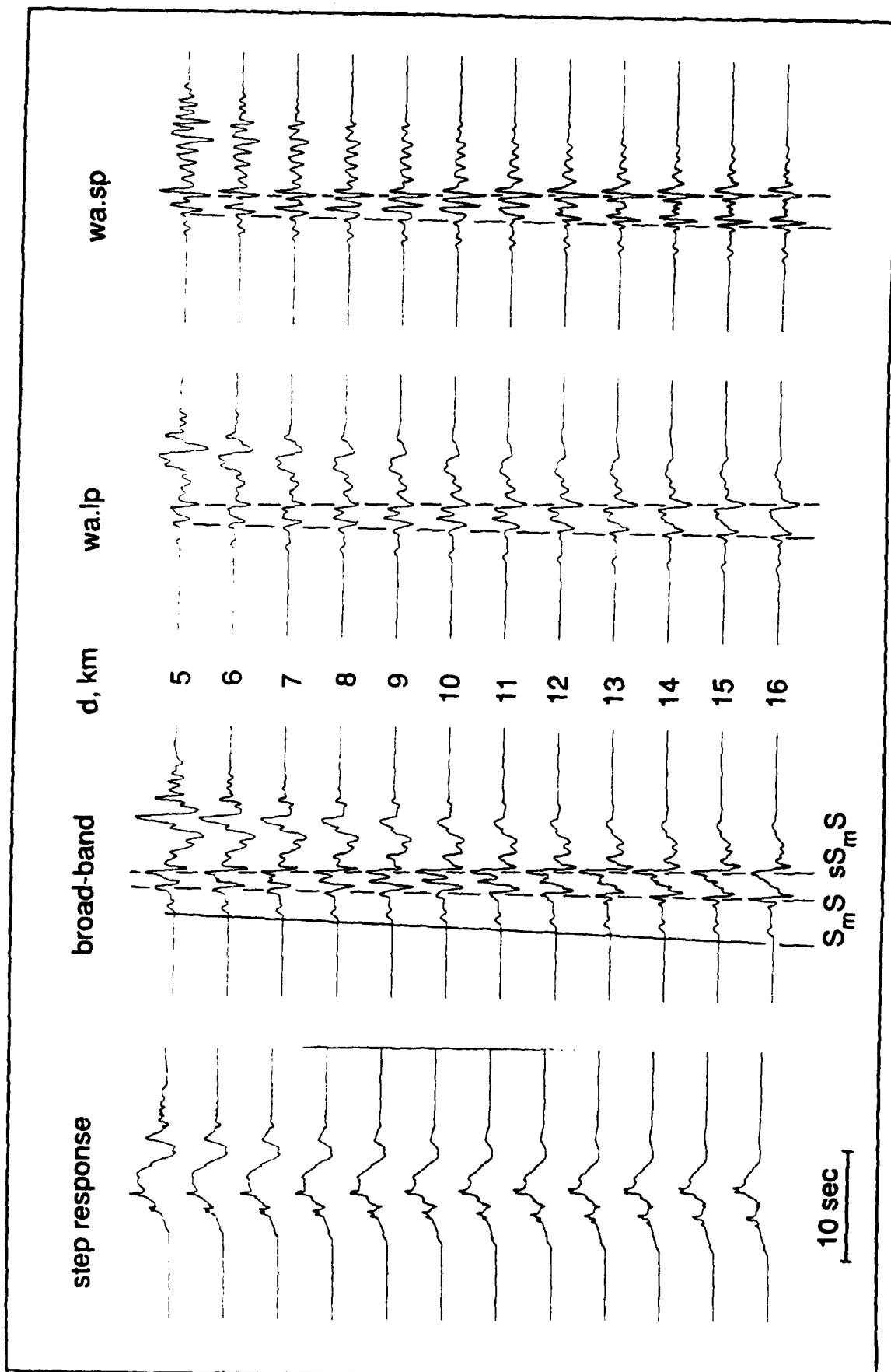


Figure 18. Depth sensitivity sections ( $\Delta=224$  km) showing the domination of the Love wave at shallow source depths. The solid line indicates the Sn arrival and the dashed the mocho reflection (SmS) and corresponding surface reflected phase (sSmS).



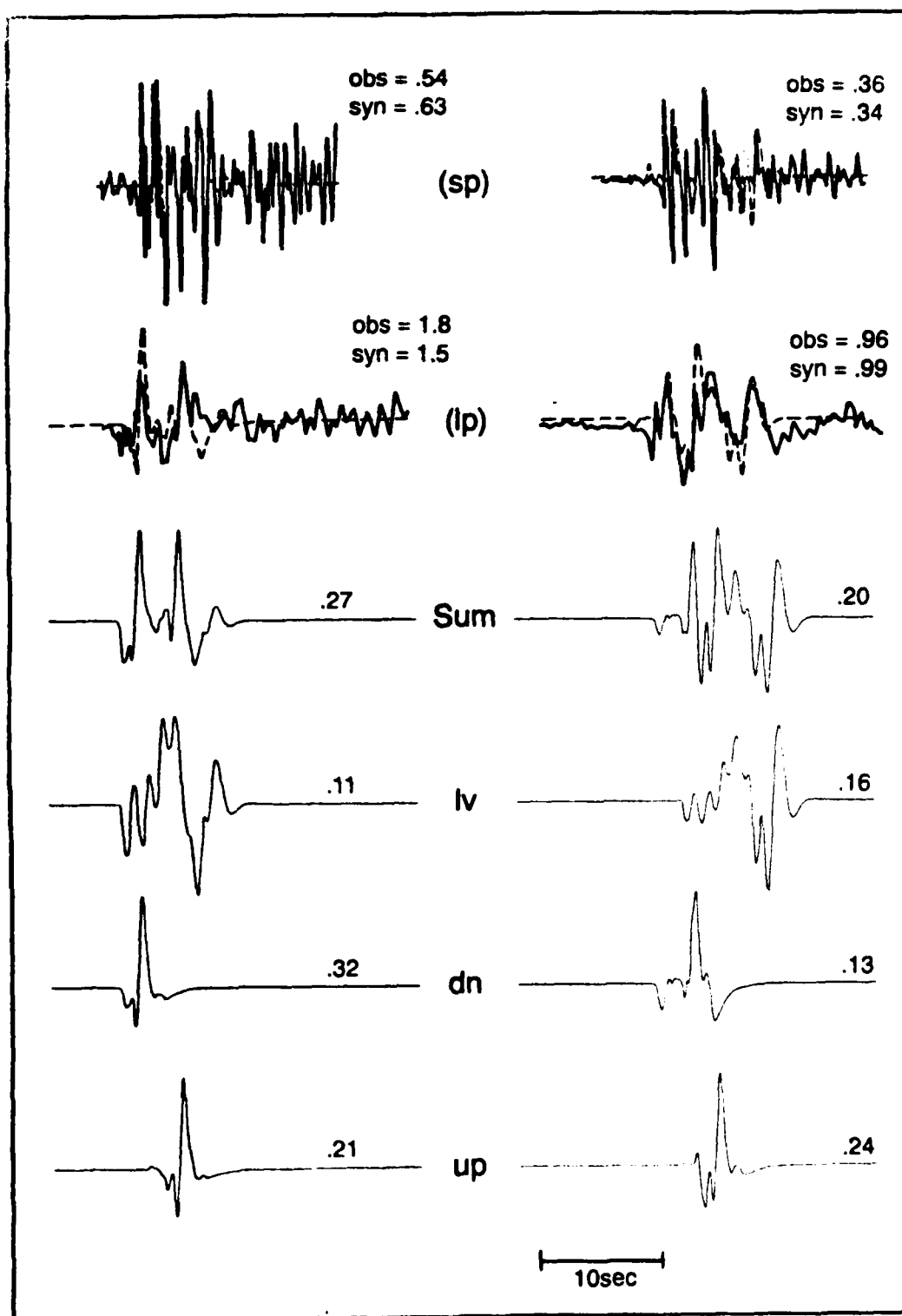


Figure 19. Comparison of observations (solid) and synthetics (dashed) for event (a) and (b), see figure 2, the lower panels display the wave-field decomposition assuming a (.2,.4,.2) trapezoidal source.

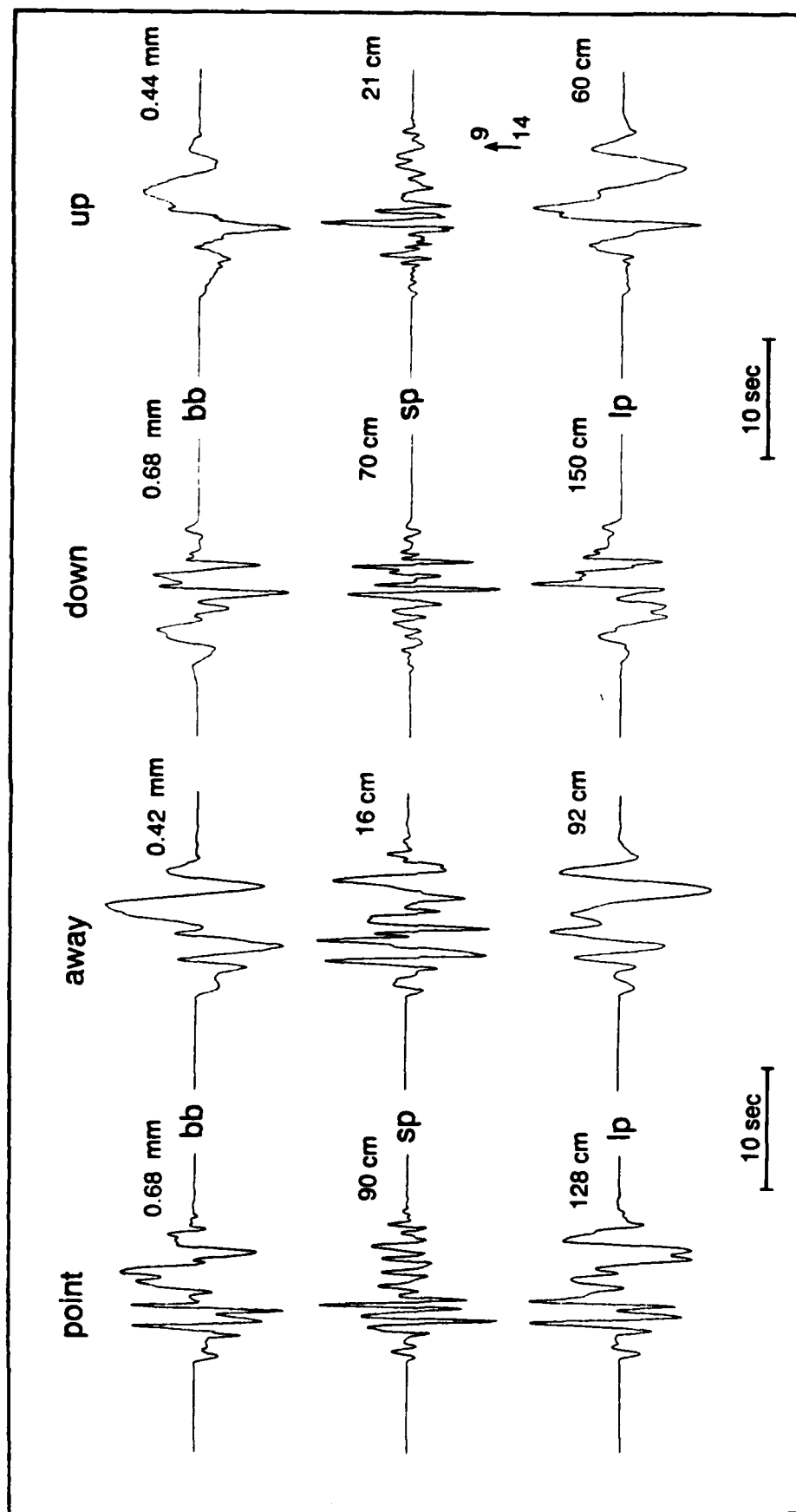


Figure 20. Directivity effects are simulated by assuming propagation along a line at six events, one km apart, rupturing at 3 km/sec. The events are all strike-slip with moments of  $1 \times 10^{23}$  ergs and have durations of (.2,.2,.2).

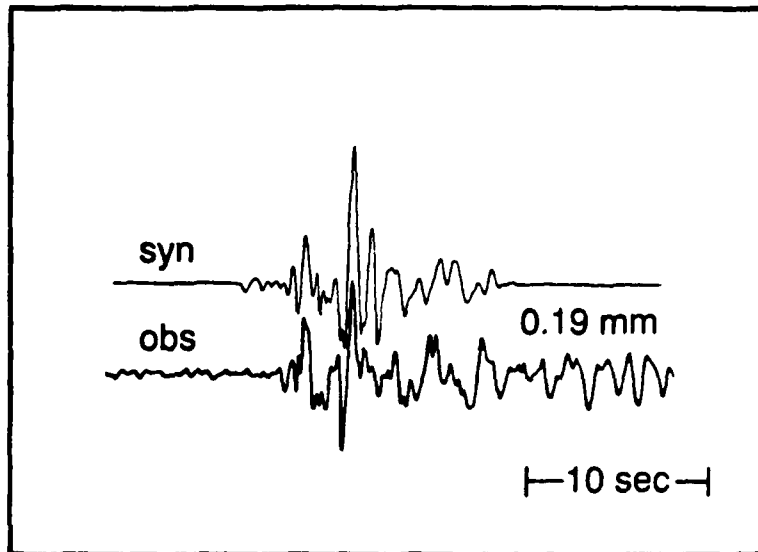


Figure 21. Comparison of the upward propagation case with the observed Coyote Mtn event. The peak amplitude of the data is .19mm corrected for instrument gain (low gain 100x), predicted to have a peak amplitude of 53 cm if recorded on the standard Wood-Anderson instrument (2800x).

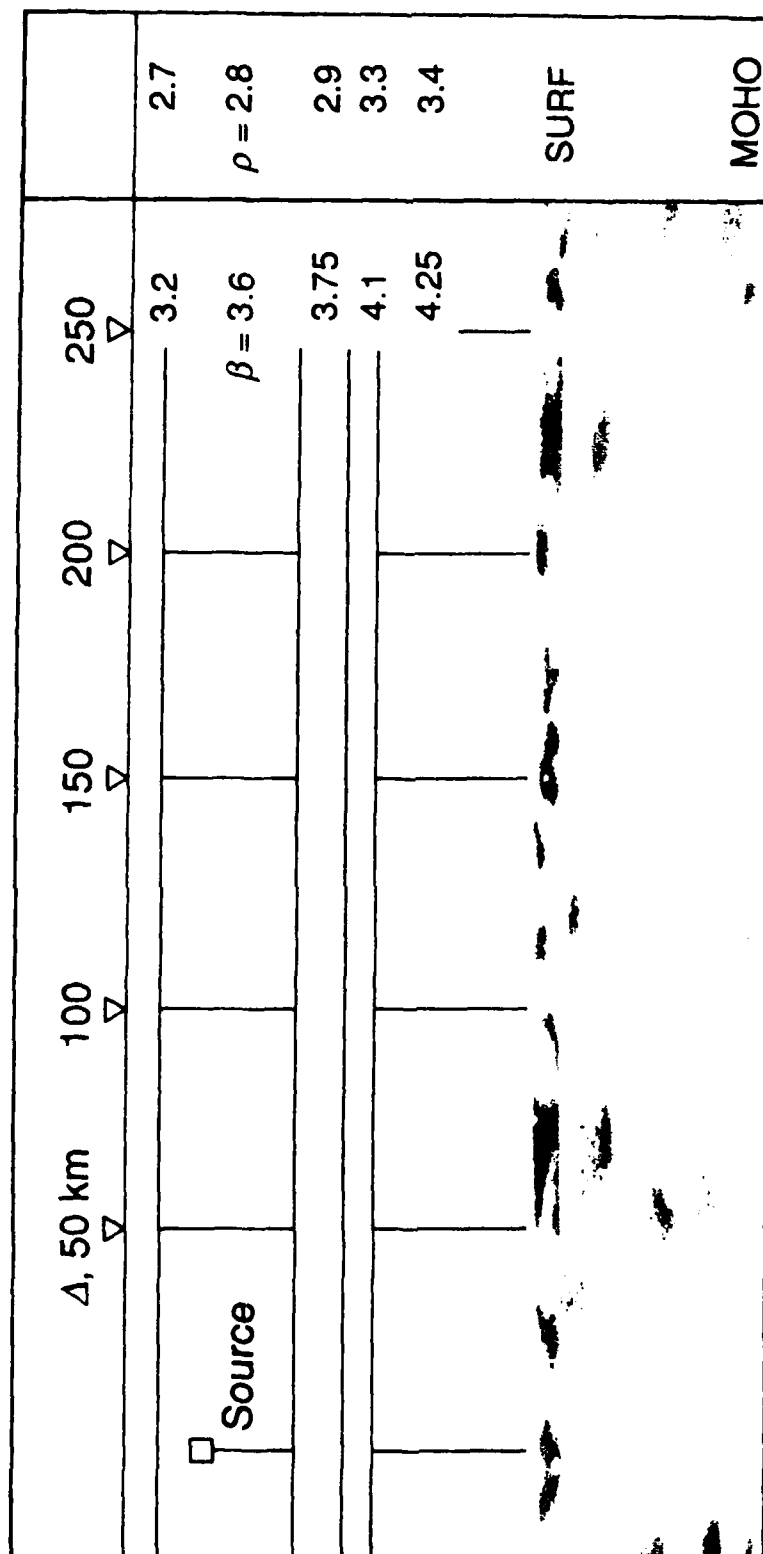


Figure 22. Diagram displaying a crustal model with various layers containing velocity anomalies (20% extremes).

# FD with Random Media Reducing $V=3.90$

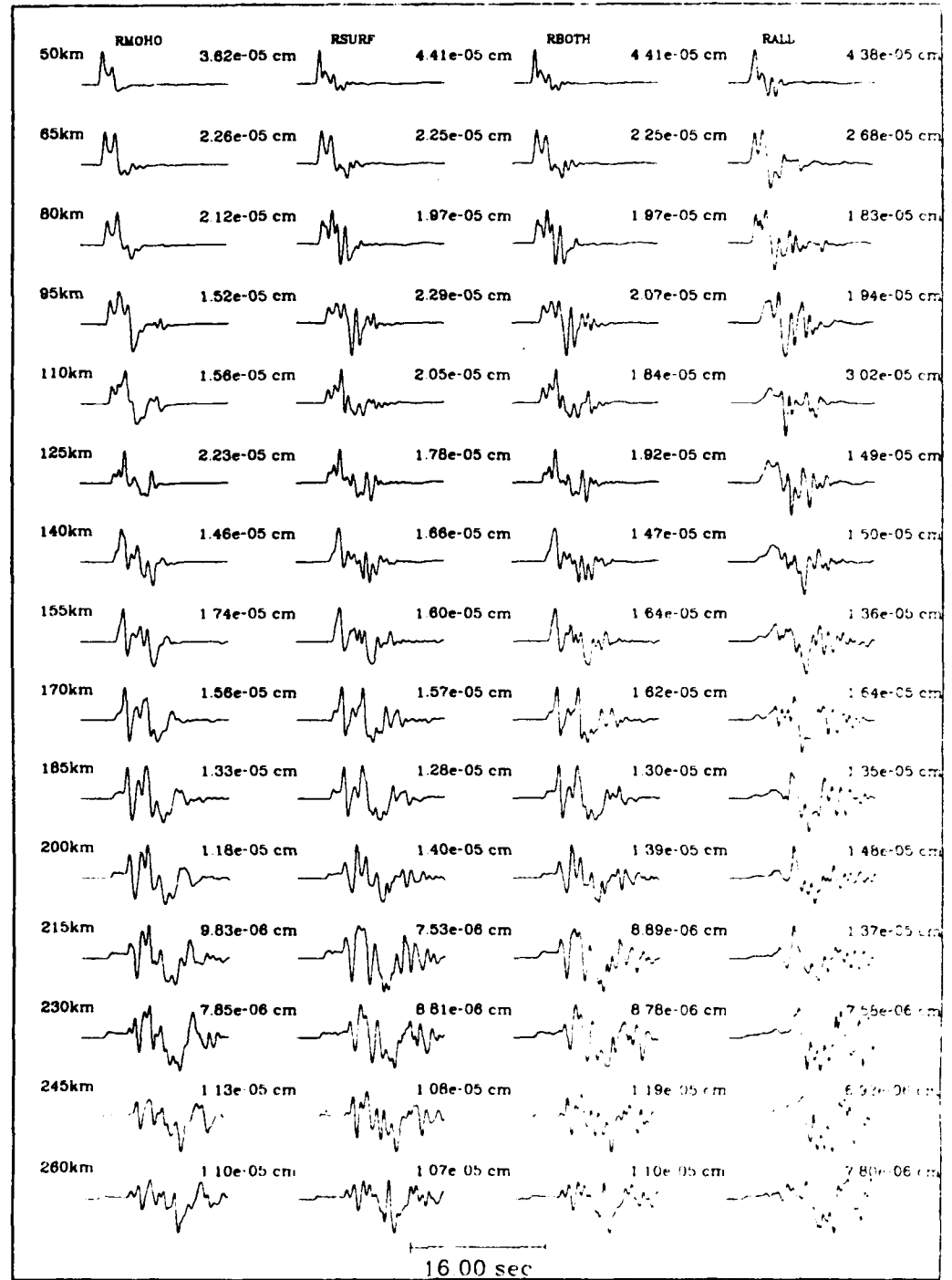


Figure 23. Profiles of BB tangential synthetics through the cross-over distances of 50 to 260 km. The column on the left (RMOHO) is nearly identical to the homogeneities case, see figure 17. The next three columns include increasingly more layered anomalies.

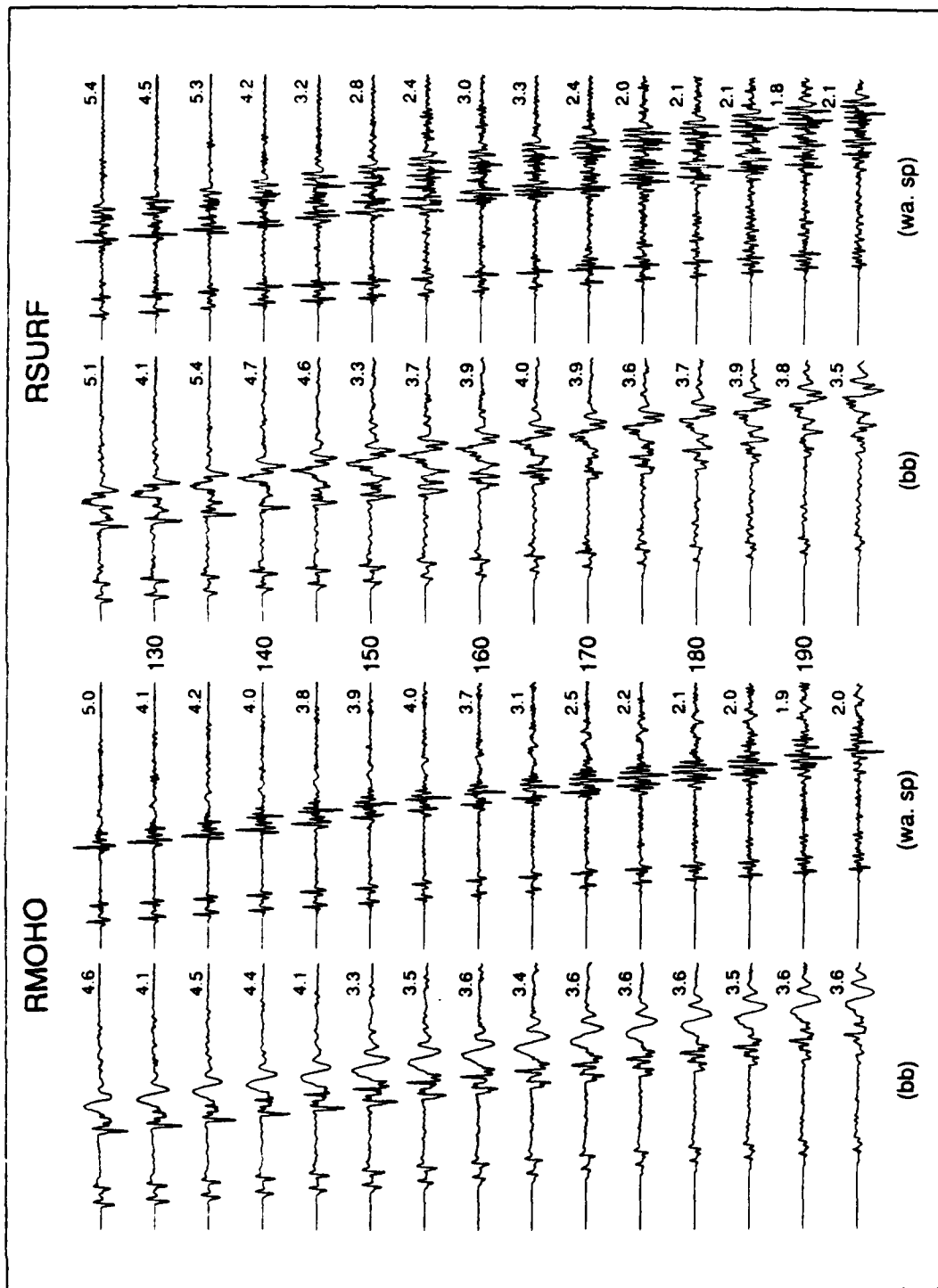


Figure 24. Comparison of BB and short period synthetics for essentially the homogeneous layered model with the model containing anomalies in the top layer. Note the increased short period duration.

# Amplitudes of Random Media Finite Difference Runs

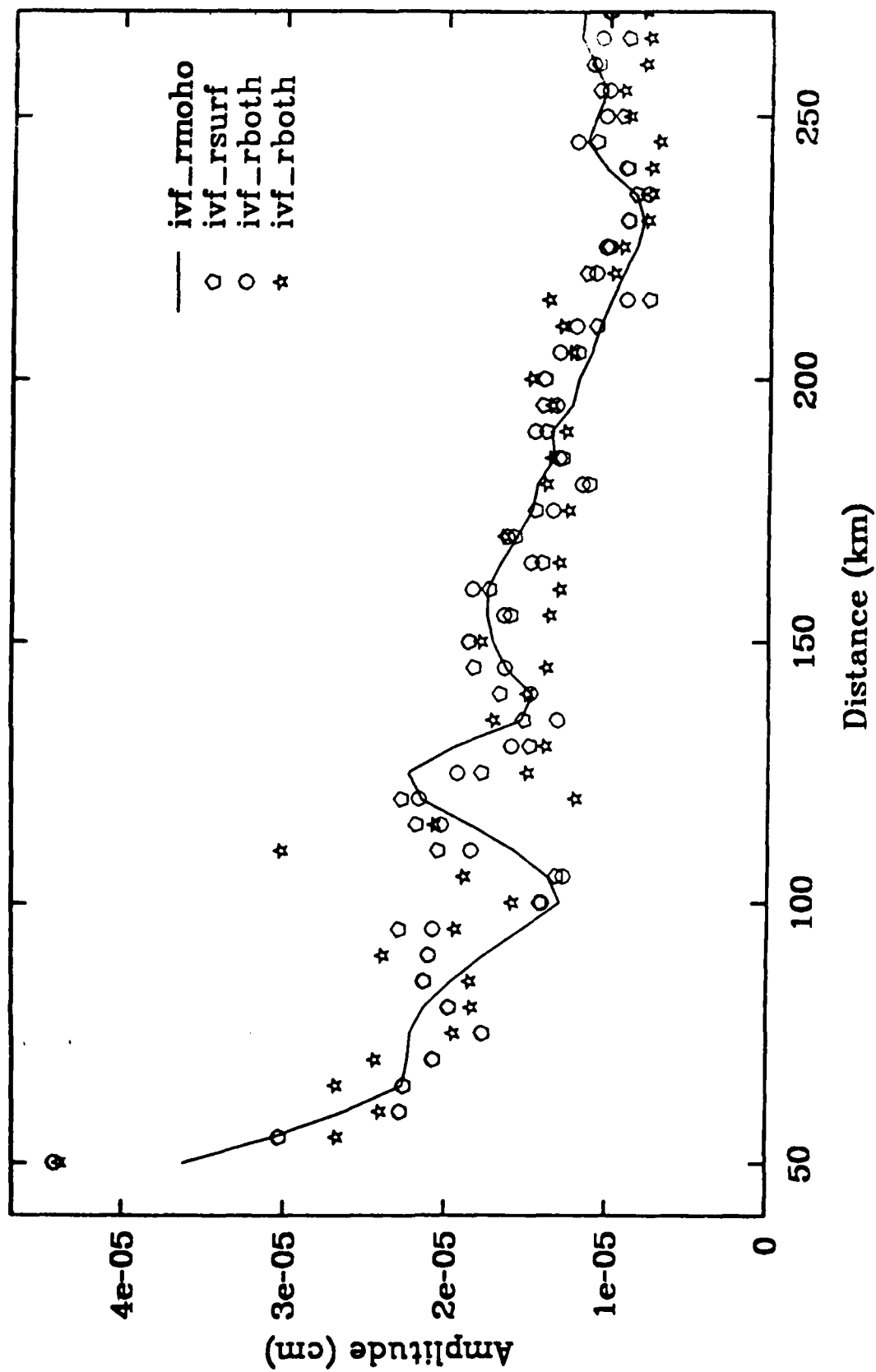


Figure 25. Comparison of the peak amplitude decay with range. The bump near 120 km is caused by critical angle Moho reflections.

## **SECTION 2**

**Determining  $M_s$  Magnitudes from Regional NTS Data**



# Determining $M_s$ Magnitudes from Regional NTS Data

Brad Woods, David Harkrider

August 2, 1991

## Abstract

We have calculated surface wave magnitudes for 102 Nevada Test Site (NTS) underground nuclear explosions from a data set of regional long-period seismograms from North American stations. In order to utilize the nearer regional stations ( $\Delta < 25^\circ$ ), a new method for determining  $M_s$  has been developed which employs synthetic seismograms to establish a relationship between the amplitude of the regional Airy phase, or Rayleigh pulse, of the data and an associated surface wave magnitude, based on conventional  $M_s$  determinations, calculated from a synthetic seismogram propagated to  $40^\circ$ . This method easily lends itself to implementing path corrections. The inclusion of path corrections decreases the  $M_s$  variance by a factor of two and also decreases the average value by 0.08 magnitude units. This latter effect is attributed to the particular station network used. The method gives stable  $M_s$  values that correlate well with other magnitude scale values over a range of three orders of magnitude in source yield. Our most refined  $M_s$  values yield the relationship  $m_b = 0.82 \times M_s + B$ , where  $B$  is dependent upon source region and shot medium. This relationship holds for events of all sizes. When events are grouped with respect to source region, significantly better fits to these individual site linear regression curves are obtained compared to the fits obtained using a single, all inclusive model. This observation implies that shot site parameters and source structure effect surface wave magnitude measurements, although event yield site distribution also may be in part responsible.

Great effort went towards making the data set comprehensive and diverse in terms of yield, source location and shot medium in order to determine the portability of seismic measuring scales. In particular we examine Pahute Mesa, Rainier Mesa and Yucca Flat explosions detonated above and below the water table.

Since our magnitude values are based on a theoretical continental structure, we regressed our values with the more standard values of Marshall *et al.* (1979). Using 14 common NTS events we found that our values were greater by  $0.53 \pm 0.03$  magnitude units.

## 1 Introduction

We re-examine the use of surface-waves for underground nuclear explosion magnitude determinations, particularly for smaller yield ( $Y < 20\text{Kt}$ ) events. The surface wave magnitude-yield scaling law for such low yield events, until now, was not known well. The data used are long-period North American station vertical records for 102 specified Nevada Test Site (NTS) events. The stations used are from several networks. Their respective instruments all have pass bands that lie within the 10 to 60 second range. Surface waves are very useful for yield estimation purposes, for ( $M_s$ ) is determined from relatively long-period seismic waves which are insensitive to high frequency near-source effects, which, along with several other possible mechanisms, may be caused by asymmetries in the shot cavity, see Zhao and Harkrider (1991). These high frequency source effects may cause appreciable bias in magnitudes that are based on higher frequency waves, such as the  $m_b$  and  $L_g$  scales.

For the lower yield events it becomes necessary to include the data from regional stations ( $\Delta < 25^\circ$ ), for teleseismic recordings have too low a signal to noise ratio, which makes them unusable. At regional distances surface waves are not well dispersed, having a prominent Airy phase pulse with a period between 6 and 20 seconds (Alewine, 1972), so that it is not possible to measure  $M_s$  conventionally (that is measuring the amplitude of the 20 sec. wave). For North America in general, there is minimum in the group velocity curve near 12 seconds for the fundamental Rayleigh-wave (Marshall *et al.* 1979).

To measure  $M_s$  we employ a technique whereby theoretical seismograms in conjunction with the surface wave data are employed to indirectly calculate

it. In using this procedure several propagation path models were tested to determine the effect of attenuation and seismic velocity structure upon the  $M_s$  values. These calculated  $M_s$  values remain stable, have reasonably small errors and correlate well with associated  $m_b$  magnitudes and log yield for the event data set. The  $M_s - m_b$  relationships are determined by a weighted least-squares linear regression.

Besides comparing the  $M_s$  results with several different independent magnitude scales, the data have also been separated with respect to source region and shot material.  $M_s$  values at Yucca Flat tend to be larger than those at Rainer Mesa by 0.09 magnitude units for a given  $m_b$ . There also appears to be some difference in waveforms between events of these two source regions. Pahute Mesa events are 0.22 magnitude units larger than those at Yucca flat for explosions set-off below the water table and with the same  $m_b$ .

We do not account for tectonic release effects upon the magnitude measurements. Such effects are best accounted for with moment tensor inversions of sources which involves more sophisticated data analysis. Standard  $M_s$  measurement techniques ignore this factor as well.

## 2 Data

The data are long-period vertical seismograms recorded at North America stations for 102 explosions at NTS and consist of digitized World Wide Seismic Network (WWSN) and Canadian Seismographic Network (CSN) records, Digital World Wide Seismic Network (DWWSN), Lawrence Livermore Regional Seismic Network (LNN) and Regional Test Seismic Network (RSTN) digital data for events occurring later than 1981. The analog WWSN and Canadian station data were digitized by ENSCO. Fifty-eight stations comprise the network, although fewer than 60 percent of the stations had data available for any single event. Fig. 1 shows a map of the station network. Epicentral distances range from 220 km for NTS to GSC (Goldstone, California), to 5200 km for NTS to STJ (Saint Johns, Newfoundland). For the smaller events, particularly Rainer Mesa explosions, only the nearer stations (distance < 1000 km) had either data available or reasonable signal to noise ratios. Station coverage varies widely between events. Five of the smaller events only had one viable station seismogram each, while some events had over 30. The average number of stations reporting per event is 10.

Surface waves that propagate across oceanic/continental margins undergo significant modification in their waveforms because of the great lateral variation in crustal and upper mantle structure at such boundaries. These propagation effects are not straight forward to model, hence appropriate Green's functions, or transfer functions, are difficult to obtain. Without robust Green's functions it is hard to infer accurate source information from the data. Smaller events also are not likely to be observed at the distant stations, which often include oceanic structure along their propagation path, and make these longer paths even less attractive to include in the monitoring network. Hence, we chose to confine our study to surface waves travelling solely along continental paths, *i.e.* within North America.

Of the 102 events, 27 are from Pahute Mesa, 16 are from Rainer Mesa, 58 from Yucca Flat and one, Piledriver, is located at Climax Stock. We consider these to be 4 distinct source regions. For some specific stations, waveforms varied somewhat between events, depending upon source location.

The Piledriver data from a given station look appreciably different from that of any other events recorded at that same station. This was true for every station recording Piledriver and probably is caused by differences in the source region for this explosion. Piledriver was detonated in a granitic source region, north of the other sites. The source to receiver geometries for this event are approximately the same as those as the other NTS events, so the difference in waveforms doesn't appear to be attributable to dispersive effects caused by differences in propagation path length. Piledriver was the only Climax Stock event with readily available data, so no further examination of this source was carried out.

At some of the nearer regional stations (distance  $< 9^\circ$ ), there are also subtle differences between the Yucca Flat and Rainer Mesa event waveforms. At DUG (Dugway, Utah), for example, the Rainer event waveforms look as if the Airy phase has been Hilbert transformed (equivalent to a  $90^\circ$  phase shift) relative to the Yucca Flat waveforms. The DUG Rainer waveforms also contain more high frequency coda energy than those from Yucca Flat. Pahute events are similar in waveform to Rainer events and have less high frequency content than Yucca events.

The seismograms were band-passed filtered between 6 and 100 seconds to get rid of the long period and short period noise which would otherwise affect the peak to peak measurement of the Rayleigh pulse. The absolute amplitudes of the data were verified by choosing several different stations

and comparing the peak to peak amplitude of the digitized record to that measured directly from the respective analog WWSSN film chip. From this step we ascertained that the station gain factor had been correctly factored out of the seismograms.

### 3 $M_s$ Calculation Technique

We have developed a method to measure surface magnitudes indirectly. Because a large portion of the data for low yield events is from stations recording at regional distances ( $\Delta < 25^\circ$ ), it is not possible to calculate  $M_s$  conventionally, for the Rayleigh-wave is pulse-like which precludes measuring a well dispersed 20 sec. phase (Alwine, 1972). We address this problem with the use of synthetic seismograms of the fundamental Rayleigh-wave using a modified Haskell-Thompson matrix method (Harkrider, 1964).

For each source to receiver path a theoretical Rayleigh-wave is generated. The Earth model used to create this synthetic is meant to reflect the average Earth structure between NTS and the given station. The Earth models used in this study were determined from inversions of dispersion and attenuation data as well as forward modeling of the waveform to fine tune the models. The criteria for determining the goodness of fit of the synthetic to the data are dispersion, absolute travel time and waveform fit (relative amplitude of different dispersed phases). Hence the synthetic seismogram displays the same spectral and time domain waveform characteristics as the data which it simulates. This was done for all paths. The paths to WWSSN and Canadian stations were taken from a study by Stevens (Stevens, 1986). The RSTN, LLN and DWWSN paths were determined previously by this research group.

To determine  $M_s$  for a particular source-receiver geometry two synthetics are generated. One which is propagated the actual path distance that is meant to simulate the data and one which is propagated to  $10^\circ$ . At  $10^\circ$  the surface wave train is well dispersed and stable, so that a conventional  $M_s$  value can be calculated. To calculate  $M_s$  we use the modified Von Seggern formula (Von Seggern, 1977):

$$M_s = \log_{10}(A/T) + 1.08 + \log_{10}(\Delta) + 1.38,$$

where  $A$  is the peak to peak amplitude (in nanometers) of the wavelet measured from the vertical record,  $T$  is the period of the wavelet, measured in

seconds, and  $\Delta$  is the propagation distance in degrees. This scale was chosen because the distance coefficient (1.08) more closely approximates the effect of attenuation along continental paths. A vertical component measurement has two advantages over horizontal component measurements. The horizontal components usually have lower signal to noise ratios than the vertical component and generally are more likely to be contaminated by Love wave signals which may be generated by tectonic release, source effects, or scattering due to lateral variations in the Earth's structure.

Both the regional and teleseismic synthetics are generated with the same source function, so that the peak to peak amplitude of the Rayleigh pulse of the regional synthetic can be directly related to the  $M_s$  value determined for a theoretical Rayleigh-wave train propagated out to  $40^\circ$ . The relationship between the data peak to peak amplitude and its indirect  $M_s$  is:

$$M_s(\text{data}) = M_s(\text{synth}|_{40^\circ}) + \log_{10}[(PPA|_{\text{data}})/(PPA|_{\text{synth}})],$$

where PPA is the peak to peak amplitude of the Rayleigh pulse. A path correction may be included on the right side of this expression.

This path correction is the difference between the individual path synthetic derived  $M_s$  and the average theoretical  $M_s$  for the entire network. For each source-receiver pair, a  $M_s$  is calculated from a synthetic seismogram propagated to  $40^\circ$ . Each such synthetic has the same size source, so ideally one would want each  $M_s$  value so measured to be equal in value. Yet this is not so, for each path's effective attenuation at the periods of interest may be different. The difference between the mean network  $M_s$  and a particular receiver  $M_s$  is the path correction. A negative path correction value implies that the theoretical  $40^\circ$  station  $M_s$  is larger than the network average. Table 1 lists the network path corrections used.

The question arises, whether or not it is valid to use the average Earth structure for a particular path to propagate a surface wave to  $40^\circ$  when the Earth model is only meant to reflect the seismic properties of the Earth for a path that may only be a small fraction of this distance. This is particularly true of the shortest paths for which the seismic waves traverse only western, North America, an area of relatively high attenuation compared to the continental craton and shield areas. A surface wave propagated  $40^\circ$  along a characteristic tectonic North American crust and mantle model (NTS to DUG, for example) for  $40^\circ$  will be much more attenuated than a wave propagated the same distance through an average structure from NTS to the

eastern seaboard (NTS to SCP, for example). Hence the calculated  $M_s$  for the NTS to DUG structure would be smaller than the NTS to SCP  $M_s$ .

There are several methods to correct for this path dependent effect. As explained above one may implement path corrections which account for the theoretical difference in attenuation between paths. Another means is to make a mixed path structure which has the appropriate path structure from the source to the actual station distance, with the rest of the path out to  $40^\circ$  being a generic seismic velocity and attenuation model. The mixed path approximation for the fundamental Rayleigh mode is easy to implement. The approximation is equivalent to assuming that the total horizontal energy flux is constant across the transmission boundary (Harkrider, 1981), (Levshin, 1985) and (Bache *et al*, 1978). Finite element results show that even for a continental-oceanic crust transtion zone this approximation is reasonable (Harkrider, 1981). For the cases in this study where the structures which comprise the mixed path are both continental structures (*i.e.* not too dissimilar) the approximation is robust enough for the synthetic seismogram calcuations.

We have implemented both procedures individually and in conjunction to see what their effects are. Another method would be to include empirical station corrections (Yacoub, 1983), (Given and Mellman, 1986). The findings concerning the path corrections are discussed in the results section.

## 4 Data Analysis and Results

The seismograms were band-passed filtered between 6 and 100 seconds to minimize contaminating noise as described previously. The vertical records were visually inspected to insure that they were within the correct time window and that their signal to noise ratio was above 2.0.  $M_L$  values were then calculated for the data as per the method described above (equation 10) with several variations. The synthetic seismograms were also band-passed filtered between 6 and 100 seconds for consistency. The  $M_s$  are plotted against seismic magnitudes of several scales for the same set of events. It should be noted that complete magnitude lists were not available for all 102 events.

We chose to compare or plot our data primarily with body wave magnitudes determined by Lilwall and McNeary (1985). The Lilwall data set contains 75 seven of the 102 events examined by us and is believed to be

a well determined and self-consistent list of  $m_b$  values that have small errors due to, among other things, the inclusion of network station corrections. Fig. 2 shows the  $m_b$ -yield relationship for events in this study for which  $m_b$  and yield information were available. It is important to notice that events above and below the water table separate into two distinct populations. For this data set this separation is only apparent near the cluster of events with  $m_b$ 's around 5.1. Also notice the very small error bars for this data; for many events the error bars are smaller than the symbols demarking a data point. The correlation between  $m_b$  and yield is good, with the scatter mostly being due to the above water table shots.

Several sets of synthetic Rayleigh-waves were calculated at the  $40^\circ$  distance. One set was propagated along the single structure model (hereafter referred to as the single path case) which reflects the average Earth structure between NTS and a given station. Two sets of mixed path synthetic seismograms were also generated. For that part of the path beyond the actual source receiver distance, out to  $40^\circ$ , a generic earth structure was used. The NTS-RSSD Earth structure was chosen for this generic path section, as it is a relatively simple structure which generates stable surface waves and it is roughly an intermediate range station (distance  $< 1290$  km), so that its structure can be considered to be an "average" structure for the network. The difference between these two mixed path earth structures is in their spectral attenuation coefficients, with  $\gamma_\beta$  being twice as large, at a given frequency, for the mixed path 2 case as for the mixed path 1 case.

Surface magnitudes were first calculated from the  $40^\circ$  synthetics generated with a single structure propagation path. Fig. 3 displays single path  $M_s$  values, calculated as described above, versus body-wave magnitude ( $m_b$ ). These  $m_b$ 's are those Lilwall and McNeary (1985). In the left fig. the  $M_s$ 's are calculated without path corrections, whereas path corrections are included in the figure on the right. The solid line is the best fitting weighted least-squares regression of the data, with the weighting factor being inversely proportional to individual event standard deviations. The dashed lines represent the two standard deviation error of the fit of the line to the data. Solid black circles are shots below the water table, shots above the water table are open circles, and open squares are shots for which this information is not known. Note the error bars are approximately 50 percent larger for the uncorrected  $M_s$ 's (Fig. 3a) than for the case of path-corrected  $M_s$ 's (Fig. 3b). The scatter in the data is also slightly less for the path corrected  $M_s$ 's. It appears that the



path corrections do improve  $M_s$  measurements.

The most significant effect of including path corrections is the reduction in variance of individual magnitudes. Without path corrections the individual station magnitudes have a bi-modal distribution reflecting the two generic Earth models of North America: the tectonic western and cratonic eastern crust and upper mantle structures. The path corrections bring-in the outlying station magnitudes values towards the mean value. Table 1 lists these network path corrections. The first column lists the corrections for single path synthetics. A positive value denotes that the  $M_s$  for a station is smaller than the network theoretical average. The fourth column is the number of events that were recorded at the station for the data entire set.

We next explored the effect of mixed path transfer functions upon the  $M_s$  calculations. As described above, we chose the path to RSSD as a generic structure for the second portion of the mixed path synthetic seismogram calculations. We generated two sets of these synthetics. The attenuation of the generic path was doubled for one of these sets (RSSDx2). Fig. 4 shows the attenuation factors ( $\gamma$ ) as a function of period. The line labeled RSSDx2 is that of the increased attenuation structure. It is referred to as "mixed path 2" throughout this study. The lower, dashed curve is the attenuation curve for the RSSD structure. Synthetics made with this RSSD generic structure for the latter portion of the 40° travel path will be referred to as "mixed path 1". Table 1 gives the path corrections for each station for these two cases, also.

Fig. 5 is analogous to Fig. 3, the difference being that the  $M_s$  magnitudes were calculated using synthetic seismograms using the mixed path 1 model. In Fig. 5a the  $M_s$ 's are calculated without path correction terms, while in Fig. 5b path corrections are included. As before the addition of the path correction terms cut the variance by about a factor of 2. Also the average  $M_s$  value decreased by a 0.01 units from those without path corrections. This difference may be statistically significant, for the standard error of the mean of the regression line is only 0.026. What is most striking between Fig. 3 and 5 is that slope of the regression line are the same for the two mixed path 1 cases, with

$$m_b = 0.83 \times M_s + B.$$

For the single path case, path corrected  $M_s$  values give the same relationship, but the slope is appreciably larger ( 0.9 ) for the uncorrected magnitudes.

although the difference lies within the errors bounds. It would seem that both path corrections and mixed path Green's functions improve  $M_s$  determinations for the method used here.

Thus the inclusion of path corrections in calculating  $M_s$  lowers the magnitude value by 0.04 units on average. This can be explained by the network coverage and the range of synthetic  $M_s$  values. The distribution of  $M_s$  values is skewed, with there being a significant number of stations with theoretical  $M_s$  values significantly larger than most of the stations within the network. Events for which such stations reported would yield a larger average  $M_s$  than for events that did not.

Fig. 6a and 6b are  $M_s$  vs.  $m_b$  plots for the mixed path 2 case without and with path corrections, respectively. For 6a a fixed slope regression, was used, so that more a more apt comparison could be made to its mixed path 1 counterpart plot. Comparing Fig. 5a to Fig. 6a shows that the average  $M_s$  value dropped 0.02 magnitude units for the mixed path 2 case relative to the mixed path 1 case. This follows from the fact that the attenuation for the second portion of the path is twice as large for the mixed path 2 case as that for the mixed path 1 case.

In comparing Figs 5b and 6b, however, it is apparent that there are no differences in magnitude values and the regression line intercept and slopes have the same value in both cases, even though the mixed-path Green's functions used for  $M_s$  calculation purposes differed with respect to attenuation for the two cases. The effect of the path correction, besides reducing the data variance as described above, is to negate the effect of differences in attenuation between the two models. To obtain stable, robust  $M_s$  values with this method it is best then to use mixed path generated synthetics in conjunction with path corrections for the 40°  $M_s$  measurements. The variance among the mixed path based  $M_s$  values for the network is smaller than that when  $M_s$  is derived from single path synthetics, so that magnitude measurements will be more consistent when they are determined from mixed path synthetics. This is particularly important for events with few reporting stations. All further plots of  $M_s$  in this study use values obtained from the mixed path 1 case with path corrections, unless stated otherwise.

How well the final  $M_s$  values reflect the actual seismic magnitude of these events necessitates having another measure of their size. In the event of anomalously high or low seismic source coupling, for example, both body waves and surface waves should be affected similarly by the coupling effect.

A magnitude parameter independent of seismic observations would be useful to plot the  $M_s$  against, so we have also fitted our results to estimated log yields. Fig. 7 shows the relationship. Yield values are estimated to be within 10 percent of the actual yield (Springer and Kinnaman, 1971). Yield information was available for 97 of the events, thus yields make-up the most comprehensive data set to compare our results to as well. The yields for this data set range over three orders of magnitude in size. The greatest scatter, as in the case of  $M_b$  vs. log yield, is due to shots above the water table. It should also be kept in mind that the scatter would be further reduced if the data were separated into populations based on their location at NTS. (i.e. Pahute Mesa, Rainier Mesa and Yucca Flat). Because of the classified nature of some the yields, it is not possible, here, to closely examine these effects with respect to yield.

Since our magnitude values are based on theoretical continental structures, as well as the particular network used, we wanted to compare our  $M_s$  values to those obtained from standard  $M_s$  methods. One such standard data set is that of Marshall *et al* (1979). There is an overlap of 14 events between studies. We performed a fixed-slope (slope=1.0), regression of our  $M_s$  values to theirs. Fig. 8 shows that the correlation is very good; scatter is small for events above and below the water table. It's important to note that with our method we are able to measure  $M_s$  for events 0.75 units smaller than the smallest Marshall values. We are able to measure  $M_s$  for these smaller events, because we are able to make use of near-regional (< 500 km) records with the method described in this paper. The offset in  $M_s$  between scales is 0.53 with mean standard error of 0.03 magnitude units. This offset is due in part to the difference in definition of  $M_s$ . At  $40^\circ$  the offset in magnitude is 0.15, thus reducing the offset to 0.38 units. However, for the method described in this study,  $M_s$  is based upon a theoretical network average  $M_s$ , so it will have a bias attached to it which is dependent upon the network used. This network bias can be assumed to be responsible for part of the offset, as well.

Table 2 lists the final mixed-path, path-corrected  $M_s$  values for the 102 events of this study. The first column lists the number of stations recording the event. Next are given the surface wave magnitude and associated error for the event are given. Next is a three letter shot information code. The first letter denotes its geographic location: Yucca (Y), Pahute (P), Rainier (R), or Climax Stock (C). The second is whether its shot depth was above (A) or below (B) the water table. The last letter describes the shot site rock

as tuff (T), rhyolite (R), granite (G), or alluvium (A). An underscore means that the information is not known. The final two columns are the event's name and Julian data, respectively. The events are listed in chronological order.

To determine the portability of this  $M_s$  calculation method the events need to be separated into groups based on their source regions and then compared, one group to another, in order to see if there are systematic differences in  $M_s$  values relative to any other magnitude scale. Three main geographic source regions comprise the event data set: Pahute Mesa, Rainier Mesa and Yucca Flat.

Whether or not a shot occurs within saturated material is another criterion by which to separate events in order to look for systematic differences in  $M_s$  values. Other studies have found significant seismic coupling differences between explosions detonated above and below the water table (Gupta, 1989), so it is a reasonable parameter to study. Reviewing Figs. 2 and 7, it is also apparent that for shots fired-off below the water table have a larger seismic magnitude than those detonated above the water table.

Fig. 9a shows the relationship between  $M_s$  vs. Lilwall  $m_b$  for all NTS events. The surface-wave magnitudes were all calculated using mixed-path Green's functions and path corrections. Figs. 9b and 9c divide the data populations into above and below the water table, respectively; shots for which water table information was not available were left out. There is no appreciable difference between the above water table and below water table curves. This is not surprising; referring to Figs. 2 and 7 it is apparent that both seismic magnitude-yield curves show that for a given yield an event below the water table has a larger magnitude than a shot above the water table. It follows that the  $M_s - m_b$  relationship may not show the same discrepancy between shots detonated above and below the water table, for the effect of the water content in the shot medium should affect surface waves and body waves in the same manner. All three regression curves are essentially the same within the error bounds. There is considerable scatter in all three figures, but that is not surprising considering the diversity of the sampled populations. Even with this scatter, the best-fitting  $M_s - m_b$  line is well constrained, for the population covers a wide range of magnitudes.

Fig. 10a gives the  $M_s - m_b$  relationship for all Yucca events. The regression curve is significantly different from that of Fig. 9a. The scatter in the data is reduced by 25 percent over that of the general population. Separating

the events with respect their relation to the water table yields two distinct curves, unlike the case where shots from all sites are grouped together. For the Yucca events below the water table (Fig. 10b) the regression curve fit is, within the errors, is not greatly different from the case of all NTS events below the water table (Fig. 9b). In Fig. 9c, for shots in dry medium, the  $M_s$ - $m_b$  curve is significantly different from the NTS above water table curve (Fig. 9c). The significance of this curve is questionable, however, due to the paucity of data used to establish it.

Fig. 11a plots all Pahute event  $M_s$ 's vs. their respective  $m_b$ 's. The relationship is essentially the same as for the aggregate NTS plot (Fig. 9a). Fig. 11b shows the relationship for Pahute shots below the water table. The slope of this curve is nearly the same as that for Yucca below water table shots, although the intercept differs appreciably. This result implies that for a given  $m_b$ , surface wave magnitudes for events at Pahute Mesa are larger than those at Yucca Flat. Fig. 11c shows the  $M_s$ - $m_b$  relationship for Pahute events above the water table. Because events in this category are clustered around  $m_b = 5.5$ , a well constrained line cannot be obtained, so we applied a fixed-slope regression, using a slope of 0.82 (that of the below water table case). Comparing Fig.s 11b and 11c, an off-set in  $M_s$ - $m_b$  of 0.09 with a mean standard error of 0.04 is obtained, implying some degree of difference in seismic coupling between body and surface waves.

Fig. 12a displays the  $M_s$ - $m_b$  regression curve and data for Rainier Mesa events, all of which are above the water table. Although the clustering of data near  $m_b = 5.0$  causes the curve to be poorly constrained, a slope close to that for Pahute events and Yucca (below the water table) is obtained. Constraining the slope to be 0.82, as in the case of Pahute events yields Fig. 12b. Comparison of the equations of Fig.s 12b and 11b give an off-set of 0.31, with a mean standard error of 0.04,  $m_b$  units, so that for a given  $m_b$ , shots at Pahute produce larger  $M_s$  values than at Rainier Mesa. Either the Pahute site is more efficient at producing surface waves or the Rainier site is less efficient at coupling body-wave energy. Rainier events are tunnel shots. The immediate source region ( $R < 200$  m) may behave like an asymmetric cavity, resulting in a source that is non-isotropic (Zhao and Harkrider, 1991) and/or seismic coupling that has strong frequency dependence.

## 5 Conclusion

The method described herein to calculate surface wave magnitudes allows the measuring of  $M_s$  for nuclear explosions over a wide magnitude distribution. Using this technique, it is now possible to use near regional ( $\Delta < 15^\circ$ ), long-period records in conjunction with the far-regional ( $\Delta > 15^\circ$ ) and teleseismic records, that have previously been used to make conventional  $M_s$  measurements, in order to measure surface wave magnitudes. This increase in observations has two advantages. First, for any event the station network coverage is enhanced in terms of overall numbers as well as in azimuthal coverage, in particular stations only several hundred miles away from NTS in California, Nevada and Utah can be included in a network that otherwise would have no coverage to the west or southwest. These improvements make the network  $M_s$ 's more stable and statistically robust. Secondly, smaller events with surface waves that haven't been analyzed will now have such observations available, so that their surface wave magnitudes now can be calculated. The method produces stable  $M_s$  values that are consistent with other seismic magnitude scales. Thirdly, the effect of inaccuracies in estimating  $Q$  are negligible for very near-regional recordings ( $< 500$  km). With the  $M_s$  calculation technique used here, one can take advantage of such nearby recordings. Lastly this method makes it very easy to use historical analog data sets more easily, for it is not necessary to use digitized data if only the maximum peak to peak amplitude needed to calculate  $M_s$ 's in this fashion.

In order to do a thorough investigation of source effects discussed above, a more complete data set of events with different pertinent source parameters is needed for observation. Specifically, events chosen for any one site location should cover a wide range of yields or magnitudes and comprise events detonated both above and below the water table. Obviously, at some site locations, it may not be possible to come up with such a comprehensive, ideal data set. This is particularly true of Rainier Mesa where most all events have yields less than 20Kt. From the results obtained with the data set used here, there does appear to be significant differences in seismic coupling between NTS sub-sites, with events at Pahute Mesa producing larger surface-wave magnitudes for a given  $m_b$  than at Rainier Mesa or Yucca Flat. This discrepancy is largest for Rainier Mesa events.

As stated earlier the method used here to obtain  $M_s$  values lends itself to such a diverse data set, for the measurement of the smallest events is

facilitated with near-regional observations.

## REFERENCES

- (1) Alewine, R.W. Theoretical and Observed Distance Corrections for Rayleigh-Wave Magnitude. *Bull. Seism. Soc. Am.*, 62(6):6133-6142, 1972
- (2) W.L. Rodi Bache, T.C. and D.G. Harkrider. Crustal structures inferred from rayleigh-wave signatures of nts explosions. *Bull. Seism. Soc. Am.*, 68(5):1399-1413, 1978.
- (3) W.W. Chan, Gupta, I.N., C.S. Lynnes and R.A. Wagner. A comparison of the spectral characteristics of nuclear explosions detonated below and above the water table. Technical Report GL-TR-89-0151. ARPA Order No. 5307. ADA214595.
- (4) Harkrider, D.G. Surface waves in multilayered media i. rayleigh and love waves from buried sources in a multilayered elastic half-space. *Bull. Seism. Soc. Am.*, 54:627-679, 1964.
- (5) Harkrider, D.G. Coupling near source phenomena into surface wave generation. In Husebye and Mykkeltveit, editors, *Identification of Seismic Sources - Earthquake or Underground Explosion*, pages 277-326. D. Reidel, 1981.
- (6) Levshin, A.L. Effects of lateral inhomogeneities on surface wave amplitude measurements. *Annales Geophysicae*, 3(4):511-518, 1985.
- (7) Lilwall, R.C. and J.M. Neary. Redetermination of earthquake body-wave magnitudes using isc bulletin data. Technical Report, AWRE, 1985. No. O 21/85
- (8) D.L. Springer Marshall, P.D. and H.C. Rodean. Magnitude corrections for attenuation in the upper mantle. *Geophys. J.R. astr. Soc.*, 57:609-638, 1979.
- (9) Springer, D.L. and R.L. Kinnaman. Seismic source summary for U.S. underground nuclear explosions, 1961-1970. *Bull. Seism. Soc. Am.*, 61(4):1073-1098, 1971.



- (10) Stevens, J.L. Estimation of scalar moments from explosion-generated surface waves. *Bull. Seism. Soc. Am.*, 76(1):123-151, 1986.
- (11) Von Seggern, D. Amplitude distance relation for 20-second rayleigh waves. *Bull. Seism. Soc. Am.*, 67(2):405-511, 1977.
- (12) Yacoub, N.K. Instantaneous amplitudes: A new method to measure seismic magnitude. *Bull. Seism. Soc. Am.*, 73(5):1345-1355, 1983.
- (13) Zhao, L.S. and D.G. Harkrider. Wave Fields From an Off-Center Explosion in an Embedded Solid Sphere. Submitted to *Geophysical Journal International*.

Table 1: Network Path Corrections

Path Correction Single Path	Path Correction Mixed Path 1	Path Correction Mixed Path 2	Station Name
0.12	-0.21	-0.20	AAM
0.13	0.20	0.20	ALQ
0.52	0.49	0.49	BKS
0.19	-0.40	-0.40	BLA
-0.36	-0.12	-0.20	BLC
0.29	-0.02	-0.02	BOZ
-0.47	-0.30	-0.29	CMC
-0.17	0.03	0.03	COR
0.08	-0.39	-0.40	DAL
-0.08	-0.07	-0.07	DUG
0.29	-0.10	0.06	EDM
-0.04	-0.19	-0.19	EPT
-0.27	0.02	0.02	FCC
-0.27	-0.06	-0.07	FFC
0.19	-0.26	-0.26	FLO
-0.36	-0.31	0.20	FRB
0.40	0.42	0.41	FSJ
0.19	-0.25	-0.26	FVM
0.19	-0.24	-0.23	GEO
-0.15	0.01	0.01	GOL
0.24	-0.09	-0.09	GSC
-0.44	-0.19	-0.19	INK
0.09	0.16	0.16	JCT
-0.18	-0.06	-0.06	LHC
-0.12	-0.07	-0.06	LON
0.33	-0.21	-0.01	LUB
-0.47	-0.42	-0.44	MBC
0.12	0.31	0.30	MNT
0.29	-0.04	-0.03	MSO
-0.28	0.10	0.16	OGD
0.12	0.34	0.34	OTT
-0.10	-0.01	-0.01	OXF
0.40	0.43	0.43	PHC
0.29	0.15	0.15	RCD
0.15	0.20	0.20	RES
0.12	0.30	0.30	SCH
-0.42	-0.35	-0.35	SCP
0.29	0.14	-0.08	SES
-0.02	-0.02	-0.02	SHA
0.12	0.17	0.17	STJ
-0.04	-0.23	-0.23	TUC
0.40	0.45	0.45	VIC
0.14	0.22	0.19	WES
-0.44	-0.04	-0.34	YKC
0.13	0.20	0.20	ALQD
0.27	0.35	0.34	JASD
-0.12	-0.07	-0.07	LOND
-0.42	-0.35	-0.35	SCPD
-0.07	0.01	0.01	RSCP
-0.14	-0.09	-0.09	RSSD
-0.25	-0.24	-0.23	RSON
0.01	0.16	0.20	RSNY
-0.44	-0.04	-0.34	RSNT
0.12	0.35	0.34	GAC

No. Seq.	Ms	Ms s.d.	Shot Info.	Event	Julian Date
11	3.98	0.16	YBT	wagtail	65062
4	3.83	0.18	YBT	lampblack	66018
6	4.03	0.16	PBT	rex	66055
14	4.32	0.16	YBT	piranha	66133
29	4.30	0.20	CBG	piledriver	66153
19	4.26	0.14	YBT	tan	66154
3	3.41	0.05	R_T	midimist	67177
1	3.17	-	RAT	doormist	67243
8	3.64	0.13	YBT	cobbler	67312
5	3.49	0.07	R_T	dorsalfin	68060
8	3.45	0.16	RAT	hudsonseal	68268
10	3.98	0.16	R_T	wineskin	69015
1	3.16	-	R_T	cypress	69043
16	4.00	0.14	YBT	blenton	69120
1	3.28	-	R_T	dianamist	70042
13	4.34	0.15	YBT	shaper	70082
3	3.39	0.04	RAT	mintleaf	70125
2	3.10	0.06	R_T	hudsonmoon	70146
7	3.20	0.18	R_T	camphor	71180
15	4.08	0.14	YBT	miniata	71189
21	3.68	0.19	YBT	algodones	71230
6	3.46	0.21	RAT	mistynorth	72123
3	3.30	0.07	YBT	monero	72140
6	3.33	0.05	R_T	diamondsculls	72202
9	4.05	0.16	YBT	miera	73067
14	4.04	0.16	YBT	starwort	73116
6	3.40	0.07	RAT	didoqueen	73156
14	4.35	0.16	YBT	latir	74058
6	3.49	0.14	R_T	mingblade	74170
22	4.57	0.17	YBT	escabosa	74191
13	3.90	0.18	YBT	stanyan	74269
15	3.98	0.17	YBA	cabrillo	75066
1	3.45	-	RAT	diningcar	75095
12	3.73	0.16	YBT	obar	75120
24	4.53	0.20	YBT	mizzen	75154
1	3.34	-	R_T	huskypup	75297
15	4.44	0.19	YBT	keelson	76035
1	3.35	-	RAT	mightyepic	76133
7	4.22	0.15	YBT	rudder	76363
17	4.14	0.14	YBT	bulkhead	77117
9	4.07	0.16	YBT	crewline	77145
27	4.31	0.19	YBT	lowball	78193
11	3.87	0.20	YBT	quargel	78322
18	4.34	0.17	YBT	quinella	79039
20	4.18	0.19	YBT	pyramid	80107
4	3.51	0.10	R_T	minersiron	80305
8	4.33	0.14	YAT	baseball	81015
6	4.12	0.19	YBT	rousanne	81316
9	4.53	0.12	PBR	molbo	82043
9	4.27	0.17	YBT	bouschet	82127
6	3.38	0.16	RAT	diamondace	82266
14	4.11	0.25	YBT	torquoise	83104
9	3.41	0.19	RAT	midasmyth	84046
16	4.35	0.19	YBT	mundo	84122
8	4.49	0.12	PBT	towanda	85122

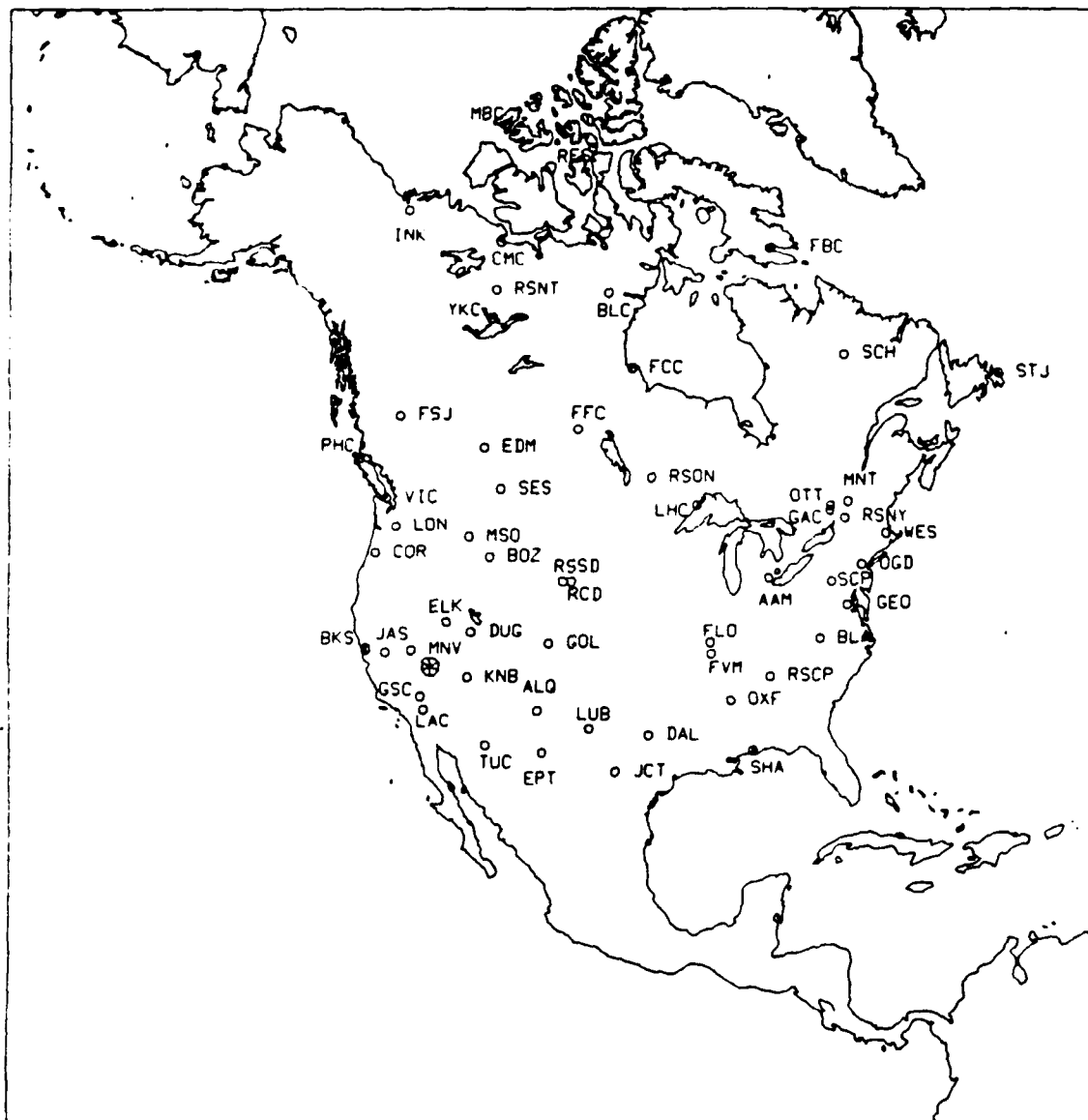


**Figure 1..** Map of North American station network used in this study. The "spoked wheel" is the Nevada Test Site.

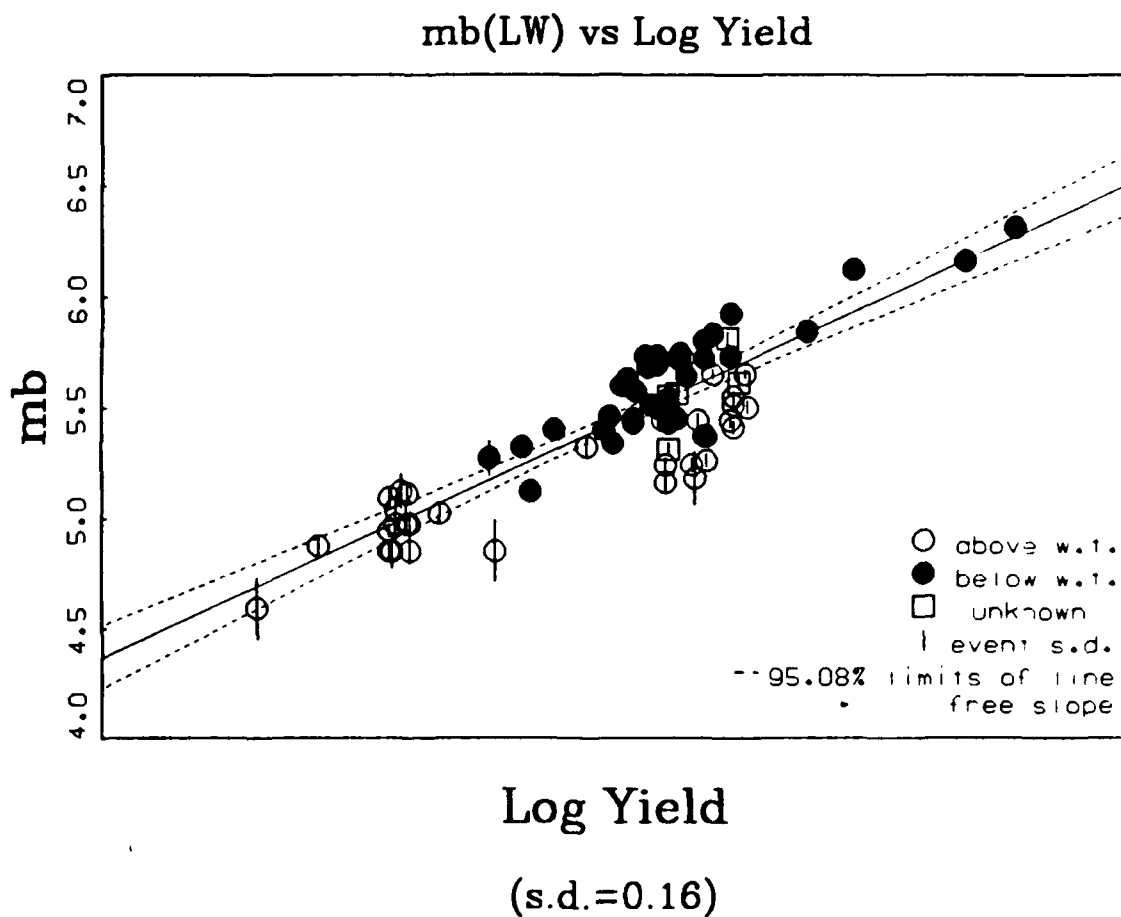


**Figure 2.** Lilwall- $m_b$  vs. log-Yield for events from this study. The solid line is the best-fitting regression line. The dashed lines show the 95 percent confidence interval of this line. Lines through the data points represent one standard deviation in a datum measurement. Blackened circles represent sources beneath the water table, open circles are events above the water table and open squares are events for which this information is not known. Events detonated below the water table have a larger  $m_b$  for a given yield. Besides this separation of data, there is little scatter to the data. The consistency of the  $m_b$ -yield relationship makes it reasonable to use these  $m_b$  values to plot our  $M_s$  measurements against.

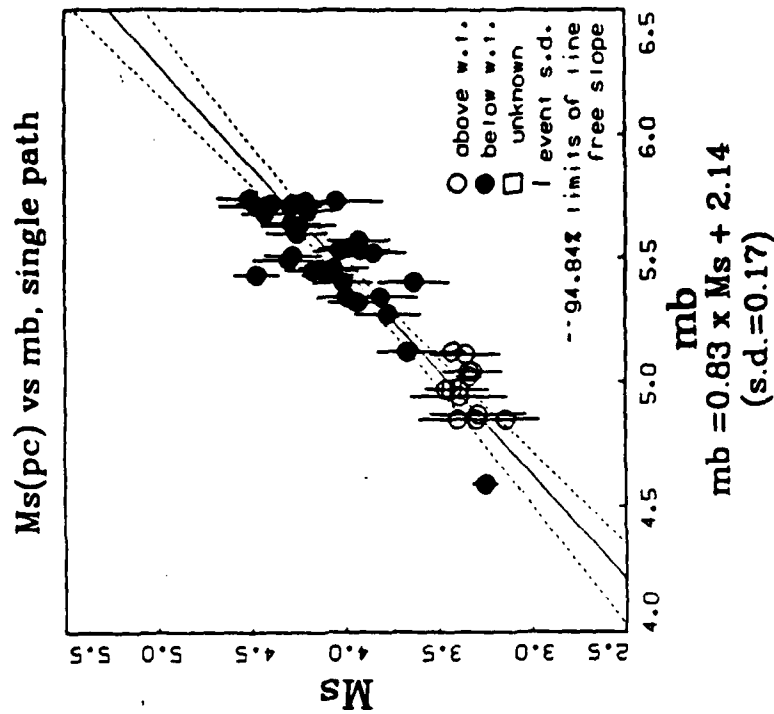
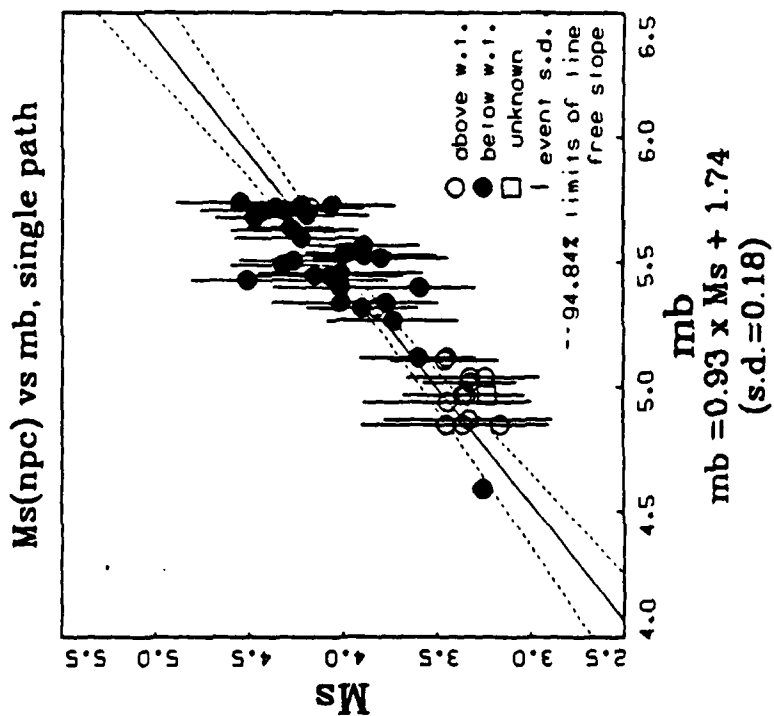


**Figure 3.**  $M_s$  vs. Lilwall  $m_b$  for a subset of the data set studied.  $M_s$  is calculated with single path Green's functions, and (a) without path corrections and (b) with path corrections. The best-fitting regression model is the solid line running through the data points. The dashed lines are the 95 percent confidence intervals of the line. The  $M_s$ - $m_b$  relationship and the r.m.s. error of the data are at the bottom of each figure.

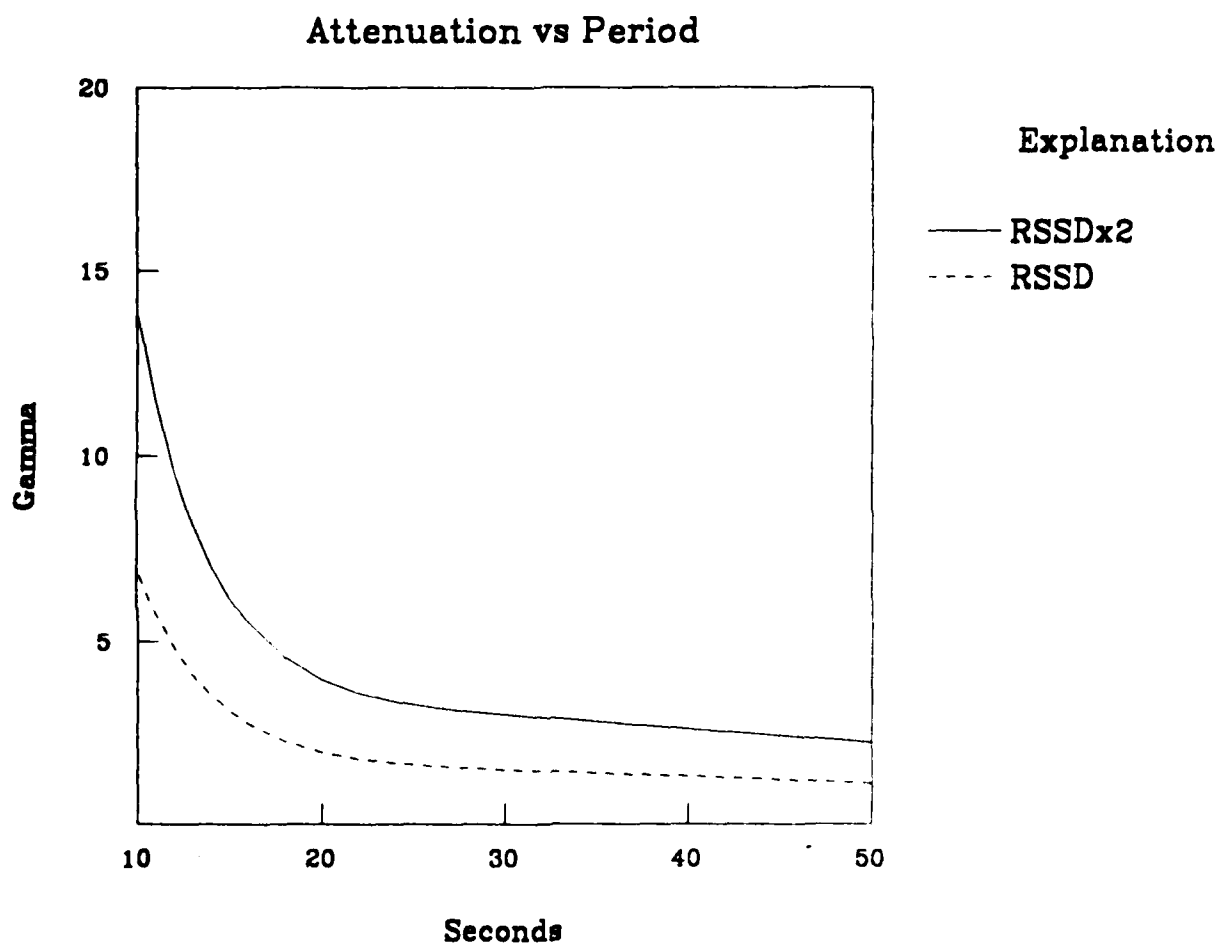


**Figure 4.** The two attenuation models for the generic portion of the hybrid propagation model are plotted versus period. Gamma is the attenuation coefficient at a given period. Model RSSDx2's attenuation is twice that of the RSSD model.  $M_s$  values calculated with synthetics using model RSSD are referred to as mixed path 1, while values determined from synthetics created using attenuation model RSSDx2 are referred to as mixed path 2.

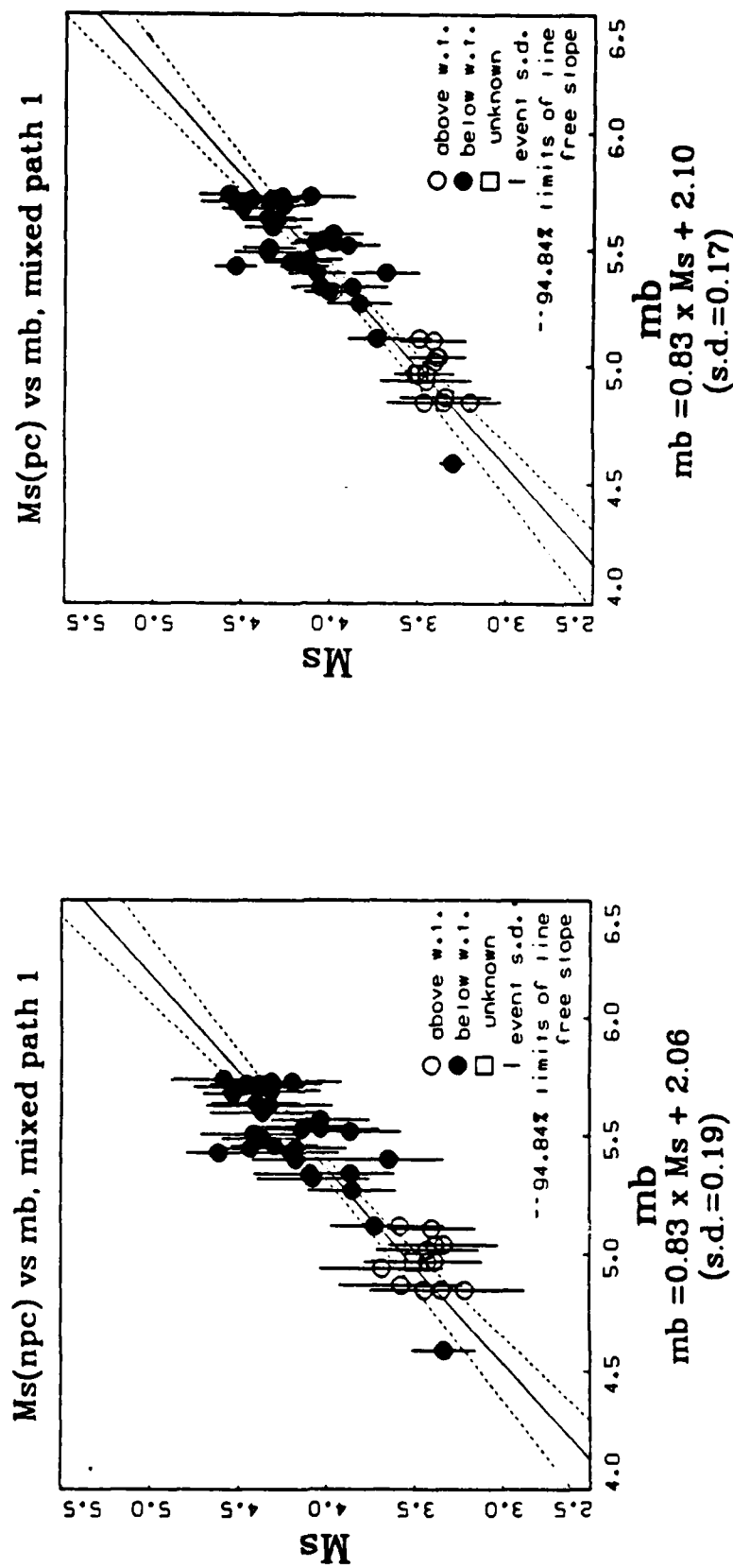
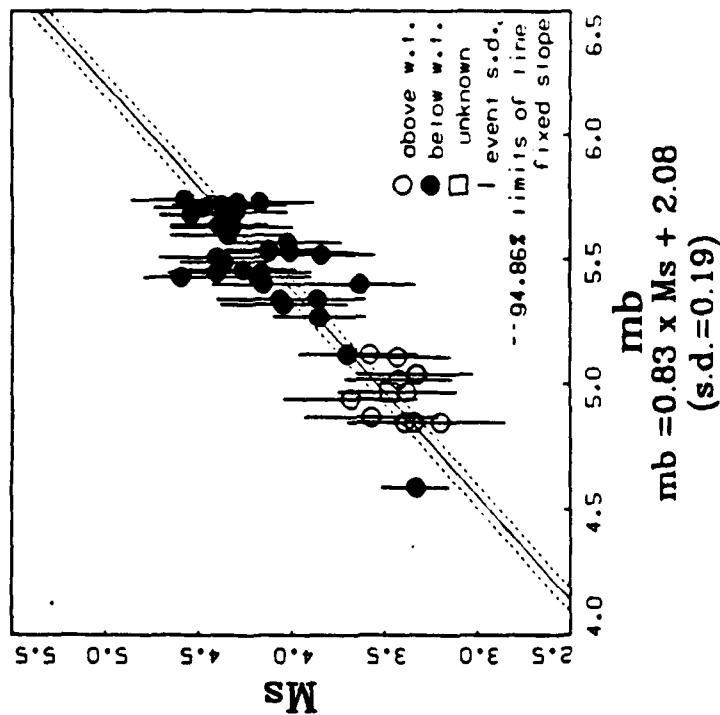


**Figure 5.**  $M_s$  vs. Lilwall  $m_b$  for a subset of the data set studied.  $M_s$  is calculated with path path Green's functions using the RSSD attenuation model (mixed path 1). and (a) without path corrections and (b) with path corrections. The best-fitting regression model is the solid line running through the data points.



**Ms(np) vs mb, mixed path 2**



**Ms(pc) vs mb, mixed path 2**

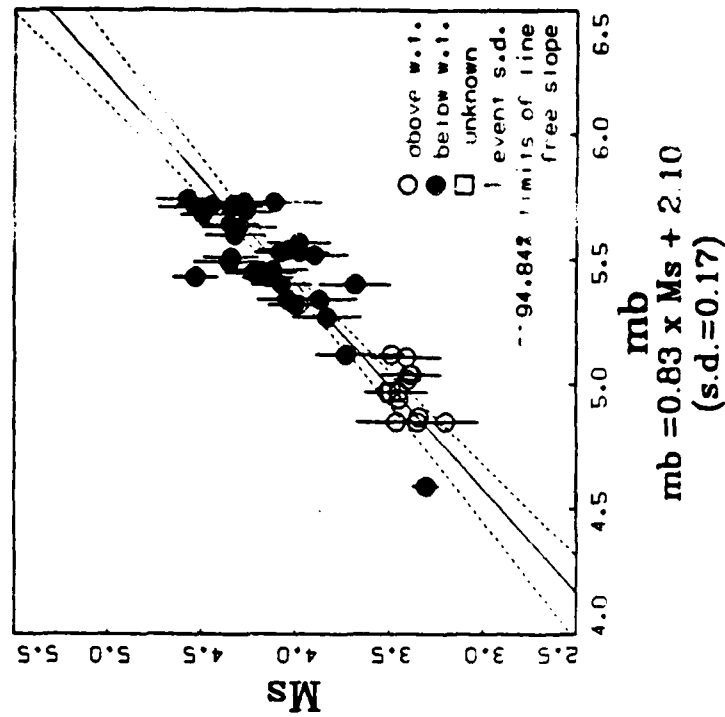
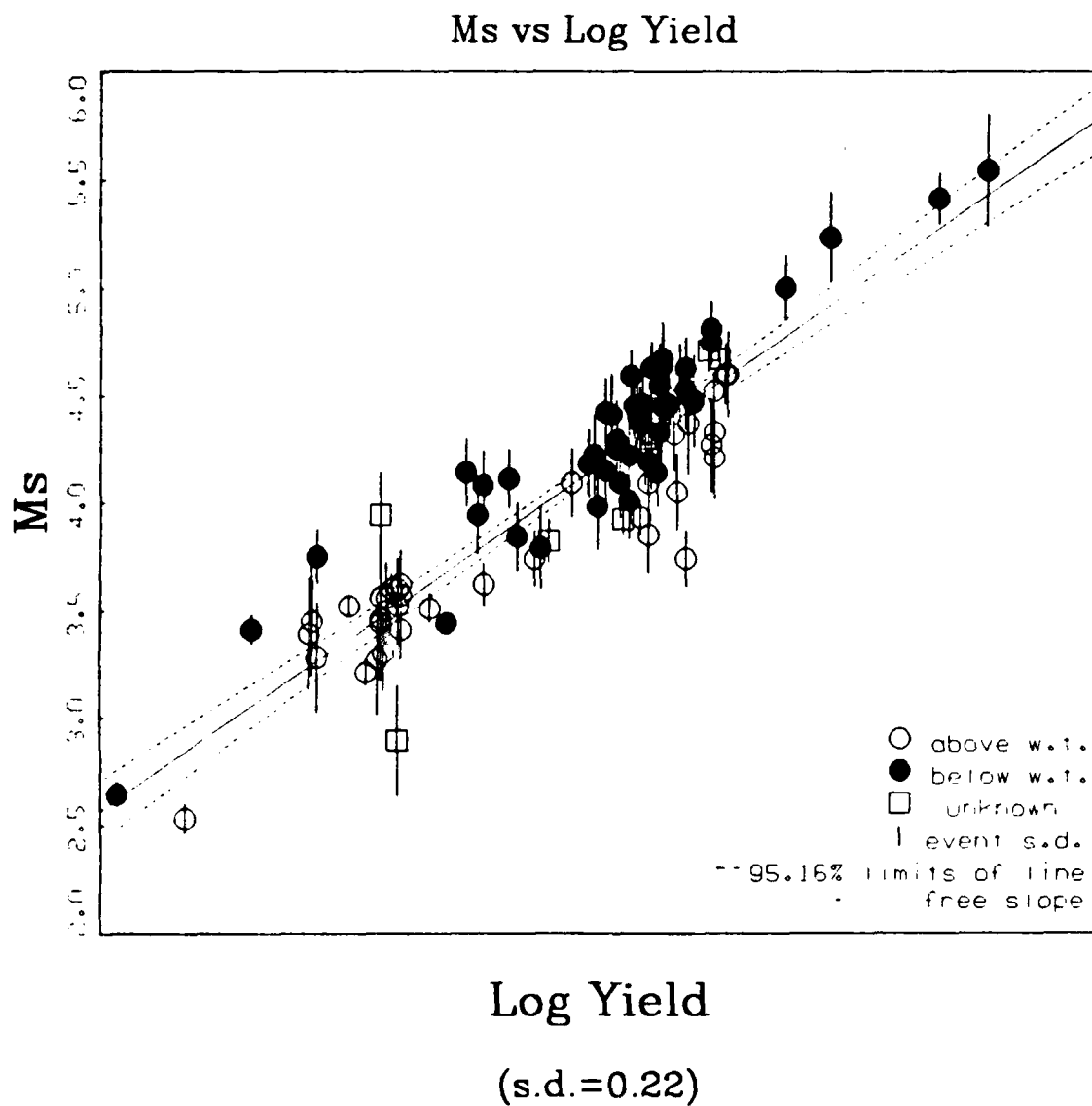
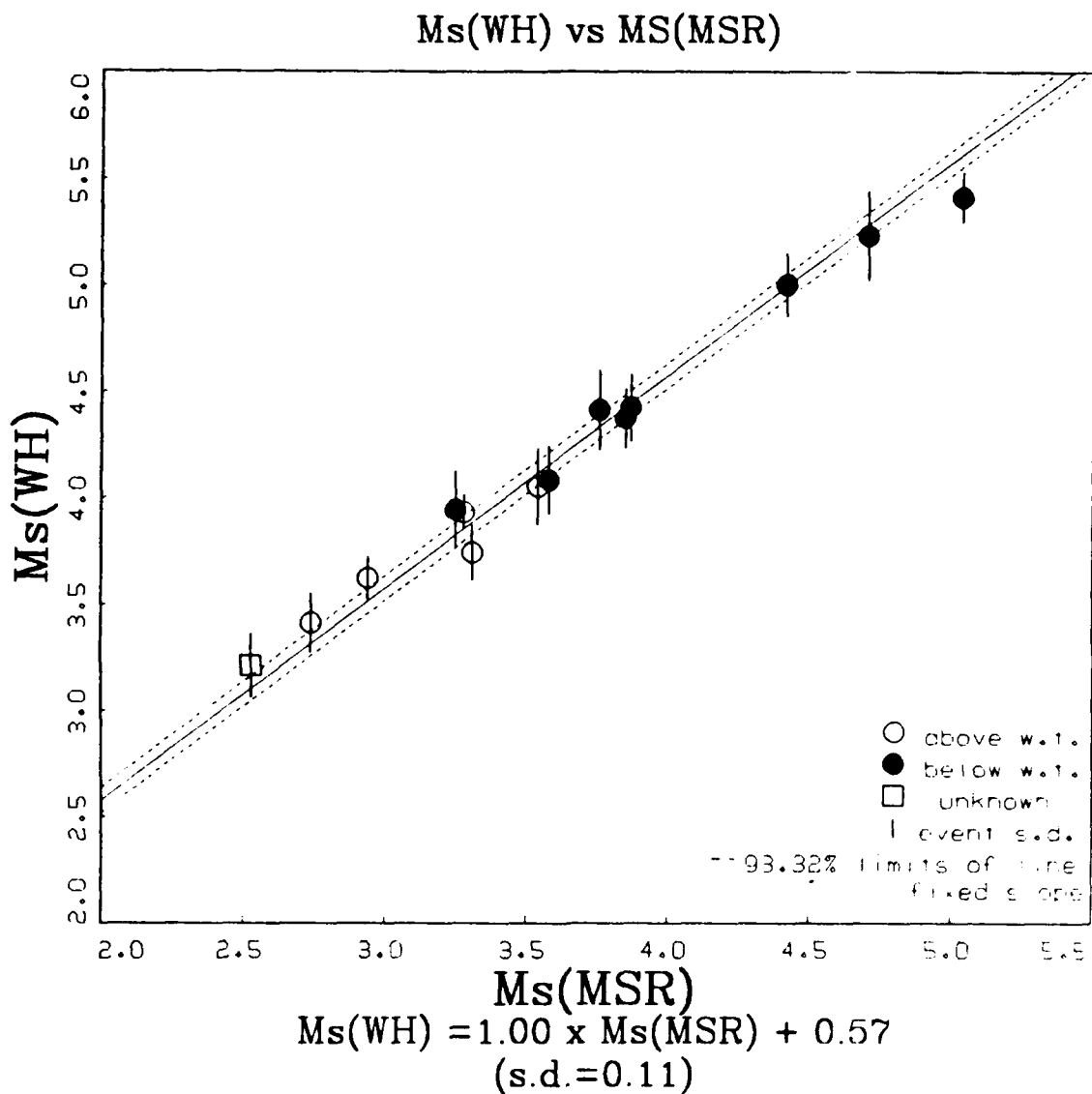


Figure 6.  $M_s$  vs. Lilwall  $m_b$  for a subset of the data set studied.  $M_s$  is calculated with path Green's functions which include the RSSDx2 attenuation model (mixed path 2), and (a) without path corrections and (b) with path corrections. The best-fitting regression model is the solid line running through the data points.



**Figure 7.**  $M_s$  vs. log yield for all available NTS event. Surface wave magnitudes were calculated with mixed path 1 Green's functions and path corrections. Scatter is mostly due to differences in shot medium and source region.



**Figure 8.** A comparison of our  $M_s$  values to those of Marshall *et al.* (1979) for 14 events. A slope of 1.0 was assumed for this regression. Although there is an off-set of 0.53 units, the relationship is very consistent.

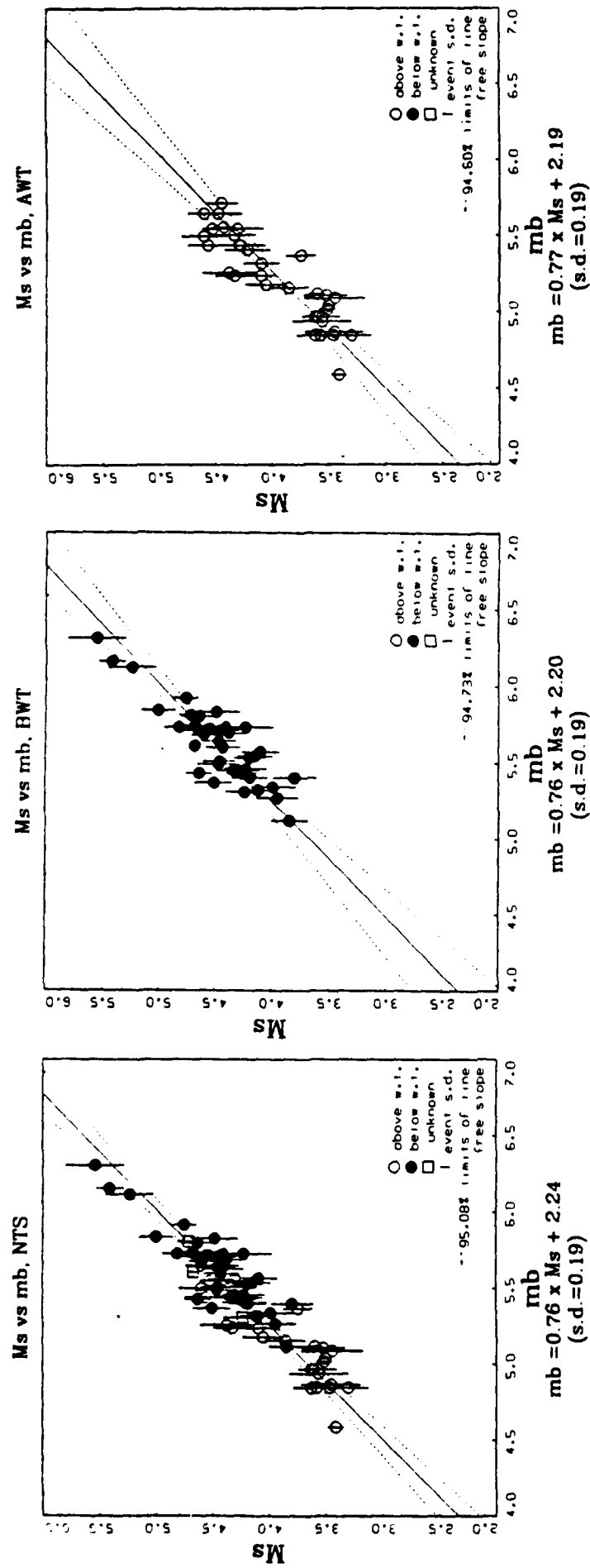


**Figure 9.**  $M_s$  vs. Lilwall  $m_b$  for (a) all available NTS events, (b) events below the water table and (c) events above the water table. The best-fitting linear regression model of the data is plotted as a solid line, with its equation printed below. The dashed lines are the two standard deviation confidence intervals of the regression line.

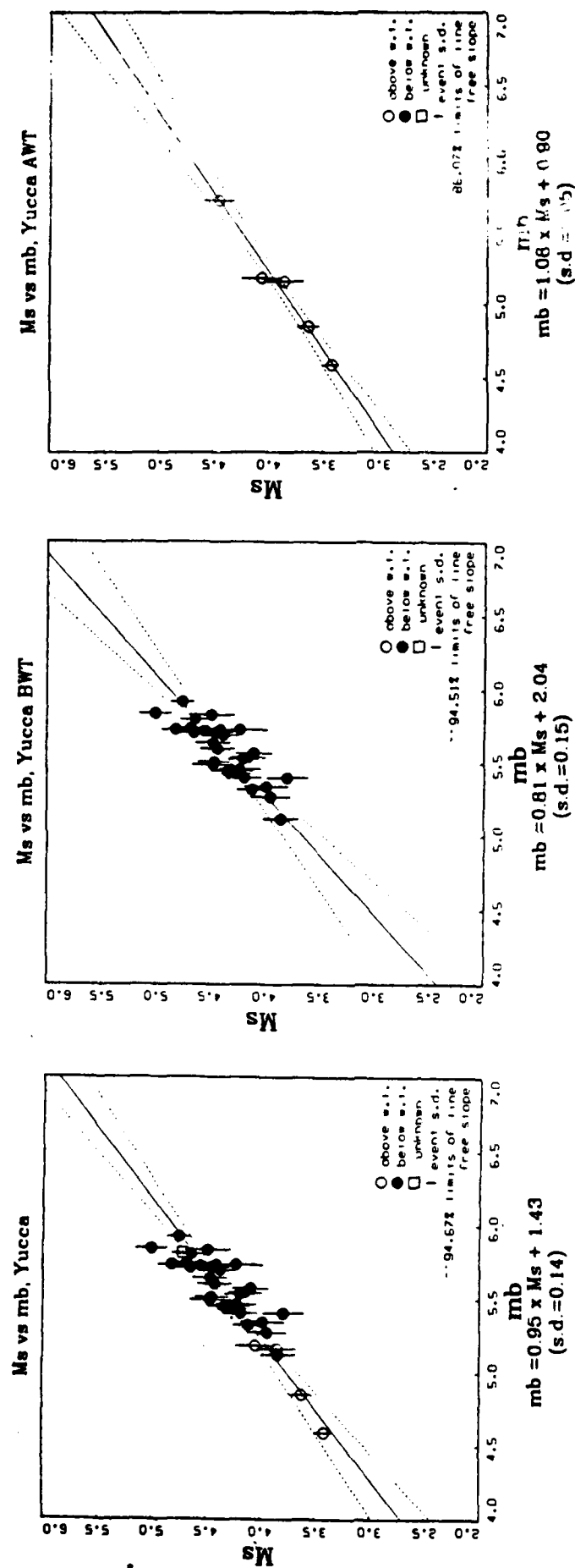


**Figure 10.**  $M_s$  vs. Lilwall  $m_b$  for (a) all available Yucca Flat events, (b) events below the water table and (c) events above the water table. The best-fitting linear regression model of the data is plotted as a solid line, with its equation printed below. The dashed lines are the two standard deviation confidence intervals of the regression line.

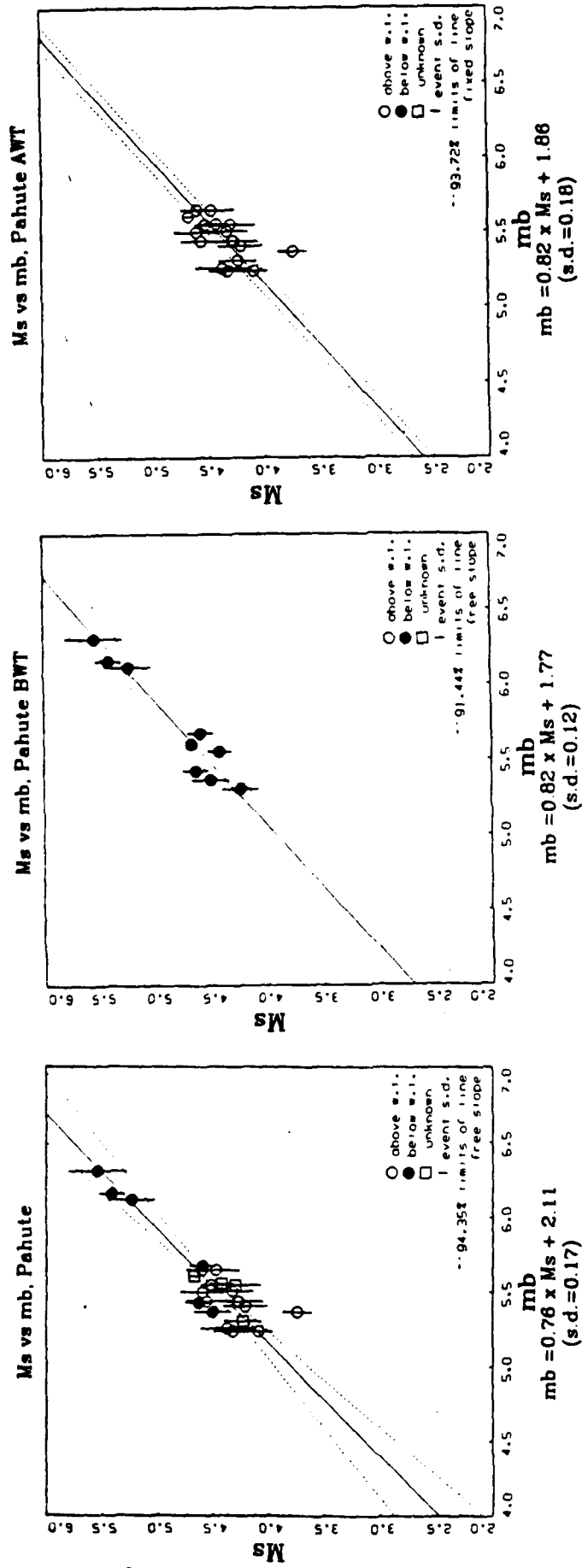
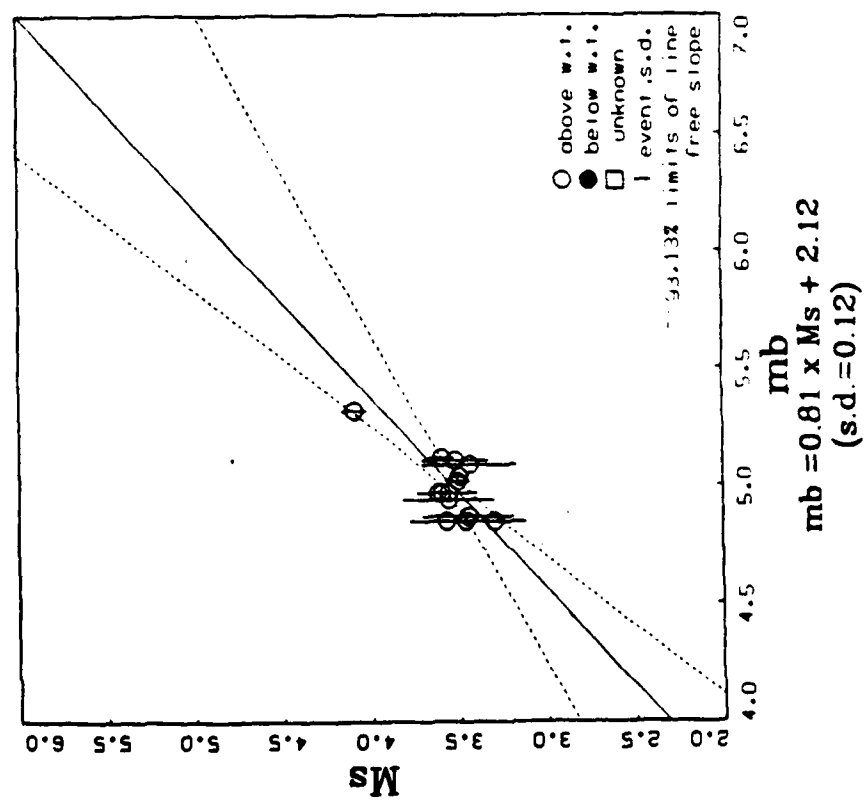


**Figure 11.**  $M_s$  vs. Lilwall  $m_b$  for (a) all available Pahute Mesa events, (b) events below the water table and (c) events above the water table. The best-fitting linear regression model of the data is plotted as a solid line, with its equation printed below. The dashed lines are the two standard deviation confidence intervals of the regression line.

Ms vs mb, Rainier AWT



Ms vs mb, Rainier AWT

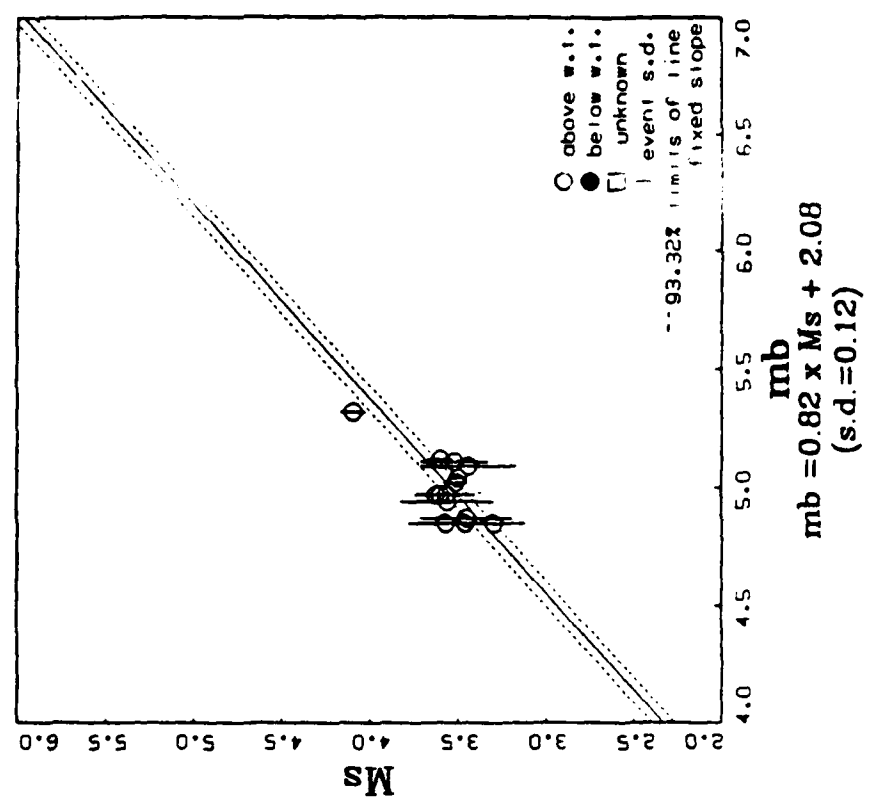


Figure 12.  $M_s$  vs. Lilwall  $m_b$  for all available Rainier Mesa events, with (a) being for a free slope regression which is poorly constrained, and (b) being for a fixed slope regression.

### **SECTION 3**

#### **A Note on the Relocation of Tibetan earthquakes**



## A Note on the Relocation of Tibetan Earthquakes

*Lian-She Zhao and Donald V. Helmberger*

Seismological Laboratory, 252 - 21

California Institute of Technology

Pasadena, California 91125

**Abstract.** Present ISC locations for earthquakes beneath Tibet indicate a random distribution of events down to a depth of about 50 km. This distribution might be expected from a relatively cool crust which would allow the seismo-genic zone to extend to such depths. A detailed investigation of the Tibetan earthquakes, with magnitude greater than 5.5 from 1964 to 1986, yields a distinctly different picture. Waveform modeling of depth phases such as  $pP$  indicates that only three or four events from this population is actually deeper than 25 km. These few events occur near the edges of the Plateau where active subduction is occurring as suggested by the thrust-like nature of their mechanisms. The events, averaging the entire population, occurred earlier than indicated by the ISC by about 3 seconds which leads to about a 1.5% and 0.5% over estimation of  $P_n$  and  $S_n$  velocities respectively applying ISC tables and standard flat-layered models. A more serious error occurs if the  $P_n$  and  $S_n$  velocities are determined by correcting for source depth but assuming the ISC origin times.

### Data, Analysis and Results

The events studied are listed in Table 1. Included in this table are the ISC determinations of depth, location and origin times of these events along with new estimates obtained from this investigation. The main objective of this report is to document these results and discuss their significance.

The data comes from the WWSSN chip library of the Seismological Laboratory at California Institute of Technology and consists mostly of long period P-waveforms and travel time picks read from the short period vertical components. The P-waveform data is used to constrain depths while the time picks are used to relocate and determine the origin times.

Errors in depth determinations using travel times become serious when no local stations are available, which is the case in Tibet. Essentially, there is a complete trade-off between origin time and depth. This difficulty can be circumvented by determining the depths independently by applying waveform modeling of the P-waveforms ( Langston and Helmberger 1975 ). This technique models the interference between direct P and free surface reflections to fix the epicentral depth although it is dependent on the velocity model of the source region. For example, assuming a surface layer of velocity 5 km/sec instead of 5.5 km/sec introduces a -1.0 km depth error, if the travel time difference between P and pP is used in modeling an event at a depth of 10 km. Thus, the source depth as determined by P waveform modeling is not very sensitive to crustal velocity and can be used to estimate the depths of the above events.

Many of the P-waveforms from Tibetan events have been modeled previously by a number of authors as indicated in the Table. These solutions have been checked by adding station coverage and, in general, found to be satisfactory. New depth estimates from modeling these events assuming the crustal model given in Zhao, Helmberger and Harkrider ( 1991 ), model TIP, are listed in Table 1.

We used the *P* wave travel times for relocations. These usually agreed with the ISC reports except in a few cases. More than 30 travel time picks distributed in azimuth are available for most events, thus providing excellent coverage. The station coverage is indicated in the Table 1. The relocation procedure used is a simple iteration scheme based on the definition of the ray parameter *p*, namely,

$$p = \frac{dT}{dR} \quad \text{or} \quad dR = \frac{dT}{p} \quad (1)$$

where  $dT$  is a small change in travel time associated with a small change in location.

We start with the origin time and location given by ISC. We define

$$dT = (T_{obs} - T_0) - T_c \quad (2)$$

where  $T_{obs}$  is the observed time pick,  $T_0$  is the origin time and  $T_c$  is the theoretical travel time based on an earth model. We assume TIP is the appropriate model at source region along with elevation correction and the model JB at the receiver stations. Station corrections were applied from the Dziewonski and Anderson's ( 1983 ) station correction table. By assuming that the  $dT$ 's are from a Gaussian distribution, we form the expectation estimate

$$\delta T = \frac{1}{n} \sum_{i=1}^{i=n} dT_i \quad (3)$$

and obtain a new origin time  $T_{0new} = T_{old} + \delta T$ . From equations (2) and (3), we can see that  $\delta T$  based on this new origin time is zero.

Then we use the new  $dT$  assuming  $T_{0new}$  given in Equation (2) to determine the mislocation  $dR$  from equation (1). We find the estimated mislocations in the North  $dx$  and East directions  $dy$ , namely,

$$dx = -\frac{1}{n} \sum_{i=0}^{i=n} dR_i \cos \Phi_i \quad (4)$$

$$dy = -\frac{1}{n} \sum_{i=0}^{i=n} dR_i \sin \Phi_i$$

assuming Gaussian distributions of the two direction mislocations, where  $\Phi_i$  is the azimuth of the source to the station (i). The new location of the earthquake is given by latitudes  $\theta_{new}$  and longitude  $\phi_{new}$ :

$$\theta_{new} = \theta_{old} + dx / R_E \quad (5)$$

$$\phi_{new} = \phi_{old} + dy / (R_E * \cos \theta_{old}).$$

Next we use the new origin time and new location as initial values, we use

equations (3) and (5) to calculate the new origin time and location, until some criteria is met. The criteria we used here is that the difference of the standard error

$$\sigma = \left( \frac{1}{n} \sum_{i=1}^n dT^2 \right)^{\frac{1}{2}}$$

and the standard error of the last iteration is smaller than 0.01

seconds. In this inversion we assume that the source depth is known, but this assumption is not required by the method. The method converges fast, normally under 5 iterations and the final results is not dependent on the initial input. Since changing the origin time trade-offs with  $T_c$ , the ISC locations are not effected much by changing the source depths.

After relocation, if the travel time residual of certain station is greater than three seconds, we consult the record again. If there is no problem with the pick, we use it; if the pick is not certain, buried in the noise, we may throw it away depending on the confidence of the pick, and event size, and all other station conditions. We throw away data that have a residual more than 5 seconds, even though the on-set is sharp. For example, UME and SEO produce more than 10 second residuals for some of the large earthquakes, and perhaps were caused by improper clock corrections or reporting errors.

We summerize our results in Table 1. In the table, "relc" means relocation, "D" is the distance between the relocated location and ISC location, " $\Delta T$ " is the relocated origin time difference from that of ISC. We also give number of stations used under "N". Under "Data", we give the references. The standard error of the origin time due to the inversion are also given in Table 1.

Figure 1 displays the contrast between the ISC depth determinations versus the new estimates. The results are dramatic where all the events occurring beneath the interior of Tibet become shallow events while the events along the frontal thrust zone become deeper. This implies a warm lower crust beneath Tibet similar to other tectonic regions of the world. In Figure 1, more than 90 per cent of the events occurred in the Tibetan Plateau, with magnitude greater than 5.5 since 1964, are included.

The mislocations are not very significant, the greatest is 21.1 km. The origin time corrections are more serious. Of the 59 earthquakes, 54 earthquakes occurred earlier than reported by ISC. The average of all earthquakes is -3.1 seconds, or these earthquakes have occurred 3.1 seconds earlier than reported by ISC. The worst case is -7.4 seconds for the second March 6, 1966 earthquake. Eleven of the events have a residual greater than 5.5 seconds.

Figure 2 shows the depth error verses origin time error, with respect to those of ISC. The new points should show a linear trend based on the assumed earth model. The least square fit of the data yields:

$$T=0.141H-1.43 \quad (6)$$

where T, origin time error in seconds, H depth mislocation in km is equal to relocated source depth minus ISC source depth. The standard error is 0.55 seconds if we assume that the origin times do not have errors and the standard error is 0.91 seconds if the error bars are included. The least square fitting method that includes error bars assumes that the probability distribution in the intervals of values between two ends is constant, the non-information probability density. The coefficient of H, 0.141, is dependent on the input model TIP, 6.16 to 6.55 km/sec of source layer, and the average ray parameter.

The offset of -1.43 seconds comes from the differences of earth model, the station correction and topographic correction relative to ISC assumption. For example, suppose we pick an event, August 20, 1986, 21 : 23 : 53.9 ( ISC origin time ), which falls near the line or on the average level ( Figure 2 ) and examine the various corrections. We relocate it and find a new origin time 21 : 23 : 54.21. In this calculation, we assume the source depth of 25 km given by ISC, and the JB model for both source region and the receiver structures, without correcting for the station delay. The travel time difference resulting from replacing the JB model by TIP is 0.4 seconds assuming a ray parameter of 0.07 sec/km. Station correction contributes about -0.2 seconds to

the origin times. The elevation correction of 5 km results in 0.8 seconds. The total of all these corrections accounts for the 1.4 second offset.

### Discussion

Barazangi and Ni ( 1982 ), and Ni and Barazangi ( 1983 ) used  $P_n$ - and  $S_n$ -waves crossing the Tibetan Plateau, and obtained velocities of 8.42 km/sec for  $P_n$ , and 4.73 km/sec for  $S_n$ . Holt and Wallace ( 1990 ) inverted the  $P_n$  waveform data and concluded that the  $P_n$  velocity is 8.24 km/sec beneath the Tibet region. Zhao et al. ( 1991 ) reported that the  $P_n$  velocity beneath the Tibetan Plateau is 8.3 km/sec, and that the  $S_n$  velocity is 4.6 km/sec by modeling SS and S waveforms. Zhao et al. ( 1991 ) did not use the absolute travel time in developing the velocity model TIP, but rather the differential travel times of SS-S, thus their results on the upper mantle velocities are not effected by the accuracy of the origin times. Using  $P_n$  waveforms and the travel times of  $P_n$  and  $S_n$  phase may introduce two percent higher lid velocity bias due to the non-planar characteristics of the Moho boundary beneath the Tibetan Plateau as given by Zhao and Helmberger ( 1991 ).

Models based on absolute travel times obviously do depend on the origin time. For example, Holt and Wallace ( 1990 ) used 24 events from population given in Table 1. They assumed these events are shallow with depths similar to the relocated depths given in Table 1, and applied the ISC origin times with corrections of the source depth, dipping Moho and 70 km crust. If they did not correct the origin times, their  $P_n$  travel times would be 3.6 seconds too short relative to the results presented in Table 1 on average. Although they over corrected the effects of the velocity structure of source region, two seconds, ( they assume that below the crust, the Tibetan Plateau has a JB velocity distribution ), their result of  $P_n$  velocity 8.24 km/sec is reasonable.

The origin time effects on the  $P_n$  and  $S_n$  results from the regional phases are slightly less dramatic, if both the source depths and origin times of ISC are used. This

is because the deeper source depth of ISC compensates its later origin time. The effects of origin time errors and depth errors on the travel times of  $P_n$  and  $S_n$  are given by

$$\Delta T_{P_n} = -0.034H + 1.43 \quad (7)$$

and

$$\Delta T_{S_n} = 0.044H + 1.43 \quad (8)$$

assuming that the compressional velocity 6.2 km/sec, the shear velocity 3.5 km/sec for the crust and velocities for the mantle are 8.3 and 4.6  $\text{km s}^{-1}$  respectively. Averaging over all the relocated earthquakes, yields  $\Delta T_{P_n} = +1.8$  seconds and  $\Delta T_{S_n} = +0.95$  seconds.

The travel time of  $P_n$  phase recorded at a station 10 degrees away from the source is about 140 seconds. From Equation (7), the  $P_n$  travel time is 1.8 seconds longer than that predicted by using ISC origin time and source depth, averaging over all the relocated earthquakes. Considering this travel time difference, we get a  $P_n$  velocity of 8.43  $\text{km s}^{-1}$  by using the  $P_n$  travel time predicted by using ISC source depth and origin time if the real  $P_n$  velocity is 8.30  $\text{km s}^{-1}$ . This velocity difference almost covers the possible models proposed for the Tibet region discussed earlier.

The  $S_n$  travel time of a source-receiver distance of 10 degrees is about 260 seconds. From Equation (8), the  $S_n$  travel time is 0.95 seconds longer than that predicted by using ISC origin time and source depth, averaging over all the earthquakes we relocated. Considering this travel time difference, we get a  $S_n$  velocity of 4.62  $\text{km s}^{-1}$  by using  $S_n$  travel time predicted by using ISC source depth and origin time if the real  $S_n$  velocity is 4.60  $\text{km s}^{-1}$ . Thus the origin time and source depth given by ISC do not make very much difference to the  $S_n$  velocity if only  $S_n$  travel times are used. In short the travel time errors introduced by the ISC origin times and source depths lead to about 1.5 per cent over-estimate of the  $P_n$  velocity and about 0.5

per cent over-estimated of the  $S_n$  velocity.

The ISC location of the earthquakes are not badly mislocated. However this mislocation may introduce more than 5 seconds to regional Love wave travel times, since the group velocity of the maximum amplitude of Love waves is about 3.5 km/sec. Thus, this small mislocation can lead to a bias in the velocity model. For example, suppose we consider the events discussed by Zhao et al. ( 1991 ), see Table 2. In this table,  $\Delta D$  is the distance between the old and new location in kms at a number of stations surrounding Tibet. Positive values mean that the new distances are larger,  $\Delta T_{syn}$  is the synthetic travel time correction caused by the distance change assuming a 3.5 km/sec group velocity.  $\Delta T_{obs}$  is the observed travel time change due to the change in origin time, and  $\delta T$  is defined as  $T_{obs} - T_{syn}$ . From this table, we see that the velocity structure derived by using the travel times of Love waves are about one percent exaggerated. Zhao et al. ( 1991 ) claim that TIP's crustal model is mainly for the southern part of the Tibetan Plateau, If we include the effects of the new origin times and locations given here, the crustal velocity structure appropriate for the northern part of the Plateau is about three percent slower than indicated by TIP.

In conclusion, we investigated more than 90 per cent of the Tibetan earthquakes and found that most of these events are shallower than reported by ISC; most are no deeper than 20 km. We relocated 59 of them, and found that the average origin time is 3.06 seconds earlier than that reported by ISC. Eleven of them are more than 5.5 seconds earlier than reported. Applying these corrections to  $P_n$  and  $S_n$  travel times explains why many authors have over-estimated the upper mantle velocities beneath the Tibetan Plateau.

#### Acknowledgments

We would like to thank Bradley Woods for his review. This research was supported by the National Science Foundation grant EAR-89-04767 and by the Advanced



Research Projects Agency of the Department of Defense and was monitored by the Air Force Geophysical Laboratory under the contract F19628-89-K0028. Contribution No. 5033, Division of Geological and Planetary Sciences, California Institute of Technology, Pasadena, California.

#### REFERENCES

- Baranowski, H., H. Armbruster, L. Seeber and P. Molnar, Focal depths and fault plane solutions of earthquakes and active tectonics of the Himalaya, *J. Geophys. Res.*, **89**, 6919-6928, 1984.
- Barazangi, M., and J. Ni, Velocities and propagation characteristics of  $P_n$  and  $S_n$  beneath the Himalayan arc and Tibetan Plateau: possible evidence for underthrusting of Indian continental lithosphere beneath Tibet, *Geology*, **10**, 179-185, 1982.
- Chandra, U., Seismicity, earthquake mechanisms and tectonics along the Himalayan mountain range and vicinity, *Phys. Earth Planet. Inter.*, **16**, 109-131, 1978.
- Dziewonski, A. M, and D. L. Anderson, Travel times and station corrections for P waves at teleseismic distances, *J. Geophys. Res.*, **88**, 3295-3314, 1983.
- Fan, Guangwei and J. F. Ni, Source parameters of the 13 February 1980, Karakorum earthquake, *Bull. Seis. Soc. Am.*, **79**, 945-954, 1989.
- Fitch, T. J. Earthquake mechanism in the Himalayan, Burmese, and Andaman regions and continental tectonics in central Asia, *J. Geophys. Res.*, **75**, 2699-2709, 1970.
- Holt, W. E. and T. C. Wallace, Crustal thickness and upper mantle velocities in the Tibetan Plateau region from the inversion of regional  $P_n$  waveforms: Evidence for a thick upper mantle lid beneath southern Tibet, *J. Geophys. Res.* **95**, 12499-12525, 1990.
- Langston, C. A., and D. V. Helmberger, A procedure for modeling shallow dislocation sources, *Geophys. J. R. astr. Soc.*, **42**, 117-130, 1975.
- Molnar, P., T. J. Fitch, and F. T. Wu, Fault plane solutions of shallow earthquakes and

- contemporary tectonics in Asia, *Earth Planet. Sci. Let.*, **19**, 101-112, 1973.
- Molnar, P. and W.-P. Chen, Focal depths and fault plane solutions of earthquakes under the Tibetan Plateau, *J. Geophys. Res.*, **88**, 1180-1196, 1983.
- Molnar, P. and W.-P. Chen, S-P wave travel time residuals and lateral inhomogeneity in the mantle beneath Tibet and the Hymalaya, *J. Geophys. Res.*, **89**, 6911-6917, 1984.
- Molnar, P. and H. Lyon-Caen, Fault plane solutions of earthquakes and active tectonics of the Tibetan Plateau and its margins, *Geophys. J. Int.*, **99**, 123-153, 1989.
- Nelson, M. R., R. McCaffrey, and P. Molnar, Source parameters for 11 earthquakes in the Tien Shan, Central Asia, determined by P and SH waveform inversion, *J. Geophys. Res.*, **92**, 12629-12648, 1987.
- Ni, J., and M. Barazangi, High frequency seismic wave propagation beneath the Indian Shield, Himalayan arc, Tibetan Plateau and surrounding regions: High uppermost mantle velocities and efficient Sn propagation beneath Tibet, *Geophys. J. R. astr. Soc.*, **72**, 665-681, 1983.
- Ni, J., and M. Barazangi, Seismotectonics of the Himalayan collision zone: geometry of the underthrusting Indian plate beneath the Himalaya, *J. Geophys. Res.*, **89**, 1147-1163, 1984.
- Zhao, Lian-She, D. V. Helmberger, and D. G. Harkrider, Shear-velocity structure of the crust and upper mantle beneath Tibetan and southeastern China. *Geophys. J. Int.*, **105**, 713-730, 1991.
- Zhao, Lian-She and D. V. Helmberger, Non-planar Moho effects on the lid velocity, manuscript in preparation, 1991.
- Zhou, Huilan, Hsui-Lin Liu, and H. Kanamori, Source processes of large earthquakes along the Xianshuihe fault in southwestern China, *Bull. Seis. Soc. Am.*, **73**, 537-551, 1983.

Table 1. Relocation of Tibetan Earthquakes

Date Mo Da Yr	Origin Time			$\Delta T$ (sec)	Location ( $^{\circ}N, ^{\circ}E$ )				D (km)	Depth		Mb	Data
	h m	relc	ISC		relc	ISC				relc	ISC		
03 16 64	0105	13.5 $\pm$ 1.2	19.8	-6.3	37.11	95.60	36.95	95.50	20.1	10	50	5.9	21 in
09 26 64	0046	-3.1 $\pm$ 1.3	02.6	-5.7	29.91	80.55	29.96	80.46	10.6	18	50	5.8	32 abin
10 21 64	2309	15.8 $\pm$ 1.3	19.0	-3.2	28.22	93.87	28.04	93.75	10.6	15	37	5.9	32 adhn
01 12 65	1332	22.1 $\pm$ 1.1	24.1	-2.0	27.41	87.85	27.40	87.84	1.8	15	23	5.8	27 anf
02 05 66	1512	27.2 $\pm$ 1.0	32.9	-5.7	26.29	103.20	26.22	103.21	8.3	4	42	5.6	39 en
02 13 66	1044	36.0 $\pm$ 1.2	38.0	-2.0	26.27	103.25	26.17	103.25	10.6	4	6	5.4	32 en
03 06 66	0210	52.1 $\pm$ 0.8	52.0	+0.1	31.50	80.53	31.51	80.55	2.2	11	5	5.3	33 n
03 06 66	0215	49.8 $\pm$ 1.1	57.2	-7.4	31.48	80.50	31.49	80.50	10.0	8	50	6.0	37 gn
06 27 66	1041	04.2 $\pm$ 1.2	08.1	-3.9	29.70	80.89	29.62	80.83	10.4	15	33	6.0	42 abhn
08 15 66	0215	29.9 $\pm$ 1.1	28.0	+1.9	28.70	78.91	28.67	78.93	4.5	25	5	5.6	31 fn
09 26 66	0510	54.5 $\pm$ 1.1	56.2	-1.7	27.53	92.73	27.49	92.61	12.9	17	20	5.4	34 bn
09 28 66	1400	18.5 $\pm$ 1.3	21.0	-2.5	27.55	100.10	27.53	100.08	2.5	10	12	5.7	42 en
10 14 66	0104	40.0 $\pm$ 1.2	42.9	-2.9	36.50	87.46	36.45	87.43	6.3	8	14	5.2	32 ghn
12 16 66	2052	14.1 $\pm$ 1.5	16.3	-2.2	29.66	80.84	29.62	80.79	6.1	12	19	5.7	40 abhn
03 14 67	0658	02.8 $\pm$ 1.5	04.4	-1.6	28.57	94.37	28.41	94.29	19.0	15	20	5.8	36 adhn
08 15 67	0921	-2.6 $\pm$ 0.9	03.3	-5.9	31.23	93.56	31.05	93.56	17.0	8	36	5.5	25 en
08 30 67	0422	01.8 $\pm$ 1.2	05.1	-3.2	31.71	100.24	31.61	100.26	11.7	10	24	6.1	35 emn
08 30 67	1108	44.8 $\pm$ 1.4	51.0	-6.2	31.73	100.28	31.57	100.31	18.1	8	35	5.2	28 emn
02 19 70	0710	00.2 $\pm$ 1.4	01.5	-1.3	27.47	94.02	27.40	93.96	9.7	10	12	5.4	19 hfn
02 24 70	0207	31.5 $\pm$ 1.4	36.0	-4.5	30.66	103.02	30.61	103.05	6.2	7	24	5.8	27 in
03 24 71	1354	15.2 $\pm$ 1.2	18.4	-3.2	35.46	98.03	35.46	98.04	0.9	7	13	5.7	40 in
04 03 71	0449	-2.2 $\pm$ 1.4	03.1	-5.3	32.19	95.08	32.16	94.99	8.9	8	27	5.6	40 n
04 03 71	0450	39.8 $\pm$ 1.4	45.8	-5.6	32.10	95.10	32.10	95.19	8.9	8	33	5.3	25 er
05 22 71	2003	27.3 $\pm$ 1.3	31.9	-4.6	32.42	92.11	32.36	92.11	6.7	8	29	5.5	43 egn
08 30 72	1514	05.0 $\pm$ 1.3	07.5	-2.5	36.64	96.35	36.65	96.35	1.3	15	17	5.5	31 in
08 30 72	1847	38.6 $\pm$ 1.2	40.3	-1.7	36.71	96.46	36.56	96.35	18.9	19	16	5.5	30 in
09 03 72	1648	24.4 $\pm$ 0.9	29.5	-5.1	36.06	73.31	35.94	73.33	13.6	12	45	6.2	37 aehn
02 06 73	1037	06.1 $\pm$ 1.5	07.0	-0.9	31.38	100.54	31.33	100.49	6.7	10	5	5.9	37 ma
02 07 73	1606	20.7 $\pm$ 1.3	25.8	-5.1	31.58	100.28	31.50	100.33	10.2	8	35	5.9	35 en
07 14 73	0451	16.1 $\pm$ 1.5	20.0	-3.9	35.25	86.41	35.16	86.40	10.0	6	22	5.9	48 egar
07 14 73	1339	24.1 $\pm$ 0.7	29.4	-5.3	35.30	86.51	35.21	86.54	10.7	7	29	5.7	18 egn
01 15 75	1134	37.0 $\pm$ 1.2	41.0	-4.0	29.46	101.78	29.41	101.78	5.3	10	29	5.5	41 en
01 19 75	0801	57.6 $\pm$ 1.4	58.0	-0.4	32.39	78.58	32.39	78.50	7.5	9	1	6.2	36 ghn
08 16 76	1406	44.5 $\pm$ 1.4	45.0	-0.5	32.80	104.09	32.78	104.09	3.8	12	9	6.1	35 en
08 21 76	2149	49.1 $\pm$ 1.1	52.0	-2.9	32.58	104.29	32.59	104.29	1.2	5	15	6.0	17 kn
08 23 76	0330	02.9 $\pm$ 1.2	06.0	-3.1	32.55	104.24	32.49	104.18	8.8	8	17	6.2	20 kn
11 18 77	0520	06.7 $\pm$ 1.1	10.3	-3.4	32.75	88.44	32.65	88.39	12.4	10	24	5.7	22 ehn
03 29 79	0707	15.3 $\pm$ 1.3	22.0	-6.7	32.55	97.28	32.44	97.26	12.9	10	45	5.4	32 en
02 13 80	2209	32.3 $\pm$ 1.2	30.8	+1.5	36.61	76.85	36.47	76.86	15.1	90	74	6.0	36 en
02 22 80	0302	42.8 $\pm$ 0.7	45.2	-2.4	30.65	88.61	30.55	88.60	11.0	10	14	5.7	34 hahn
06 01 80	0619	-5.2 $\pm$ 1.1	01.2	-6.3	39.06	95.63	38.91	95.60	16.5	12	50	5.2	26 in
06 24 80	0735	44.7 $\pm$ 1.2	44.7	+0.0	33.02	88.46	33.00	88.55	9.2	11	3	5.1	25 in
07 29 80	1458	39.4 $\pm$ 1.0	41.6	-2.2	29.64	81.08	29.63	81.09	7.5	15	23	6.1	39 hahn
08 23 80	2136	48.9 $\pm$ 1.5	49.0	-0.1	33.07	75.69	32.96	75.75	13.0	14	3	5.2	27 in
08 23 80	2150	-0.5 $\pm$ 2.0	01.0	-1.5	32.89	75.83	32.90	75.80	3.2	13	12	5.2	28 in
10 07 80	0932	03.0 $\pm$ 1.3	08.7	-5.7	35.63	82.21	35.62	82.14	6.5	4	32	5.4	29 in
11 19 80	1900	45.5 $\pm$ 0.9	45.0	+0.5	27.47	88.80	27.40	88.80	7.9	14	1	6.0	45 hahn
01 23 81	2113	46.5 $\pm$ 1.2	52.0	-5.5	30.99	101.14	30.89	101.15	11.4	8	34	5.7	22 ma
06 09 81	2208	17.6 $\pm$ 1.3	18.6	-1.0	34.65	91.34	34.51	91.42	21.1	10	10	5.3	29 en
01 23 82	1737	25.8 $\pm$ 1.2	29.2	-3.4	31.74	82.27	31.68	82.28	6.6	10	25	6.0	33 in
06 15 82	2324	26.5 $\pm$ 1.2	28.8	-2.3	31.91	99.92	31.85	99.92	7.1	7	10	5.5	34 en
02 13 83	0140	08.2 $\pm$ 1.9	09.2	-0.9	40.05	75.17	39.99	75.24	9.0	5	0	5.6	29 en
05 20 85	1511	35.6 $\pm$ 0.5	38.9	-3.3	35.62	87.28	35.56	87.20	9.9	8	19	5.2	13 in
04 26 86	0735	12.6 $\pm$ 1.3	16.2	-3.6	32.23	76.39	32.15	76.40	11.8	13	33	5.2	28 in
06 20 86	1712	43.5 $\pm$ 1.2	47.2	-3.7	31.23	86.79	31.22	86.82	3.0	15	33	5.9	27 ejin
07 06 86	1924	20.9 $\pm$ 1.2	23.1	-2.2	34.55	80.15	34.45	80.20	12.3	5	9	5.7	28 in
07 16 86	2203	07.7 $\pm$ 1.6	07.0	+0.7	31.10	78.08	31.05	78.00	8.8	13	4	5.6	25 in
08 20 86	2123	51.2 $\pm$ 1.2	53.9	-2.8	34.65	91.49	34.56	91.64	17.1	11	25	5.6	24 in
08 26 86	0943	-1.2 $\pm$ 1.4	00.5	-1.7	37.83	101.55	37.74	101.52	10.7	7	8	6.1	29 in

a Baranowski et al., 1984

b Chandra, 1978

c Fan and Ni, 1989

d Fitch, 1970

e Holt and Wallace, 1990

f Molnar et al., 1973

g Molnar and Chen, 1983

h Molnar and Chen, 1984

i Molnar and Lyon-Caen, 1989

j Nelson et al., 1987

k Ni and Barazangi, 1984

l Zhao et al., 1989

m Zhou et al., 1983

n this study

**Table 2.**

Data	Time	Station	Distance	$\Delta D$	$\Delta T_{\text{syn}}$	$\Delta T_{\text{obs}}$	$\delta T$
08 15 67	0921	SHL	649	19.2	5.5	5.9	0.4
08 30 67	1108	NDI	2242	-2.1	-0.6	6.2	6.8
08 30 67	1108	LAH	2456	-4.9	-1.4	6.2	7.6
08 30 72	1514	NDI	1995	-0.4	-0.1	2.5	2.6
02 07 73	1606	NDI	2241	-4.4	-1.3	5.1	6.4
02 07 73	1606	NIL	2540	-6.6	-1.9	5.1	7.0
06 15 82	2324	NDI	2209	0.4	0.1	2.3	2.2

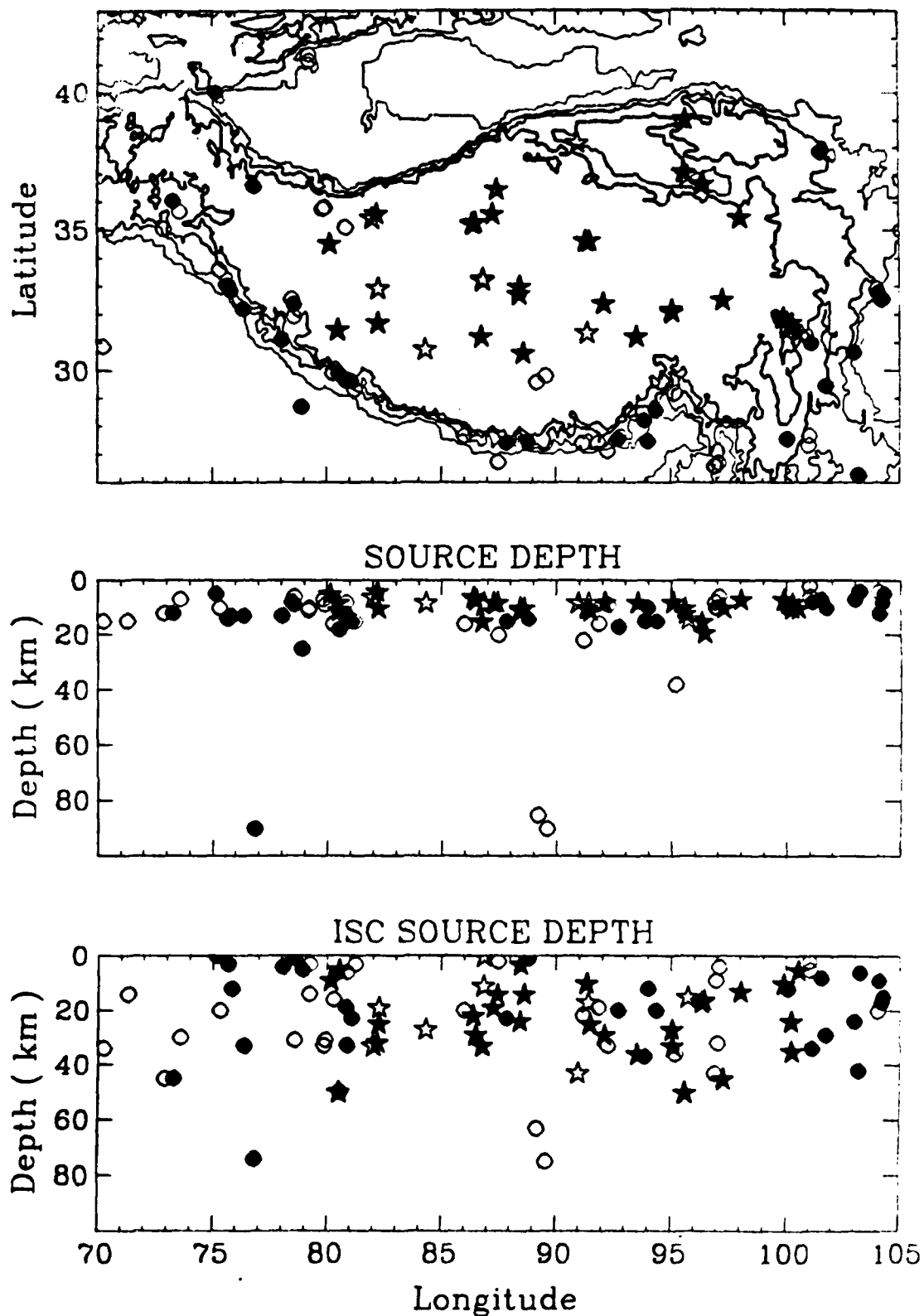


Figure 1. The source depths before and after relocation. The top plot shows the locations of the earthquakes whose depths are plotted below. The dots are the earthquakes on the Tibetan boundary, the stars are inside Tibet. The middle plot shows the source depth distribution after relocation and the bottom plot shows ISC depths. The solid symbols indicate the events that we relocated in this study.

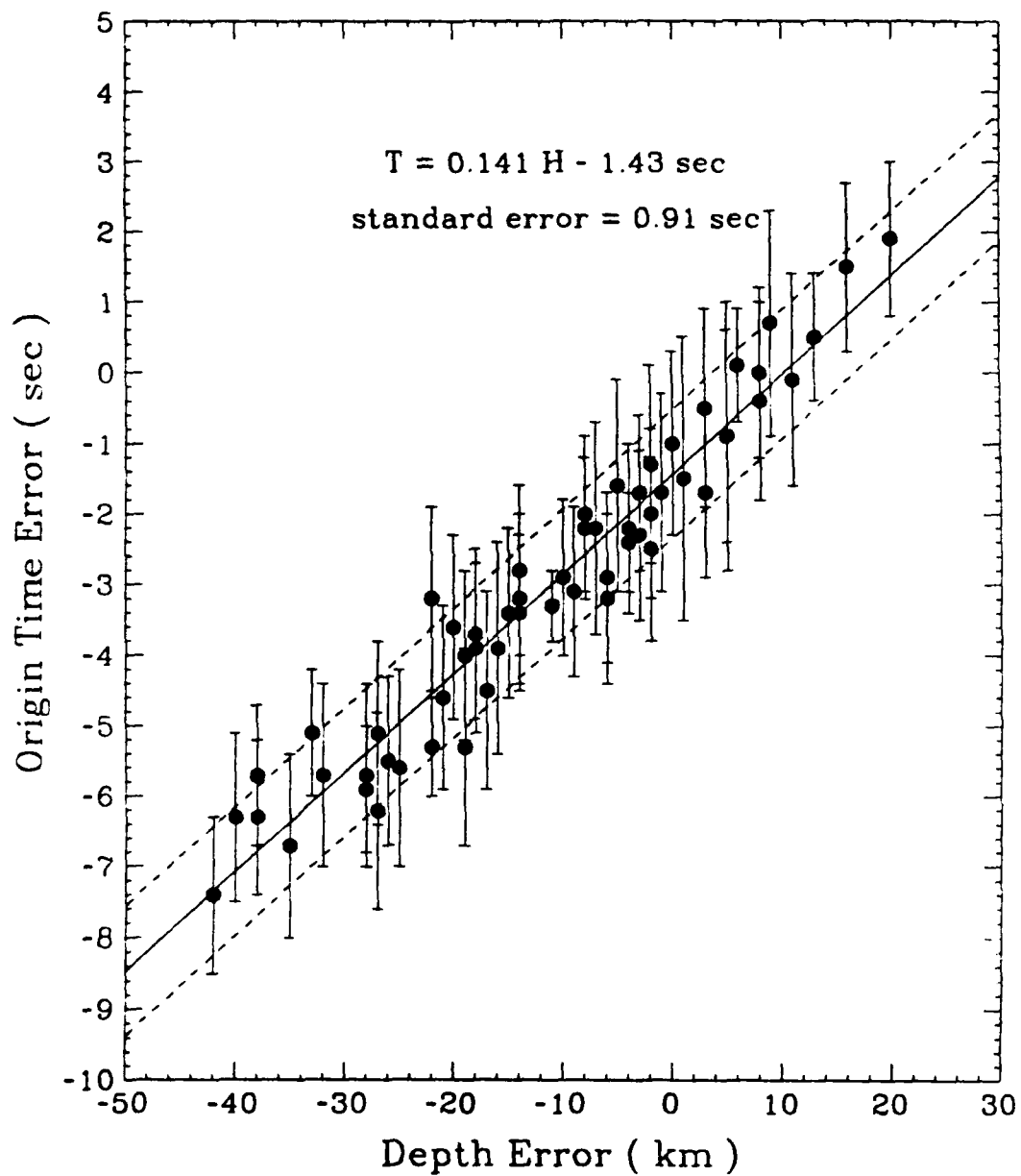


Figure 2. Origin time error verses depth error respects to the ISC reports. The vertical lines show the error bars.

Prof. Thomas Ahrens  
Seismological Lab, 252-21  
Division of Geological & Planetary Sciences  
California Institute of Technology  
Pasadena, CA 91125

Prof. Keiiti Aki  
Center for Earth Sciences  
University of Southern California  
University Park  
Los Angeles, CA 90089-0741

Prof. Shelton Alexander  
Geosciences Department  
403 Deike Building  
The Pennsylvania State University  
University Park, PA 16802

Dr. Ralph Alewine, III  
DARPA/NMRO  
3701 North Fairfax Drive  
Arlington, VA 22203-1714

Prof. Charles B. Archambeau  
CIRES  
University of Colorado  
Boulder, CO 80309

Dr. Thomas C. Bache, Jr.  
Science Applications Int'l Corp.  
10260 Campus Point Drive  
San Diego, CA 92121 (2 copies)

Prof. Muawia Barazangi  
Institute for the Study of the Continent  
Cornell University  
Ithaca, NY 14853

Dr. Jeff Barker  
Department of Geological Sciences  
State University of New York  
at Binghamton  
Vestal, NY 13901

Dr. Douglas R. Baumgardt  
ENSCO, Inc  
5400 Port Royal Road  
Springfield, VA 22151-2388

Dr. Susan Beck  
Department of Geosciences  
Building #77  
University of Arizona  
Tucson, AZ 85721

Dr. T.J. Bennett  
S-CUBED  
A Division of Maxwell Laboratories  
11800 Sunrise Valley Drive, Suite 1450  
Reston, VA 22091

Dr. Robert Blandford  
AFTAC/IT, Center for Seismic Studies  
1330 North 17th Street  
Suite 1450  
Arlington, VA 22209-2308

Dr. G.A. Bollinger  
Department of Geological Sciences  
Virginia Polytechnical Institute  
21044 Derring Hall  
Blacksburg, VA 24061

Dr. Stephen Bratt  
Center for Seismic Studies  
1300 North 17th Street  
Suite 1450  
Arlington, VA 22209-2308

Dr. Lawrence Burdick  
Woodward-Clyde Consultants  
566 El Dorado Street  
Pasadena, CA 91109-3245

Dr. Robert Burrige  
Schlumberger-Doll Research Center  
Old Quarry Road  
Ridgefield, CT 06877

Dr. Jerry Carter  
Center for Seismic Studies  
1300 North 17th Street  
Suite 1450  
Arlington, VA 22209-2308

Eric Chael  
Division 9241  
Sandia Laboratory  
Albuquerque, NM 87185

Prof. Vernon F. Cormier  
Department of Geology & Geophysics  
U-45, Room 207  
University of Connecticut  
Storrs, CT 06268

Prof. Anton Dainty  
Earth Resources Laboratory  
Massachusetts Institute of Technology  
42 Carleton Street  
Cambridge, MA 02142

Prof. Steven Day  
Department of Geological Sciences  
San Diego State University  
San Diego, CA 92182

Art Frankel  
U.S. Geological Survey  
922 National Center  
Reston, VA 22092

Marvin Denny  
U.S. Department of Energy  
Office of Arms Control  
Washington, DC 20585

Dr. Cliff Frolich  
Institute of Geophysics  
8701 North Mopac  
Austin, TX 78759

Dr. Zoltan Der  
ENSCO, Inc.  
5400 Port Royal Road  
Springfield, VA 22151-2388

Dr. Holly Given  
IGPP, A-025  
Scripps Institute of Oceanography  
University of California, San Diego  
La Jolla, CA 92093

Prof. Adam Dziewonski  
Hoffman Laboratory, Harvard University  
Dept. of Earth Atmos. & Planetary Sciences  
20 Oxford Street  
Cambridge, MA 02138

Dr. Jeffrey W. Given  
SAIC  
10260 Campus Point Drive  
San Diego, CA 92121

Prof. John Ebel  
Department of Geology & Geophysics  
Boston College  
Chestnut Hill, MA 02167

Dr. Dale Glover  
Defense Intelligence Agency  
ATTN: ODT-1B  
Washington, DC 20301

Eric Fielding  
SNEE Hall  
INSTOC  
Cornell University  
Ithaca, NY 14853

Dr. Indra Gupta  
Teledyne Geotech  
314 Montgomery Street  
Alexandria, VA 22314

Dr. Mark D. Fisk  
Mission Research Corporation  
735 State Street  
P.O. Drawer 719  
Santa Barbara, CA 93102

Dan N. Hagedorn  
Pacific Northwest Laboratories  
Battelle Boulevard  
Richland, WA 99352

Prof Stanley Flatte  
Applied Sciences Building  
University of California, Santa Cruz  
Santa Cruz, CA 95064

Dr. James Hannon  
Lawrence Livermore National Laboratory  
P.O. Box 808  
L-205  
Livermore, CA 94550

Dr. John Foley  
NER-Geo Sciences  
1100 Crown Colony Drive  
Quincy, MA 02169

Dr. Roger Hansen  
AFTAC/TTR  
Patrick AFB, FL 32925

Prof. Donald Forsyth  
Department of Geological Sciences  
Brown University  
Providence, RI 02912

Prof. David G. Harkrider  
Seismological Laboratory  
Division of Geological & Planetary Sciences  
California Institute of Technology  
Pasadena, CA 91125



Prof. Danny Harvey  
CIRES  
University of Colorado  
Boulder, CO 80309

Prof. Donald V. Helmberger  
Seismological Laboratory  
Division of Geological & Planetary Sciences  
California Institute of Technology  
Pasadena, CA 91125

Prof. Eugene Herrin  
Institute for the Study of Earth and Man  
Geophysical Laboratory  
Southern Methodist University  
Dallas, TX 75275

Prof. Robert B. Herrmann  
Department of Earth & Atmospheric Sciences  
St. Louis University  
St. Louis, MO 63156

Prof. Lane R. Johnson  
Seismographic Station  
University of California  
Berkeley, CA 94720

Prof. Thomas H. Jordan  
Department of Earth, Atmospheric &  
Planetary Sciences  
Massachusetts Institute of Technology  
Cambridge, MA 02139

Prof. Alan Kafka  
Department of Geology & Geophysics  
Boston College  
Chestnut Hill, MA 02167

Robert C. Kemerait  
ENSCO, Inc.  
445 Pineda Court  
Melbourne, FL 32940

Dr. Max Koontz  
U.S. Dept. of Energy/DP 5  
Forrestal Building  
1000 Independence Avenue  
Washington, DC 20585

Dr. Richard LaCoss  
MIT Lincoln Laboratory, M-200B  
P.O. Box 73  
Lexington, MA 02173-0073

Dr. Fred K. Lamb  
University of Illinois at Urbana-Champaign  
Department of Physics  
1110 West Green Street  
Urbana, IL 61801

Prof. Charles A. Langston  
Geosciences Department  
403 Deike Building  
The Pennsylvania State University  
University Park, PA 16802

Prof. Thorne Lay  
Institute of Tectonics  
Earth Science Board  
University of California, Santa Cruz  
Santa Cruz, CA 95064

Dr. William Leith  
U.S. Geological Survey  
Mail Stop 928  
Reston, VA 22092

James F. Lewkowicz  
Phillips Laboratory/GPEH  
Hanscom AFB, MA 01731-5000

Mr. Alfred Lieberman  
ACDA/VI-OA State Department Building  
Room 5726  
320-21st Street, NW  
Washington, DC 20451

Prof. L. Timothy Long  
School of Geophysical Sciences  
Georgia Institute of Technology  
Atlanta, GA 30332

Dr. Robert Masse  
Denver Federal Building  
Bos 25046, Mail Stop 967  
Denver, CO 80225

Dr. Randolph Martin, III  
New England Research, Inc.  
76 Olcott Drive  
White River Junction, VT 05001

Dr. Gary McCartor  
Department of Physics  
Southern Methodist University  
Dallas, TX 75275

Prof. Thomas V. McEvilly  
Seismographic Station  
University of California  
Berkeley, CA 94720

Prof. Art McGarr  
U.S. Geological Survey  
Mail Stop 977  
U.S. Geological Survey  
Menlo Park, CA 94025

Dr. Keith L. McLaughlin  
S-CUBED  
A Division of Maxwell Laboratory  
P.O. Box 1620  
La Jolla, CA 92038-1620

Stephen Miller & Dr. Alexander Florence  
SRI International  
333 Ravenswood Avenue  
Box AF 116  
Menlo Park, CA 94025-3493

Prof. Bernard Minster  
IGPP, A-025  
Scripps Institute of Oceanography  
University of California, San Diego  
La Jolla, CA 92093

Prof. Brian J. Mitchell  
Department of Earth & Atmospheric Sciences  
St. Louis University  
St. Louis, MO 63156

Mr. Jack Murphy  
S-CUBED  
A Division of Maxwell Laboratory  
11800 Sunrise Valley Drive, Suite 1212  
Reston, VA 22091 (2 Copies)

Dr. Keith K. Nakanishi  
Lawrence Livermore National Laboratory  
L-025  
P.O. Box 808  
Livermore, CA 94550

Dr. Carl Newton  
Los Alamos National Laboratory  
P.O. Box 1663  
Mail Stop C335, Group ESS-3  
Los Alamos, NM 87545

Dr. Bao Nguyen  
AFTAC/TTR  
Patrick AFB, FL 32925

Prof. John A. Orcutt  
IGPP, A-025  
Scripps Institute of Oceanography  
University of California, San Diego  
La Jolla, CA 92093

Prof. Jeffrey Park  
Kline Geology Laboratory  
P.O. Box 6666  
New Haven, CT 06511-8130

Howard Patton  
Lawrence Livermore National Laboratory  
L-025  
P.O. Box 808  
Livermore, CA 94550

Dr. Frank Pilotte  
HQ AFTAC/TT  
Patrick AFB, FL 32925-6001

Dr. Jay J. Pulli  
Radix Systems, Inc.  
2 Taft Court, Suite 203  
Rockville, MD 20850

Dr. Robert Reinke  
ATTN; FCTVTD  
Field Command  
Defense Nuclear Agency  
Kirtland AFB, NM 87115

Prof. Paul G. Richards  
Lamont-Doherty Geological Observatory  
of Columbia University  
Palisades, NY 10964

Mr. Wilmer Rivers  
Teledyne Geotech  
314 Montgomery Street  
Alexandria, VA 22314

Dr. George Rothe  
HQ AFTAC/TTR  
Patrick AFB, FL 32925-6001

Dr. Alan S. Ryall, Jr.  
DARPA/NMRO  
3701 North Fairfax Drive  
Arlington, VA 22209-1714

Dr. Richard Sailor  
TASC, Inc.  
55 Walkers Brook Drive  
Reading, MA 01867

Prof. Charles G. Sammis  
Center for Earth Sciences  
University of Southern California  
University Park  
Los Angeles, CA 90089-0741

Prof. Christopher H. Scholz  
Lamont-Doherty Geological Observatory  
of Columbia University  
Palisades, CA 10964

Dr. Susan Schwartz  
Institute of Tectonics  
1156 High Street  
Santa Cruz, CA 95064

Secretary of the Air Force  
(SAFRD)  
Washington, DC 20330

Office of the Secretary of Defense  
DDR&E  
Washington, DC 20330

Thomas J. Sereno, Jr.  
Science Application Int'l Corp.  
10260 Campus Point Drive  
San Diego, CA 92121

Dr. Michael Shore  
Defense Nuclear Agency/SPSS  
6801 Telegraph Road  
Alexandria, VA 22310

Dr. Matthew Sibol  
Virginia Tech  
Seismological Observatory  
4044 Derring Hall  
Blacksburg, VA 24061-0420

Prof. David G. Simpson  
IRIS, Inc.  
1616 North Fort Myer Drive  
Suite 1400  
Arlington, VA 22209

Donald L. Springer  
Lawrence Livermore National Laboratory  
L-025  
P.O. Box 808  
Livermore, CA 94550

Dr. Jeffrey Stevens  
S-CUBED  
A Division of Maxwell Laboratory  
P.O. Box 1620  
La Jolla, CA 92038-1620

Lt. Col. Jim Stobie  
ATTN: AFOSR/NL  
Bolling AFB  
Washington, DC 20332-6448

Prof. Brian Stump  
Institute for the Study of Earth & Man  
Geophysical Laboratory  
Southern Methodist University  
Dallas, TX 75275

Prof. Jeremiah Sullivan  
University of Illinois at Urbana-Champaign  
Department of Physics  
1110 West Green Street  
Urbana, IL 61801

Prof. L. Sykes  
Lamont-Doherty Geological Observatory  
of Columbia University  
Palisades, NY 10964

Dr. David Taylor  
ENSCO, Inc.  
445 Pineda Court  
Melbourne, FL 32940

Dr. Steven R. Taylor  
Los Alamos National Laboratory  
P.O. Box 1663  
Mail Stop C335  
Los Alamos, NM 87545

Prof. Clifford Thurber  
University of Wisconsin-Madison  
Department of Geology & Geophysics  
1215 West Dayton Street  
Madison, WI 53706

Prof. M. Nafi Toksoz  
Earth Resources Lab  
Massachusetts Institute of Technology  
42 Carleton Street  
Cambridge, MA 02142

Dr. Larry Turnour  
CIA-OSWR/NED  
Washington, DC 20505

DARPA/RMO/SECURITY OFFICE  
3701 North Fairfax Drive  
Arlington, VA 2203-1714

Dr. Gregory van der Vink  
IRIS, Inc.  
16116 North Fort Myer Drive  
Suite 1440  
Arlington, VA 22209

HQ DNA  
ATTN: Technical Library  
Washington, DC 20305

Dr. Karl Veith  
EG&G  
5211 Auth Road  
Suite 240  
Suitland, MD 20746

Defense Intelligence Agency  
Directorate for Scientific & Technical Intelligence  
ATTN: DTIB  
Washington, DC 20340-6158

Prof. Terry C. Wallace  
Department of Geosciences  
Building #77  
University of Arizona  
Tucson, AZ 85721

Defense Technical Information Center  
Cameron Station  
Alexandria, VA 22314 (2 Copies)

Dr. Thomas Weaver  
Los Alamos National Laboratory  
P.O. Box 1663  
Mail Stop C335  
Los Alamos, NM 87545

TACTEC  
Battelle Memorial Institute  
505 King Avenue  
Columbus, OH 43201 (Final Report)

Dr. William Wortman  
Mission Research Corporation  
8560 Cinderbed Road  
Suite 700  
Newington, VA 22122

Phillips Laboratory  
ATTN: XPG  
Hanscom AFB, MA 01731-5000

Prof. Francis T. Wu  
Department of Geological Sciences  
State University of New York  
at Binghamton  
Vestal, NY 13901

Phillips Laboratory  
ATTN: GPE  
Hanscom AFB, MA 01731-5000

AFTAC/CA  
(STINFO)  
Patrick AFB, FL 32925-6001

Dr. Michel Bouchon  
I.R.I.G.M.-B.P. 68  
38402 St. Martin D'Heres  
Cedex, FRANCE

DAARPA/PM  
3701 North Fairfax Drive  
Arlington, VA 22203-1714

Dr. Michel Campillo  
Observatoire de Grenoble  
I.R.I.G.M.-B.P. 53  
38041 Grenoble, FRANCE

DARPA/RMO/RETRIEVAL  
3701 North Fairfax Drive  
Arlington, VA 22203-1714

Dr. Kin Yip Chun  
Geophysics Division  
Physics Department  
University of Toronto  
Ontario, CANADA

Prof. Hans-Peter Harjes  
Institute for Geophysics  
Ruhr University/Bochum  
P.O. Box 102148  
4630 Bochum 1, GERMANY

Prof. Eystein Husebye  
NTNF/NORSAR  
P.O. Box 51  
N-2007 Kjeller, NORWAY

David Jepsen  
Acting Head, Nuclear Monitoring Section  
Bureau of Mineral Resources  
Geology and Geophysics  
G.P.O. Box 378, Canberra, AUSTRALIA

Ms. Eva Johannisson  
Senior Research Officer  
National Defense Research Inst.  
P.O. Box 27322  
S-102 54 Stockholm, SWEDEN

Dr. Peter Marshall  
Procurement Executive  
Ministry of Defense  
Blacknest, Brimpton  
Reading FG7-FRS, UNITED KINGDOM

Dr. Bernard Massinon, Dr. Pierre Mechler  
Societe Radiomana  
27 rue Claude Bernard  
75005 Paris, FRANCE (2 Copies)

Dr. Svein Mykkeltveit  
NTNT/NORSAR  
P.O. Box 51  
N-2007 Kjeller, NORWAY (3 Copies)

Prof. Keith Priestley  
University of Cambridge  
Bullard Labs, Dept. of Earth Sciences  
Madingley Rise, Madingley Road  
Cambridge CB3 0EZ, ENGLAND

Dr. Jorg Schlittenhardt  
Federal Institute for Geosciences & Nat'l Res.  
Postfach 510153  
D-3000 Hannover 51, GERMANY

Dr. Johannes Schweitzer  
Institute of Geophysics  
Ruhr University/Bochum  
P.O. Box 1102148  
4360 Bochum 1, GERMANY